VILNIUS UNIVERSITY
CENTER FOR PHYSICAL SCIENCES AND TECHNOLOGY

Tomas Čeponis

RADIATION TECHNOLOGIES FOR OPTIMIZATION OF Si DEVICE PARAMETERS AND TECHNIQUES FOR CONTROL OF RADIATION DEFECTS

Doctoral dissertation
Technological Sciences, Material Engineering (08 T)

Vilnius 2012

Doctoral dissertation was prepared during period of 2008–2012 years at Vilnius University Faculty of Physics and Institute of Applied Research

Supervisor:

Dr. Sc. Eugenijus Gaubas (Vilnius University, Technological Sciences, Material Engineering – 08 T)

VILNIAUS UNIVERSITETAS
FIZINIŲ IR TECHNOLOGIJOS MOKSLŲ CENTRAS

Tomas Čeponis

RADIACINĖS Si PRIETAISŲ PARAMETRŲ OPTIMIZAVIMO IR RADIACINIŲ DEFEKTŲ KONTROLĖS TECHNOLOGIJOS

Daktaro disertacija

Technologijos mokslai, medžiagų inžinerija (08 T)

Vilnius, 2012

Disertacija rengta 2008–2012 metais Vilniaus universiteto Fizikos fakultete ir Taikomųjų mokslų institute.

Mokslinis vadovas:
habil. dr. Eugenijus Gaubas (Vilniaus universitetas, technologijos mokslai, medžiagų inžinerija – 08 T)

Acknowledgements

First of all I would like to express my appreciation to Dr. Sc. E. Gaubas for supervising this thesis and his continuous support, advice, encouragement and long lasting discussions about fundamental problems of describing of particle detectors currents.

I am grateful to Prof. V. Gavriušinas and Dr. R. Maldžius for reading this thesis carefully and providing valuable suggestions of how to improve it.

I am thankful to my friend and colleague A. Uleckas for the good team-work, cooperation and help in performing experiments.

I would like to thank my fiancée Ksenija, my parents and friends for their support and encouragement during long years of my education.

Lithuanian State Science and Studies Foundation and Research Council of Lithuania are acknowledged for the financial support.

Contents

I. Introduction

Research problem. Silicon (Si) is one of the most widely used semiconductor materials in microelectronics, in production of semiconductor power devices, of solar cells and ionizing radiation detectors, etc. due to its well examined fundamental properties and well developed technology and relatively low price. Many nowadays applications require power devices that are capable to control large amount of energy during switching cycle, to ensure high blocking voltage and low leakage current, to maintain low voltage drop during on-state regime, and those are capable to operate at high switching rates with soft reverse recovery behaviour. Power devices are needed for systems that operate at wide spectrum of power levels and frequencies. Thyristors are usually applied for low frequency and high power applications, while Insulated Gate Bipolar Transistors (IGBTs) are exploited for the medium frequency and power applications, and power Metal Oxide Semiconductor Field Effect Transistors (MOSFETs) are employed for high frequency applications. However, there is no common device that would be suitable for the whole range of applications. Power rectifiers are used in power electronic circuits to control the direction of the current flow. Schottky diodes are capable to operate at high frequencies, however high voltage (>200 V) at blocking regime can not be achieved as the width of the drift region should be increased that would result in undesirable enhancement of the voltage drop in the on-state regime. Rectifiers designed on *pin* structures are capable to support high voltages (200 – 5000 V) at blocking regime and operate at frequencies higher than tenths of MHz. However, appropriate material properties (carrier lifetime, doping densities and profiles) must be chosen and the device structure should be designed to maintain the desired static and dynamic parameters of devices in a compromise way. Reverse recovery time (RRT) of power devices is usually controlled by introducing recombination centres into the active region of the device. These recombination centres are usually introduced by gold or platinum doping or irradiation with electrons or protons beam or implantation

of necessary elements. The shape of the reverse recovery current transient and symmetry of the reverse recovery characteristic, which is also an important parameter of the power device, can be controlled by positioning and profiling of the enhanced recombination layer within an active region of the device.

In many high energy physics experiments at European Organization for Nuclear Research (CERN), high resistivity Si particle detectors of *pin* structure operating at full depletion (diode base is fully depleted due to sufficient external electric field applied) regime are employed for tracking of the ionizing particles. These detectors should be capable to survive radiation fluences up to 10^{16} cm^{-2}. However, radiation induced defects within Si material that act as generation/recombination and carrier capture centres, consequently affect the detector functional parameters. Therefore, a variety of experiments are performed and different techniques are applied to evaluate the radiation damage mechanisms and their impact on detector functional parameters. Furthermore, it is necessary to search for the new approaches on how to suppress or control the degradation process of detectors, as well as to design advanced detector structures.

Evaluation of the mechanisms of radiation damage of particle detectors in the range of high fluences is commonly implemented by combining of several techniques. Examination of leakage current, of carrier generation lifetime is performed by thermally stimulated current (TSC), by capacitance deep level transient spectroscopy (DLTS) and by exploiting measurements of drift current transients (TCT) in analysis of the post-irradiation state of devices. However, capacitance and depletion based measurements (DLTS, C-V and TCT) become complicated when high resistivity material (with rather small doping density) is exploited in fabrication of particle detectors. Then, heavily irradiated diodes may experience a transition to an insulating substance state with rather small free carrier concentration (due to high density of different type carrier capture centres) insufficient to sustain a depletion boundary, by exhibiting a long dielectric relaxation time. Therefore, evaluation of carrier capture and generation lifetimes as well as of other important parameters

becomes a complicated task when depletion width based techniques are employed. Although, concerted analysis and the deduced characteristics in lightly irradiated structures might be useful to anticipate trends and primary understanding of the radiation induced defect complexes and their impact on functional characteristics of particle detectors. However, in the range of high irradiation fluences ($>10^{14}$ cm^{-2}), application of the above-mentioned techniques is complicated since the radiation defect density significantly overpasses the concentration of dopants, and cluster formation may become the dominant mechanism in radiation damaged detector material. Additionally, measurements carried out after irradiation do not provide direct information on the evolution and interactions within the densely radiation damaged material.

Particle detectors are designed referring to Ramo's theorem which describes the induced current flowing in the external circuit when the particle crosses the detector volume. This theorem was originally formulated for the linear medium in design of vacuum tubes and does not describe the current components caused by charge relaxation, generation and capture processes that are inherent for the irradiated semiconductor detectors. Furthermore, the analysis of current transient flowing in the external circuit becomes more complicated if the diode is not fully depleted.

Hence, it is important to develop the techniques that would allow revealing of parameters of the material and devices irradiated with high fluences ($\Phi \geq 10^{14}$ cm^{-2}), radiation damage mechanisms and evolution of defects during irradiation.

Objectives of research. The aim of this work is addressed to technological developments for optimization of the functional parameters of *pin* power diodes, when radiation technologies are employed, as well as developments of materials science and defect engineering, by creation of novel techniques for the characterization of heavily irradiated diodes and models capable to reveal peculiarities of the variations in carrier transport,

generation/recombination and capture parameters within detectors irradiated by high fluences.

The main objectives were concentrated on:

- optimization of the regimes of protons irradiation applied to power *pin* diodes for enhancement of the switching rates to hundreds of nanoseconds by maintaining the high blocking and low on-state voltages,
- simulation of irradiation regimes for the optimization of the device static and dynamic parameters by formation the δ- or triangle shape enhanced recombination layers and comparative analysis of parameters after irradiation,
- creation of the techniques capable to unveil radiation damage mechanisms in heavily irradiated Si detectors after irradiation and to monitor the evolution of defects during irradiation,
- development of techniques for the *in situ* control of the device operational parameters during modification by protons beam,
- design of the techniques for spectroscopy of radiation induced carrier traps and for profiling of depth-distribution of radiation defects within layered device structures,
- analysis of the regimes for suppression of radiation defects by anneals technologies.

Relevance and scientific novelty. Detail analysis of different device operation factors to reach a trade-off and optimization of the static and dynamic parameters of power *pin* diodes by varying the protons irradiation regimes and by formation of various profiles of the enhanced recombination layers (δ- or triangle shape) as well as their location within diode base region comprise novelty in this work. Comprehensive control techniques and regimes of thermal anneal procedures in suppression and manipulation of the electrical activity of the radiation induced defects also contains technological novelty. Development of the techniques allowing of the *in situ* monitoring of the modification of material parameters as well as evolution of radiation defects during irradiation is a new approach and technological solution. Models

describing displacement, drift and diffusion current components and their impact on the pulsed operation characteristics of the irradiated detectors are proposed and approved for analysis of carrier transport and capture/generation parameters, comprising scientific and measurement technology novelties. New measurement techniques for spectroscopy and profiling of dopants and for analysis of radiation defects have been designed and implemented in fast characterization of layered device structures.

Practical importance. The designed irradiation/anneal procedures within modification of parameters of the power rectifiers and techniques for control of dynamic characteristics of devices performed on industrial structures comprise the technological importance of this study. The irradiation regimes for profiling of enhanced recombination layers and for governing of the reverse recovery characteristics might be included into a technological route of production of the power devices.

The techniques developed for the *in situ* monitoring of variations of material parameters during hadrons irradiation or implantation of ions can be applied in practice for the design of radiation technologies in modification of parameters of power devices and for the on-line dosimetry of background irradiations within accelerator facilities.

The proposed model for separation of current components in irradiated diodes, when using different pulsed excitation and biasing regimes, is beneficial for the analysis of registered signals, generated by detectors during their operation. The revealed peculiarities of degradation of the detectors caused by the increase of generation current and of depletion width should be considered within design of novel and radiation tolerant detectors.

It has been shown that the developed pulsed techniques for spectroscopy and profiling of impurities and other defects, based on concerted analysis of barrier and storage capacitance transients as well as of various current components, is a powerful tool for fast analysis of different device structures

and can be applied for technological control of radiation detectors, solar cells, power switches and other junction structures.

Statements in defence. The main statements in defence of this thesis are as follows:

1. The proposed model of pulsed charging current transients, by analyzing the displacement as well as carrier drift, diffusion and generation components within changes of barrier and storage capacitance of junction structures, can be applied for a design of transient techniques for evaluation of the operational particle detectors parameters and irradiated material characteristics in a wide range of induced charge densities.
2. The designed technique of barrier and storage capacitance changes under linearly increasing voltage pulses, implemented by combining of varied pulse durations, of primaring by dc voltage bias, by varying of sample temperature and by applying either cw or pulsed bias illumination of different intensity as well as of spectral range, can be applied for spectroscopy and profiling of impurities and radiation defects in Si junction structures.
3. The designed technology of combined measurements of barrier capacitance charging current and of induced charge current pulsed transients as a function of irradiation fluence enables one to examine *in situ* an evolution of radiation defects and to determine a degradation of operational characteristics of device structures post-irradiation, by evaluating the changes of depletion width and of leakage current device characteristics and of simultaneous variations in carrier recombination, generation and transport parameters in the irradiated material.
4. The combined modelling and measurements of the reverse recovery time, of recovery softness and of forward voltage drop characteristics in Si power diodes show that these parameters strongly depend on values of carrier lifetime at high injection and on their depth-distribution within

diode base region, while the desired trends in variations of these parameters dependent on carrier lifetime appear at discrepant tendencies. Therefore optimization of dynamic diode operation characteristics can be only achieved by trade-off, using formation of strongly localized and predictably distributed recombination centres by proton beams when stabilized extended radiation defects are created. To reach a trade-off between the dynamic and static diode parameters, the radiation induced traps with short low-level carrier lifetime should be annealed, however creation of different species and densities of protons beam induced defects makes the annealing procedure complicated.

Author's contribution. Over this study author prepared samples for the irradiations and performed simulations of irradiation regimes to create δ- and triangle shape enhanced recombination profiles for the modification of parameters of power diodes. Author performed measurements on reverse recovery time, on-state voltage drop, current-voltage, capacitance-voltage characteristics, part of DLTS and proposed the surface passivation procedures of Si wafer samples for the control of carrier recombination lifetime. Author contributed within creation of contact techniques for the evaluation of barrier and transport parameters, made the main experimental and simulation research presented in this dissertation. The main results were presented at a number of international (RESMDD2010, IWORID13, etc.) and national (LNFK38, LNFK39) conferences and several drafts of manuscripts were prepared by the author.

Measurements of recombination characteristics were performed in collaboration with PHD student A. Uleckas. Also, A. Uleckas created software for data analysis and control of measurements within study of barrier and transport characteristics and considerably helped during *in situ* experiments. All the investigations, data analysis and preparation of manuscripts were made under supervision of Dr. Sc. E. Gaubas.

The power *pin* diode structures were produced and Si wafer substrate samples were provided by enterprise “Vilniaus Ventos Puslaidininkiai”. Proton irradiations of power diodes and *in situ* experiments of carrier transport parameters were performed at Helsinki University Accelerator Laboratory. *In situ* experiments of barrier capacitance variations during protons implantation were performed by ion accelerator installed at State Research Institute Centre for Physical Sciences and Technology, Vilnius. The neutron irradiated Si *pin* detectors for measurements of fluence dependent variations of barrier parameters were prepared within CERN RD50 project, using Ljubljana TRIGA reactor.

Articles published. The main results of this study are published within 20 scientific articles and presented at 29 conferences. Publications are listed below:

A1. E. Gaubas, **T. Čeponis**, D. Šalucha, I.Šimkienė, and A. Uleckas, Characteristics of surface recombination in silicon diode isolation grooves. Lith. J. Phys. **47** (2007) 461.

A2. J. Višniakov, E. Gaubas, **T. Čeponis**, A. Uleckas, J. Raisanen, and S. Vayrynen, Comparative investigation of recombination characteristics in proton and electron irradiated Si structures. Lith. J. Phys. **48** (2008) 137.

A3. J. Višniakov, **T. Čeponis**, E. Gaubas, and A. Uleckas, Comparative study of the recombination characteristics in electron, proton and neutron irradiated Si structures. Materials of the international conference “Radiation Interaction with Material and Its Use in Technologies 2008” Kaunas, “Technologija” (2008) 22.

A4. **T. Čeponis**, E. Gaubas, A. Uleckas, and J. Višniakov, Investigation of the anneal induced transformations of radiation defects in proton implanted Si structures. Materials of the international conference “Radiation Interaction with Material and Its Use in Technologies 2008” Kaunas, “Technologija” (2008) 226.

A5. J. Višniakov, **T. Čeponis**, E. Gaubas, and A. Uleckas, Anneal-induced variations of the recombination characteristics in 2 MeV proton irradiated Si structures. Lith. J. Phys. **48** (2008) 325.

A6. J. Višniakov, **T. Čeponis**, E. Gaubas, and A. Uleckas, Study of recombination characteristics in 2 MeV protons irradiated and annealed Si structures. Nucl. Instrum. Methods A **607** (2009) 95.

A7. E. Gaubas, **T. Čeponis**, A. Uleckas, and J. Vaitkus, Anneal dependent variations of recombination and generation lifetime in neutron irradiated MCZ Si. Nucl. Instrum. Methods A **612** (2010) 563.

A8. A. Uleckas, **T. Čeponis**, A. Dzimidavičius, E. Gaubas, J. Pavlovas, and K. Žilinskas, Investigation of the switching and carrier recombination characteristics in the proton irradiated and thermally annealed Si *pin* diodes. Lith. J. Phys. **50** (2010) 225.

A9. **T. Čeponis**, A. Balčytis, A. Dzimidavičius, E. Gaubas, J. Kusakovskij, and K. Žilinskas, Dependence of silicon *PIN* diode electrical characteristics on proton fluence. Lith. J. Phys. **50** (2010) 215.

A10. **T. Čeponis**, E. Gaubas, A. Uleckas, and K. Žilinskas, *In situ* study of carrier drift and diffusion characteristics during proton irradiation. Materials of the international conference “Radiation Interaction with Material and Its Use in Technologies 2010” Kaunas, “Technologija” (2010) 77.

A11. E. Gaubas, **T. Čeponis**, S. Sakalauskas, A. Uleckas, and A. Velička, Fluence dependent variations of barrier and generation currents in neutron and proton irradiated Si *pin* diodes. Lith. J. Phys. **51** (2011) 227.

A12. E. Gaubas, **T. Čeponis**, J. Vaitkus, and J. Raisanen, Carrier drift and diffusion characteristics of Si *pin* detectors measured *in situ* during protons irradiation. Lith. J. Phys. **51** (2011) 351.

A13. E. Gaubas, **T. Čeponis**, and J. Vaitkus, Impact of generation current on evaluation of the depletion width in heavily irradiated Si detectors. J. Appl. Phys. **110** (2011) 033719.

A14. E. Gaubas, **T. Čeponis**, J. Kusakovskij, and A. Uleckas, Barrier evaluation by linearly increasing voltage technique applied to Si solar cells and irradiated *pin* diodes. ISRN Materials Sc. **2012** (2012) Article ID 543790.

A15. E. Gaubas, **T. Čeponis**, and J. Kusakovskij, Profiling of barrier capacitance and spreading resistance by transient linearly increasing voltage technique. Rev. Sc. Instrum. **82** (2011) 083304.

A16. E. Gaubas, **T. Čeponis**, J. Vaitkus, and J. Raisanen, Study of variations of carrier recombination and charge transport parameters during proton irradiation of silicon *pin* diode structures. AIP Advances, **1** (2011) 022143.

A17. **T. Čeponis**, E. Gaubas, V. Kalendra, A. Uleckas, J. Vaitkus, K. Zilinskas, V. Kovalevskij, M. Gaspariunas, and V. Remeikis, *In situ* analysis of carrier lifetime and barrier capacitance variations in silicon during 1.5 MeV protons implantation. J. Instrum. **6** (2011) P09002.

A18. E. Gaubas , **T. Čeponis**, A. Uleckas, and R. Grigonis, Room temperature spectroscopy of deep levels in junction structures using barrier capacitance charging current transients. J. Instrum. **7** (2012) P01003.

A19. **T. Čeponis**, and E. Gaubas, Peculiarities of separation of the radiation detector currents. Materials of the international conference “Radiation Interaction with Material and Its Use in Technologies 2012” Kaunas, “Technologija” (2012) 274.

A20. J. Kusakovskij, **T. Čeponis,** E. Gaubas, and D. Meškauskaitė, Profiling of proton irradiated Si *pin* diodes by capacitance-voltage technique. Materials of the international conference “Radiation Interaction with Material and Its Use in Technologies 2012” Kaunas, “Technologija” (2012) 278.

Publications which results are not included in the thesis are listed below:

A21. E. Gaubas, **T. Čeponis**, A. Uleckas, and J. Vaitkus, Recombination characteristics in 2–3 MeV protons irradiated FZ Si. Nucl. Instrum. Methods A **612** (2010) 559.

A22. A. Uleckas, E. Gaubas, **T. Čeponis**, and A. Balčytis, *In situ* study of carriers recombination characteristics during proton irradiation. Materials of the international conference "Radiation Interaction with Material and Its Use in Technologies 2010" Kaunas, "Technologija" (2010) pp. 81.

A23. E. Gaubas, **T. Čeponis**, A. Uleckas, J. Vaitkus, K. Žilinskas, V. Kovalevskij, M. Gaspariunas, and V. Remeikis, *In situ* analysis of the carrier lifetime modifications in silicon during implantation of 1.5 MeV protons. Lith. J. Phys. **50** (2010) 427.

A24. A. Uleckas, E. Gaubas, **T. Čeponis**, K. Zilinskas, R. Grigonis, V. Sirutkaitis, and J. Vanhellemont, Analysis of Auger Recombination Characteristics in High Resistivity Si and Ge. Sol. State Phenom. **178-179** (2011) 427.

Presentations at conferences. Oral and poster presentations are listed below:

P1. E. Gaubas, J. Vaitkus, **T. Čeponis**, A. Uleckas, J. Raisanen, S. Vayrynen, and E. Fretwurst, Fluence dependent recombination lifetime in neutron and proton irradiated MCz, FZ and epi-Si structures. 11th CERN RD50 Workshop, GENEVA, 2007.

P2. J. Višniakov, **T. Čeponis**, E. Gaubas, and A. Uleckas, Comparative study of the recombination characteristics in electron, proton and neutron irradiated Si structures. International conference "Radiation Interaction with Material and Its Use in Technologies", Kaunas, 2008.

P3. **T. Čeponis**, E. Gaubas, A. Uleckas, and J. Višniakov, Investigation of the anneal induced transformations of radiation defects in proton implanted Si

structures. International conference “Radiation Interaction with Material and Its Use in Technologies”, Kaunas, 2008.

P4. E. Gaubas, J. Vaitkus, **T. Čeponis**, A. Uleckas, E. Fretwurst, and G. Lindstrom, Fluence dependent variations of recombination and deep level spectral characteristics in neutron and proton irradiated MCz , FZ and epi-Si structures. 3rd Workshop on Defect Analysis in Silicon Detectors, Hamburg, 2008.

P5. J. Vaitkus, **T. Čeponis**, E. Gaubas, A. Uleckas, J. Višniakov, and J. Raisanen, Fluence and isochronal anneal dependent variations of recombination and DLTS characteristics in neutron and proton irradiated MCz, FZ and epi-Si structures. 12th CERN RD50 Workshop, Ljubljana, 2008.

P6. **T. Čeponis**, A. Dzimidavičius, E. Gaubas, J. Pavlov, and A. Uleckas, Investigation of correlation between characteristics of carrier recombination and switching of Si *pin* diodes irradiated by protons and neutrons. Lithuanian National Conference of Physics 38, Vilnius, 2009.

P7. **T. Čeponis**, A. Balčytis, E. Gaubas, and J. Kusakovskij, Variations of the electrical characteristics in proton irradiated *pin* diodes. Lithuanian National Conference of Physics 38, Vilnius, 2009.

P8. J. Vaitkus, E. Gaubas, **T. Čeponis** and A. Uleckas, Comparative study of the electric field dependent variations of carrier recombination and drift parameters in MCZ Si detectors irradiated by different fluences of neutrons. 14th CERN RD50 Workshop, Freiburg, 2009.

P9. J. Vaitkus, E. Gaubas, **T. Čeponis**, A. Uleckas, J. Raisanen, J. Harkonen, and E. Tuominen, Carrier lifetime and charge extraction-collection variations during irradiation of the MCZ Si wafers and detectors by 8 MeV protons. 15th CERN RD50 Workshop, Geneva, 2009.

P10. J. Vaitkus, E. Gaubas, V. Kazukauskas, N. Vainorius, **T. Čeponis**, A. Uleckas, J. Kusakovskij, A. Velicka, and K. Žilinskas, Properties of a new series of Hamamatsu Si diodes. 17th RD50 Workshop, Geneva, 2010.

P11. E. Gaubas, **T. Čeponis**, A. Uleckas, J. Vaitkus, E. Žąsinas, and J. Raisanen, Study of dominant recombination defects by fluence dependent variations of carrier lifetimes and drift parameters in MCZ Si. 16th CERN RD50 Workshop, Barcelona, 2010.

P12. E. Gaubas, **T. Čeponis**, A. Uleckas, S. Sakalauskas, and J. Vaitkus, Evaluation of fluence dependent variations of capacitance and generation current parameters by transient technique. 16th CERN RD50 Workshop, Barcelona, 2010.

P13. **T. Čeponis**, E. Gaubas, S. Sakalauskas, and A. Uleckas, Evaluation of barrier and carrier generation parameters in neutron irradiated Si *pin* diodes by transient technique. 12th International Conference-School "Advanced Materials and Technologies", Palanga, 2010.

P14. **T. Čeponis**, E. Gaubas, A. Uleckas, and K. Žilinskas, *In situ* study of carrier drift and diffusion characteristics during proton irradiation. International conference "Radiation Interaction with Material and Its Use in Technologies" Kaunas, 2010.

P15. **T. Čeponis**, E. Gaubas, J. Vaitkus, and J. Raisanen, Carrier drift and diffusion characteristics of Si *pin* detectors measured *in situ* during protons irradiation. 8th International Conference on Radiation Effects on Semiconductor Materials Detectors and Devices, Florence, 2010.

P16. **T. Čeponis**, E. Gaubas, S. Sakalauskas, and A. Uleckas, Fluence dependent variations of barrier and generation currents in neutron and proton irradiated Si *pin* diodes. 8th International Conference on Radiation Effects on Semiconductor Materials Detectors and Devices, Florence, 2010.

P17. E. Gaubas, **T. Čeponis**, R. Grigonis, A. Uleckas, and J. Vaitkus, Carrier recombination and emission lifetimes in heavily irradiated pad–detectors and their impact on operational characteristics of *pin* diodes. 18th RD50 Workshop, Liverpool, 2011.

P18. **T. Čeponis**, E. Gaubas, A. Uleckas, J. Vaitkus, K. Žilinskas, V. Kovalevskij, M Gaspariūnas, and V. Remeikis, *In situ* analysis of carrier

lifetime and barrier capacitance variations in silicon during 1.5 MeV protons implantation. International Workshop on Radiation Imaging Detectors, Zurich, 2011.

P19. **T. Čeponis**, E. Gaubas, J. Kusakovskij, and A. Uleckas, Fluence dependent barrier capacitance and compensation effects in neutron irradiated Si *pin* diodes. International Workshop on Radiation Imaging Detectors, Zurich, 2011.

P20. K. Žilinskas, **T. Čeponis**, E. Gaubas, and A. Uleckas, Investigation of barrier capacitance charging currents in Si *pin* diodes dependent on IR bias illumination. 13th International Conference-School "Advanced Materials and Technologies", Palanga, 2011.

P21. A. Velička, **T. Čeponis**, E. Gaubas, A. Uleckas, Investigation of technological defects within Si thyristor structures by capacitance voltage and capacitance-deep level transient spectroscopy techniques. 13th International Conference-School "Advanced Materials and Technologies", Palanga, 2011.

P22. A. Uleckas, E. Gaubas, **T. Čeponis**, and R. Grigonis, Generation current and photoconductivity spectroscopy in Si *pin* diodes by employing barrier capacitance probing technique. 13th International Conference-School "Advanced Materials and Technologies", Palanga, 2011.

P23. V. Kalendra, **T. Čeponis**, E. Gaubas, A. Uleckas, and V. Kovalevskij, *In situ* analysis of carrier lifetime in Si structures during proton irradiation. 13th International Conference-School "Advanced Materials and Technologies", Palanga, 2011.

P24. **T. Čeponis**, E. Gaubas, and J. Kusakovskij, Barrier capacitance and spreading resistance profiling by linearly increasing voltage pulsed technique. 13th International Conference-School "Advanced Materials and Technologies", Palanga, 2011.

P25. **T. Čeponis**, E. Gaubas, and J. Kusakovskij, Profiling of barrier capacitance and spreading resistance by pulsed technique. Lithuanian National Conference of Physics 39, Vilnius, 2011.

P26. A. Uleckas, E. Gaubas, **T. Čeponis**, A. Tekorius, V. Kovalevskij, and V. Remeikis, Analysis of barrier charging current variations in Si particle detectors during 1.5 MeV proton irradiation. Lithuanian National Conference of Physics 39, Vilnius, 2011.

P27. J. Kusakovskij, **T. Čeponis**, and E. Gaubas, Simulations of Spreading current in Si layered structures. Lithuanian National Conference of Physics 39, Vilnius, 2011.

P28. A. Velička, **T. Čeponis**, E. Gaubas, A. Uleckas, and A. Tekorius, Investigation of the technological defects anneal in Si thyristor structures by capacitance and deep level spectroscopy techniques. Lithuanian National Conference of Physics 39, Vilnius, 2011.

P29. E. Gaubas, J. Vaitkus, **T. Čeponis**, A. Uleckas, Prototype instrument for fluence monitoring based on carrier lifetime control by microwave probed photoconductivity transients. AIDA 1st Annual Meeting, DESY, Hamburg, 2012.

P30. **T. Čeponis**, and E. Gaubas, Peculiarities of separation of the radiation detector currents. International conference “Radiation Interaction with Material and Its Use in Technologies” Kaunas, 2012.

P31. J. Kusakovskij, **T. Čeponis,** E. Gaubas, and D. Meškauskaitė, Profiling of proton irradiated Si *pin* diodes by capacitance-voltage technique. International conference “Radiation Interaction with Material and Its Use in Technologies” Kaunas, 2012.

Structure of dissertation. The dissertation consists of seven chapters as introduction, survey on power device and particle detectors operational characteristics, experimental techniques, results and analysis of radiation induced modifications of parameters of power devices, variations of barrier parameters in particle detectors after neutron irradiation and during protons implantation, variations of carrier transport parameters during protons irradiation, results on simulations of power device characteristics. List of references is provided at the end of the thesis.

II. Survey on power device and particle detectors operational characteristics

2.1. Radiation induced interactions and damage mechanisms in Si

Since radiation related technologies is the main subject of this thesis, it is first necessary to discuss the radiation interaction and damage mechanisms in material.

Radiation damage is basically ascribed to ionising and displacement damage [1, 2]. Ionising events happen when radiation creates the electron-hole pairs, while displacement damage, which requires more single event energy, appears via dissipation of the radiation and ionization phenomena as well as of nuclear reactions, - when lattice atoms are knocked from their sights, thus, creating vacancies and interstitials.

Ionisation damage. Three basic types of radiation interaction with material dependent on photons energy may occur [3]. At low (of a few keV's) energies the whole energy of the photon is absorbed resulting in creation of electron-hole pairs. This effect is called photoelectric effect. In Si the threshold energy value for electron-hole pair creation is about $E_{e\text{-}h}$=3.6 eV. In the range of intermediate photon energies Compton effect dominates. After absorption of incident photon, the lower energy photon is emitted which can further be absorbed if it possesses sufficient energy for electron-hole pair creation. If E_{ph} is the energy of incident photon then $E_{ph}/E_{e\text{-}h}$ electron-hole pairs will be created.

For high energy photons electron-positron pair production dominates. The probability of manifestation of radiation interaction mechanisms is presented in Fig. 2.1.

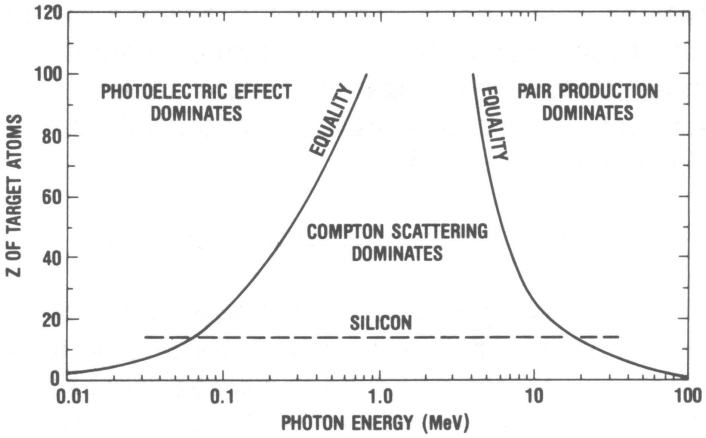

Fig. 2.1. Three types of radiation interaction with material. The solid lines correspond to equal possibilities of neighbouring energy loss mechanisms. The dashed line highlights the effects in Si (with atomic number Z=14). [3]

Displacement damage. The energy of particles is dissipated via elastic or inelastic collisions. This energy might be high enough to knock directly the atom from its lattice site. In such a situation the displacement damage appears through cascade energy transfer processes, when the last displacement event (with activation energy of about 15 eV for Si lattice) creates a vacancy (V) at the same time forming an interstitial (I). Such lattice defects are called point defects. These primarily created defects are mobile at room temperature and might migrate. They are able to recombine or can be trapped by impurity atoms and form more stable secondary defects or complexes. Possible reactions of primary defects with impurity atoms and other point defects are presented in table 2.1 [4-6].

Table 2.1. Possible reactions of radiation induced primary radiation defects with impurity atoms and other point defects [4-6].

$V+I \rightarrow Si$	$I+I \rightarrow I_2$
$V+V \rightarrow V_2$	$I+V_2 \rightarrow V$
$V+V_2 \rightarrow V_3$	$I+V_3 \rightarrow V_2$
$V+O \rightarrow VO$	$I+VO \rightarrow O$
$V+VO \rightarrow V_2O$	$I+V_2O \rightarrow VO$
$V+V_2O \rightarrow V_3O$	$I+V_3O \rightarrow V_2O$
$V+P \rightarrow VP$	$I+VP \rightarrow P$
$V+I_2 \rightarrow I$	$I+C_S \rightarrow C_i$
$V+ICC \rightarrow CC$	$I+CC \rightarrow ICC$
$V+ICO \rightarrow CO$	$I+CO \rightarrow ICO$

The symbols in table 2.1 represent: V_2, V_3 – divacancy and trivacancy defects, respectively, I_2 is complex of two interstitials, O, P and C are ascribed to oxygen, phosphorus and carbon impurity atoms, respectively. C_i and C_s are carbon atoms in interstitial and substitutional positions. For energetic ions only a fraction of ≤0.1% goes into displacement damage. For very high energy particles inelastic nuclear collision may occur. Then energetic particles are absorbed by nucleus and nucleons (alpha particles and γ-photons) are eradiated. The fraction of energy which goes into lattice damage is called Non Ionising Energy Loss (NIEL).

For neutron irradiations the ionizing and Rutherford-type interactions can be neglected as most of the energy loss is caused by inelastic displacements. Then neutron transmutation doping (NTD) may occur, which can be depicted by the reaction [1, 7]:

$$^{30}\mathrm{Si}(n,\gamma) \rightarrow {}^{31}\mathrm{Si} \rightarrow {}^{31}\mathrm{P}+\beta^{-}. \qquad (2.1)$$

Here thermal neutrons are absorbed by Si nucleus, which becomes unstable isotope and transforms into P donor atom after emission of an electron (β^-). The starting material for NTD is p-type Si which becomes n-type after certain neutron exposure duration. In this case very homogeneous distribution of resistivity can be achieved.

2.2. Radiation technologies for the optimization of Si power devices

The optimization of static and dynamic parameters of power devices is achieved by the modification of carrier lifetime of the device material. There are different technologies employed for the lifetime technological control, such as gold or platinum diffusion, gamma, electron or proton irradiation, or implantation of necessary elements into the active region of power devices to produce recombination centres [7].

The in-diffusion of gold or platinum impurities is commonly performed in fabrication of power devices, but before metallization electrodes are formed. To achieve uniform distribution of recombination centres the temperature is kept in the range of 800-900 ^{o}C. The in-diffused concentration of impurities is

controlled by varying the temperature because the solid solubility of the Au, Pt impurities depends on temperature. Wafer temperature must be reduced rapidly after a certain time of diffusion to lock the impurities within crystal lattice. Electrodes can only be formed after gold or platinum diffusion. Thus, the device parameters can not be tested before performing lifetime control procedures. Moreover, even small variations of temperature during diffusion procedure can produce large variations of device parameters [7]. These problems can be avoided by high energy irradiation technologies.

Irradiation using high energy particles causes lattice damage by displacement of Si atoms from their sites, consequently creating excess vacancies and interstitials [1]. These primary defects are not stable, as they migrate within crystal and form complexes with impurity atoms. The latter complexes produce various carrier trap levels within the bandgap [4, 8]. There are many advantages in applications of radiation techniques [7], namely: i) the irradiation can be performed at room temperature and after complete fabrication (including metallization) of the device, and thereby the device characteristics can be tested before irradiation and immediately after irradiation; ii) the lifetime can be precisely controlled by monitoring the irradiation dose; iii) the irradiations can be performed in steps by testing the device parameters after each step until desired parameters are achieved; iv) the irradiation procedures are cleaner by comparing with diffusion when contaminant together with gold or platinum atoms might be introduced; v) the enhanced recombination layer can be positioned at various depths within device structures by implantation of certain atoms of various energies.

Radiation defects enrich the bandgap with a variety of levels that modify the recombination parameters of a material [1] and consequently the parameters of a power device [7]. Therefore it is necessary to discuss the influence of defect levels for the modification of recombination characteristics and, consequently, the power device parameters.

In semiconductors under thermal equilibrium conditions, a detail balance between the generation and recombination occurs. External stimulus

disturbs this equilibrium by creation of excess carriers. After external stimulus is removed, the excess carrier density returns to equilibrium value. The rate of recovery is governed by the minority carrier lifetime (within Shockley-Read-Hall recombination statistics approach [9]). The recovery to equilibrium may occur via several simultaneous processes [10], namely: i) the interband recombination (in Si radiation processes are irrelevant due to indirect bandgap); ii) the phonon assisted recombination via deep levels; iii) three particle Auger recombination (is important in heavily doped Si or at very high excitation levels); iv) surface recombination due to surface traps.

The recombination rate via a single level is controlled by minority carrier lifetime and described by Shockley-Read-Hall model [9]. Then, carrier lifetime is expressed as:

$$\tau = \frac{\delta n}{U} = \tau_{p0}\left(\frac{n_0 + n_1 + \delta n}{n_0 + p_0 + \delta n}\right) + \tau_{n0}\left(\frac{p_0 + p_1 + \delta n}{n_0 + p_0 + \delta n}\right). \qquad (2.2)$$

Here δn is an excess electron concentration equal to excess holes concentration δp; U – recombination rate; τ_{p0} and τ_{n0} – minority carrier lifetimes in heavily doped n-type and p-type conductivity semiconductor, respectively. n_0 and p_0 are the equilibrium concentrations for the electrons and holes, respectively. $n_1=N_C\exp((E_r-E_C)/k_BT)=n_i\exp((E_r-E_i)/k_BT)$ and $p_1=N_V\exp((E_V-E_r)/k_BT)=n_i\exp((E_i-E_r)/k_BT)$ represent the equilibrium electron and hole densities, respectively, when Fermi level position coincides with the recombination level position, with N_C and N_V – the density of states in the conduction and valence bands, respectively. Here, E_C, E_r, E_V and E_i denote the conduction band, recombination level, the valence band and intrinsic energy levels, respectively. k_B denotes Boltzmann‘s constant, and T - the absolute temperature. In n-type material carrier pair lifetime can be written as

$$\frac{\tau}{\tau_{p0}} = \left[1 + \frac{1}{(1+h)}e^{(E_r-E_F)/k_BT}\right] + \zeta\left[\frac{h}{(1+h)} + \frac{1}{(1+h)}e^{(2E_i-E_r-E_F)/k_BT}\right]. \qquad (2.3)$$

Here E_F is Fermi energy level position, $\zeta=\tau_{n0}/\tau_{p0}$ is the ratio of the minority carrier lifetimes in heavily doped p-type and n-type material, and $h=\delta n/n_0$ denotes the injection level.

The minority carrier lifetime in heavily doped p-type and n-type material is dependent on the capture cross-sections for electrons (c_n) and holes (c_p) at the recombination centre and expressed as:

$$\tau_{n0} = \frac{1}{c_n N_r} = \frac{1}{v_{Tn}\sigma_{cn} N_r} \tag{2.4}$$

and

$$\tau_{p0} = \frac{1}{c_p N_r} = \frac{1}{v_{Tp}\sigma_{cp} N_r} \ . \tag{2.5}$$

Here v_{Tn} and v_{Tp} are the thermal velocities for electrons and holes, respectively, and N_r is the density of recombination centres.

At low injection levels (h<<1), according to Eq. (2.3), carrier lifetime is independent of carrier density and acquires a constant value:

$$\frac{\tau_{LL}}{\tau_{p0}} = \left[1 + e^{(E_r - E_F)/k_B T}\right] + \zeta\left[e^{(2E_i - E_r - E_F)/k_B T}\right]. \tag{2.6}$$

At high injection levels (h>>1), the lifetime again from Eq. (2.3) is independent of injection level and in this case is expressed as

$$\frac{\tau_{HL}}{\tau_{p0}} = 1 + \zeta \ . \tag{2.7}$$

From equations (2.6) and (2.7), it can be seen that τ_{LL} is the shortest one when the recombination centre is located in the middle of the bandgap and τ_{LL} value increases if recombination level moves towards the conduction or valence band, while τ_{HL} is independent of recombination level position. However, τ_{HL} depends on parameter ζ.

Carrier generation lifetime, expressed as [7]

$$\tau_g = \tau_{p0}\left[e^{(E_r - E_i)/k_B T} + \zeta e^{(E_i - E_r)/k_B T}\right], \tag{2.8}$$

strongly depends on recombination level position. The shortest τ_g is obtained when recombination level is situated in the middle of the bandgap. A reduction of generation lifetime leads to an increase of the leakage current, which is related to τ_g as

$$I_g = q_e S w_d \frac{n_i}{\tau_g}. \quad (2.9)$$

Here, q_e is the elementary charge, S – an area of the junction, w_d – the depletion width, n_i – the intrinsic carrier concentration.

Therefore, τ_{LL}, τ_{HL}, τ_{SC} can be controlled by varying the recombination level position or value of ζ. This can be achieved by employing radiation techniques, as these techniques are suitable for the control of introduction of vast variety of defects [1].

In power devices, the ratio τ_{HL}/τ_{LL} should be kept large in order to maximize the concentration of injected minority carriers and to modulate the conductivity of the base region during current flow. This is achieved when the recombination level is positioned in the middle of the bangap. However, large τ_{HL}/τ_{LL} ratio opposes the low leakage current. Therefore, traps inducing the deep levels and characterized by rather large carrier capture cross-section are desirable. Furthermore, reverse recovery time τ_{RR} and peak reverse current I_{RP} values are reduced when τ_{HL} is short and also depends on recombination layer position within diode structure. Therefore, optimization of the parameters of power devices can only be achieved in a compromise way by engineering the dominant recombination levels and by positioning of recombination layers within diode base region.

The modification of recombination characteristics for the control of dynamic parameters of power devices is commonly employed using irradiations by electrons, protons, alpha particles or combining irradiations of several species. Electron irradiations create homogeneous damage within sample bulk. Meanwhile, protons or alpha particles damage is inhomogeneous because secondary displacements near the site of the primary displacement occur [1, 5]. Protons or ions dissipate most of their energy at their projectile depth, thus creating high density of defects at their stopping range. The penetration depth within the material depends on the energy of ions. Therefore, implantation of certain ions allows of modifying locally the distribution of

defects and consequently the recombination parameters within the depth of device structure [1, 11, 12].

Protons, electrons and alpha particles produce radiation defects such as single or double charged divacancies $V_2^{-/0}$ or $V_2^{=/-}$, respectively, vacancy–oxygen pairs VO, and carbon–oxygen interstitial pairs C_iO_i [13, 14, 15]. During protons implantation (opposite to electrons and alphas) the hydrogen related defects, such as VOH are also produced. These levels have a negligible influence on carrier generation and recombination at low irradiation fluences due to their low values of carrier capture cross-sections [16]. The dominant centres are VO complexes, responsible for the lifetime at high injection level and $V_2^{-/0}$ responsible for the recombination at low injection level and carrier generation within a depletion region [13]. However, at high proton implantation fluences, VOH centres start to dominate due to high density of the implanted hydrogen atoms [17, 18].

It has been shown that applied proton implantations provide 3-10 times lower leakage current than those obtained for standard alpha implantations, evaluated for the equivalent reduction of reverse current peak [19]. This is explained by lower production of divacancies. In the case of proton irradiations, divacancies dominate in creation of the carrier generation current within the depletion region. Hydrogen atoms, which are implanted at the projectile range during protons irradiation, also stimulate annealing of divacancies by suppressing formation of V_2O complexes. Therefore, the leakage current of proton irradiated diodes is significantly reduced after annealing at 350 ^oC. While, this current of diodes irradiated with alphas sustains its high value. On the other hand, some author's demonstrated a reduction of breakdown voltage in protons [20, 21] and helium ions [22, 23] implanted diodes after post-irradiation anneals in the range of 350-500 ^oC temperatures. This result was explained [20-23] by formation of thermal donors which increase positive charge within space charge region and, consequently, cause an enhancement of the electric field and accelerate impact

ionization. It was shown that the possibility of the avalanche breakdown is reduced by shifting the recombination layer away from the junction [24].

It was reported that ion irradiated diodes exhibit larger leakage current compared to those irradiated by electrons due to the higher production of divacancies in the case of ion irradiation [21]. Electron irradiations lead to the increase of forward voltage drop (U_F). Contrary, the lifetime local killing techniques provide reduction of reverse recovery charge collection keeping the lower voltage drop value. However, the higher doses, collected within a low doped n-base region, result in sharp and undesirable increase of U_F. This happens if conditions of high-level injection are violated within location of the largest damage. Electron irradiations can not properly shape the diode recovery characteristics which stay qualitatively identical to that of the non-irradiated diode [21]. Control of carrier local lifetime by using ion irradiations can speed-up the diode switching and soften the recovery by leaving enough charge on the cathode side. However, manipulation of the local lifetime, if applied exceptionally to the anode junction, does not determine desirable carrier distribution within the n-base during forward conduction regime, leaving the rather large injected charge in the middle of base width. This charge enhances the switching losses and the probability of dynamic avalanche. For this reason, local lifetime control has to be applied in combination with an additional local lifetime control or uniform lifetime control treatment. The only reasonable way for optimization of the ON-state losses is a precise setting of the axial lifetime profile. This lifetime distribution profile is devoted to decrease the excess carrier plasma density only in the necessary locations and, at the same time, to guarantee that the conditions of high-level injection will not be violated [21].

Platinum impurity atoms introduced within a substitutional site of Si lattice are the ideal recombination centres for the modification of recombination parameters [7]. Diffusion of platinum atoms occurs via interstitial configurations. A stable Pt impurity state is in its sustitutional site. Pt atoms acquire a substitutional state via reactions of $Pt_i+V \Leftrightarrow Pt_S$. Therefore, profiling of distribution of platinum atoms within diode structure can be

implemented by profiling of vacancies. The latter technique is successfully implemented by implantation of He ions [25]. This technique allows a reduction of the reverse current peak (I_{RP}) which appears during switching from forward conduction to the reverse blocking regime and avoiding of current swinging during recovery process. These phenomena are inherent for reverse recovery processes in standard He implanted devices. Also, the lower leakage current values are obtained in Pt in-diffused devices [26]. Therefore, combined platinum in-diffusion and radiation mediated (enhanced due to excess vacancies) formation of electrically active Pt traps technology is employed. However, a controllability of radiation enhanced platinum in-diffusion from Pt/Si source is limited. As a result, inappropriate scatter of dynamic parameters (especially of reverse peak current) is obtained for radiation enhanced Pt in-diffusion modified devices.

It has been also reported that breakdown voltage can be increased by compensating of the n-base doping close to the anode junction of power device [27]. This is achieved by local lifetime control using radiation enhanced palladium in-diffusion. Irradiations are performed by alpha particles at energies proper to achieve the stopping range in the base region close to the junction. Besides the compensation effect, the reduced carrier lifetime values are obtained within the palladium in-diffusion modified region, and this serves for reduction of the peak recovery current (consequently, of recovery losses) and provides soft recovery [28]. The introduced recombination centres show high thermal stability, however this technology requires the multiple procedures (diffusion, irradiation, anneals).

Hazdra et. al. reported that hydrogenation of platinum atoms can be implemented by protons irradiation [29]. Hydrogenation appears within protons projectile depth forming centres and complexes related to Pt and H. It is also shown that Pt atoms accelerate anneal of divacancies and vacancy–oxygen complexes. This provides another approach for engineering of recombination centre parameters. However, again multiple procedures of diffusion, implantation and thermal anneals are required.

2.3. Peculiarities of the operational characteristics in particle detectors

In high energy physics experiments semiconductor particle detectors of *pin* structure operating at full depletion regime are commonly employed for tracking the ionising particles. Semiconductor particle detectors were designed based on Ramo's theorem [30] which was first formulated for the design of vacuum tubes. The theorem is formulated from the moving charge and electrode electrostatic energy balance equation $Q_A V_A = -qV_q$ for the linear medium conditions to derive currents induced in external circuit by a moving charge in an ionising chamber:

$$i_A = \frac{dQ_A}{dt} = -\frac{q}{V_A}\frac{dV_e}{dt} = -\frac{q}{V_A}\left[\frac{dV_q}{dx}\frac{dx}{dt}\right] = qE_{qA}(\pm v_{q,kin}), \qquad (2.10)$$

with the weighting field $E_{q,A}=1/V_A(dV_q/dx)\approx 1/d$, at charged particle motion velocities $v_{q,kin}<<c/n$. The other symbols represent: Q_A is the induced charge on electrodes, V_A is a potential on electrode, while V_q is a potential of a moving charge q. Ramo's theorem describes the induced currents in a linear medium. It was shown [31-34] that Ramo's theorem can not be applied straightforwardly for the non-linear medium (semiconductor detectors). Thus the inhomogeneity of electric field, of charge relaxation, of recombination/generation and diffusion processes should be included. Furthermore, the analysis of current transients becomes more complicated in partially depleted detectors when variations of depletion boundary due to mentioned processes must be taken into account.

Ionising radiation creates the defects in semiconductor which provide a wide variety of levels within the bandgap that affect the detectors operational parameters [35-37]. The shallow levels change the effective doping (N_{eff}) density thus influencing the full depletion voltage $U_{FD}=d^2 q_e N_{eff}/2\varepsilon\varepsilon_0$. Moderately deep levels act as capture centres reducing the charge collection efficiency $CCE \sim Q(t)=Q_0\exp(-t/\tau_C)$ with carrier capture lifetime $\tau_C=1/\sigma_C v_T(N_T-n_T(t))$. Deep levels act as generation centres increasing the leakage current $I_g=q_e n_i w_d S/\tau_g$ with generation lifetime $\tau_g=2\cosh(E_T-E_i)/\sigma_C v_T N_T$ which is a source of noise within registered signal. The other quantities within above

expressions are as follows: $Q(t)$ – the collected charge, $Q_0(t)$ – the generated charge, σ_C – carrier capture cross section, v_T – thermal velocity, N_T – the density of traps, $n_T(t)$ – density of filled traps, q_e – the elementary charge, n_i – intrinsic carrier density, w_d – depletion width of the drift region, S – the area of the junction, E_T – the energy of trap level within bandgap, E_i – the intrinsic energy level position. Therefore, it is necessary to analyze the peculiarities of defects in irradiated diodes, their evolution, transformations, and to search for new approaches of improving the detectors structure and operational regimes.

Generation current and consequently parameters of carrier generation centres are controlled by measurements and analysis of current-voltage (I-V) characteristics. Value of full depletion voltage (U_{FD}) is determined either as a saturation point on the C-V characteristic [38] or by the transient current technique (TCT) using a kink-point on the characteristic of voltage dependent variations of the injected charge drift transients [39-43]. Having determined U_{FD} by the mentioned measurement procedures, the effective doping density N_{eff} is calculated using the relation $N_{eff} \cong 2\varepsilon\varepsilon_0 U_{FD}/q_e d^2$, which is valid only for a perfect diode. Carrier capture, emission parameters as well as concentration of defects are evaluated by Deep Level Transient Spectroscopy (DLTS) [44] or Thermo Stimulated Currents (TSC) [44-47] technique. The latter DLTS and TCT techniques are based on measurements and analysis of the capacitance or current changes caused by variations of the thermal emission rate of carriers from defect levels.

The straightforward analysis of C-V characteristics showed a decrease of U_{FD} at lightly irradiated n-type diodes and then an increase at higher ($>10^{13}$ cm^{-2}) fluences for detectors of high resistivity material [38]. Then it was inferred that effective doping concentration decreases at small irradiation fluences, changes its sign to p-type and finally starts to increase with enhancement of fluence. Furthermore the dependence of U_{FD} (extracted from C-V characteristics) on ac test signal of LRC meters was observed in heavily irradiated diodes [38], which clearly indicates the influence of carrier capture and emission processes for the measured C-V characteristics.

Current transients measured in heavily irradiated diodes by employing the TCT technique are obtained to be of double peak shape [48-50] which was proposed to be originating from the double peak electric field distribution within diode of *pin* structure drift region with its highest values at the p^+n and nn^+ junctions [51, 52]. The origin of this double peak electric field distribution was explained [50] by deep levels trapping of thermally generated electrons and holes at different sides of the drift region (electrons nearby nn^+ junction and holes nearby the p^+n junction) and consequently, resulting in different sign of space charge nearby the p^+n and nn^+ junctions. It was also proposed that the double junction effect at applied reverse voltages below U_{FD} appears [49, 50].

However, it is necessary to notice that the application of the above mentioned techniques becomes complicated at high irradiation fluences. Then C-V characteristics measured become distorted because of the phase shift measured by LRC meter is determined by generation current not by the change of capacitance, and simple models [53] based on equivalent circuits should not be applied for description of C-V characteristics. The model of TCT technique based on Ramo's theorem [30] has been also shown [31-34] not to be applicable for the analysis of under depleted diodes. Furthermore, when defects density exceeds that of dopants ($N_T >> N_D$), the radiation induced traps can only be partially filled. This phenomenon is illustrated in Fig. 2.2, where simulated variations of carrier capture (τ_C) and emission (τ_{em}) times as a function of trap level position in material with $N_D=10^{12}$ cm^{-3} are presented for different density of traps (N_T) [A13]. It can be seen that only deep traps with $\tau_C << \tau_{em}$ can only be filled when $N_T >> N_D$. Thus, DLTS and TCS techniques can not be applied at high irradiation fluences for correct evaluation of traps parameters.

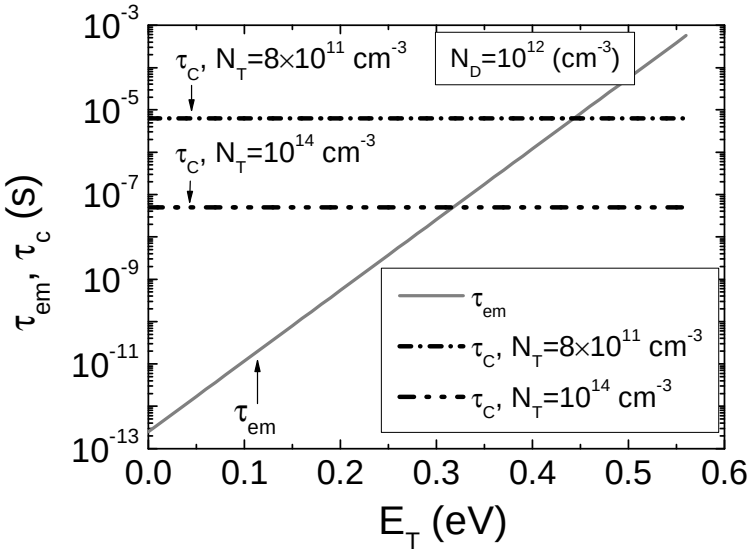

Figure 2.2. Carrier emission (τ_{em}) and capture (τ_C) lifetimes as functions of deep level position E_T in the upper half of forbidden-gap in the n-type (N_D=10^{12} cm^{-3}) material. Capture lifetimes are presented for N_T=8×10^{11} cm^{-3}< N_D and for N_T=10^{14} cm^{-3}>> N_D [A13].

Therefore, techniques capable to characterize heavily irradiated detectors, models capable to describe the peculiarities of current transients in detectors (taking into account the dielectric relaxation, trapping and recombination processes) and verification of widely accepted phenomenon of space charge sign inversion, are needed.

III. Sample preparation and characterization techniques

In this work several techniques were combined for the analysis of deep level spectra and of their variations with irradiation fluence and thermal anneals, for evaluation of the generation/recombination and trapping as well as transport parameters in irradiated power diodes and detectors. In this section basic principles of operation of these techniques are presented. First, sample preparation, surface passivation and primary characterization are described.

3.1 Preparation, passivation and primary characterization of samples

The preparation of samples for the irradiations, in order to modify the recombination and functional parameters of devices, is an important procedure. In this work initial material float zone (FZ) n-Si (which is employed for the production of diodes) wafer samples were prepared for the control of recombination parameters after irradiation while completely fabricated diode samples were prepared for the control of static and dynamic characteristics of a device.

The structure of FZ n-Si wafer substrates is sketched in Fig. 3.1 (a), and contains such layers: 60 μm – thickness n-Si layer of relatively large ρ=25 Ωcm resistivity and of N_D=1.74·10^{14}cm^{-3} dopants density, and n$^+$-Si 200 μm - thick layer of ρ=0.04 Ωcm low resistivity, containing N_D=3.37·10^{17}cm^{-3} donors density.

The diode structures were produced at enterprise “Vilniaus Ventos Puslaidininkiai” and had a structure, shown in Fig. 3.1 (b), with layers as follows (from left to right, in Fig. 3.1 (b)): Al electrode of 20 μm thickness, p$^+$-Si layer of resistivity of ρ=0.004 Ωcm with acceptors density of N_A=2.7·10^{19}cm^{-3}, and of thickness of 19 μm; n-Si layer of resistivity of ρ=25 Ωcm, of donors density of N_D=1.74·10^{14} cm^{-3}, and of thickness of 41 μm; n$^+$-Si layer of resistivity of ρ=0.04 Ωcm, of donors density of N_D=3.37·10^{17}cm^{-3} and of thickness of 185 μm; n^{++}-Si layer of resistivity of ρ=0.002 Ωcm, of donors density of N_D=3.4·10^{19}cm^{-3} and of thickness of 15 μm; Cr/Ni/Ag electrode of 20 μm thickness.

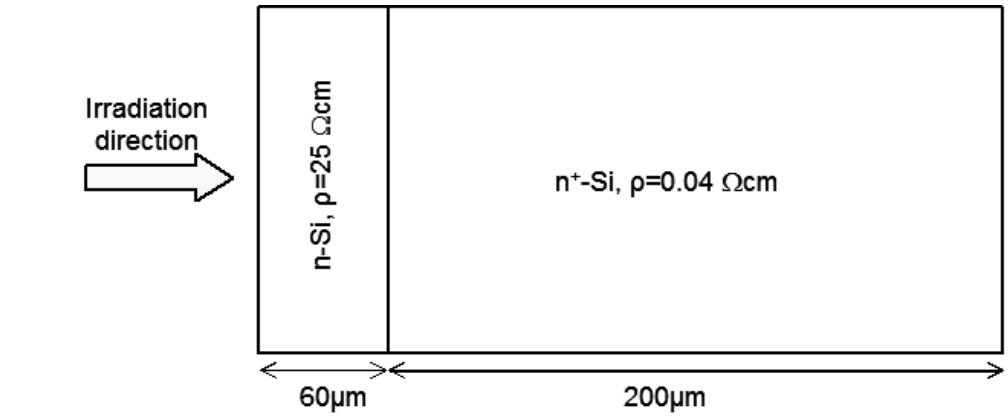

a

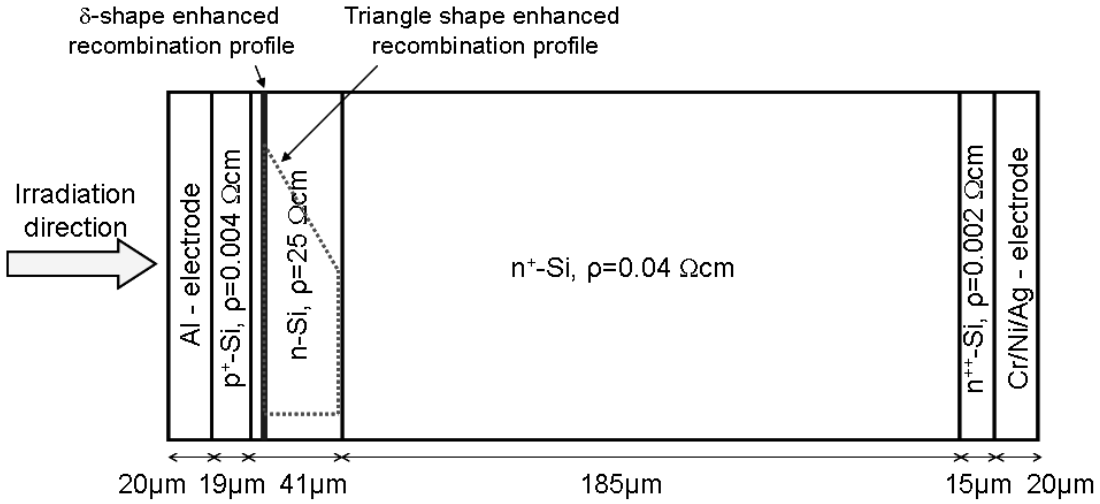

b

Fig. 3.1. Structure of FZ n-Si wafer samples (a) and diodes with indicated δ and triangle shape enhanced recombination regions (b).

The produced diode plates on 4 inch wafer substrate were cut into diode blocks of dimensions 21.04 mm × 19.95 mm each containing 20 diodes (Fig. 3.2 (a)), since only samples of that geometry were available to mount inside the irradiation chamber at Helsinki University Accelerator Laboratory (HUAL). Only six diodes (which is enough for characterisation), set in the centre of the block (highlighted in Fig. 3.2 (a)), were irradiated, to reduce the exposure procedure. The picture of the single diode is presented in Fig. 3.2 b. Samples of the initial FZ n-type Si for the irradiations were cut into blocks of the same dimensions as diode sample blocks. The diode blocks were cut into single devices after irradiations (Fig. 3.2.b).

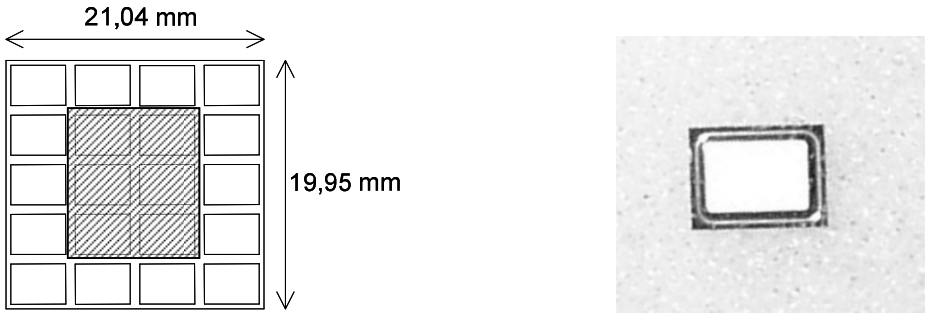

Fig. 3.2. a- Sketch of a block of diodes prepared for protons irradiation. The irradiated area in the middle of the block is emphasized. b- Picture of the diode.

Primary characterization of recombination parameters in FZ n-Si wafer samples was carried out by employing microwave probed photoconductivity transient technique. Carrier lifetime measurements allow one to evaluate the presence of technological defects (that might be introduced during each technological step especially when thermal operations – as diffusion of dopants, etc. are performed) and radiation defects [54]. When bulk carrier lifetime is relatively long, it can only be evaluated correctly when carrier surface recombination is suppressed by passivating the surface of the structure. Surface passivation might be implemented by growing thermal oxide [54]. However, the mentioned procedure is not very practical, especially, when carrier lifetime needs to be measured within each technological operation during production process of the device.

In our experiments, a wet surface passivation procedure by iodine-ethanol solution has been proposed. First, Si wafers were etched for 5 minutes in $HF : HNO_3 : H_3COOH = 28 : 4 : 10$ mixture to remove oxide and surface defects. Then Si wafers were placed into the plastic bag filled with iodine ethanol solution of the ratio 100 ml ethanol : 5 g iodine. The plastic bag and passivating iodine-ethanol thin layers are transparent for infrared excitation light and for microwaves probing the photoconductivity transients. Carrier recombination parameters had been extracted by measuring the microwave probed photoconductivity decays on the *in situ* passivated samples.

3.2. Standard device characterization techniques

3.2.1. Current-voltage and capacitance-voltage techniques

Diode current-voltage (I-V) characteristic for the ideal case is expressed by Shockley equation which consists of diffusion currents of holes (J_p) and (J_n) electrons [7,55]:

$$J_D = J_p + J_n = J_0\left[\exp\left(\frac{q_e U}{k_B T}\right) - 1\right] \tag{3.1}$$

where

$$J_0 = \frac{q_e D_p p_{n0}}{L_p} + \frac{q_e D_n n_{p0}}{L_n} = \frac{q_e D_p n_i^2}{L_p N_D} + \frac{q_e D_n n_i^2}{L_n N_A}. \tag{3.2}$$

Here q_e is the elementary charge, U – voltage applied, k_B – Boltzmann's constant, T – absolute temperature, D_p and D_n – diffusion coefficients of holes and electrons, respectively, n_i – intrinsic carrier density, L_p and L_n – diffusion lengths of holes and electrons, respectively, N_D and N_A – donor and acceptor concentrations, respectively.

For real diode structure, current in the forward biased junction consists of current components determined by generation/recombination $J_R=q_e g w_d=(q_e n_i w_d/\tau_g)\exp(q_e U/2k_B T)$ (where g is the generation rate), diffusion (eq. 3.1), high injection $J_T=2q_e n_{av} d/\tau_{HL}$ (with average carrier concentration n_{av} within diode drift region at high injection conditions) and series resistance (associated with the finite resistivity within quasi-neutral regions) effects. For a reverse biased junction, the current $J_g=q w_d n_i/\tau_g$ is determined by generation processes within the depleted region. Therefore, measurements and analysis of I-V characteristics allows of controlling the recombination/generation and diffusion parameters.

Differential of small signal capacitance is expressed as:

$$C = S\lim_{\Delta U\to 0}\left(\frac{\Delta Q}{\Delta U}\right) = S\frac{dQ}{dU}, \tag{3.3}$$

where S – the area of the junction, $dU=dU_R+dU_{bi}$ with U_{bi} – barrier height, U_R – applied reverse voltage. Assuming U_{bi} remains independent of external

voltage the capacitance can be measured in terms of the change of the applied voltage dU_R.

C-V characteristics are analyzed using depletion approximation [44] which must satisfy the following assumptions: i) there are no free carriers within space charge region; ii) non-depleted bulk region is everywhere neutral; iii) the boundary between the two mentioned regions is sharp. Then barrier capacitance of asymmetric p^+n junction is expressed by depletion approximation [44]:

$$C = \frac{\varepsilon\varepsilon_0 S}{w_d}. \tag{3.4}$$

Here

$$w_d = \sqrt{\frac{2\varepsilon\varepsilon_0 (U_R + U_{bi})}{q_e N_D}} \tag{3.5}$$

is the depletion width at applied reverse voltage U_R. Assuming $U_R >> U_{bi}$, the slope of C^{-2} vs. U_R provides the effective doping concentration:

$$N_{eff}(x) = \frac{2}{q_e \varepsilon\varepsilon_0 S^2} \left(\frac{C^{-2}}{U_R} \right)^{-1}. \tag{3.6}$$

In reality, the boundary between depleted and neutral regions is not abrupt. Free carrier density decreases approximately exponentially with the square of the distance from the boundary within the depletion region, at a rate characterized by the Debye length L_D:

$$L_D = \left(\frac{\varepsilon\varepsilon_0 k_B T}{q_e^2 N_D} \right)^{\frac{1}{2}}. \tag{3.7}$$

In applications of the profiling methods, the effective density of dopants N_{eff} is evaluated by controlling the slope of characteristic C^{-2}-U_R, and the resolution of depth variations of dopants density has a fundamental limit of the order of magnitude of $\pm L_D$ [44].

A profile of the effective doping distribution in the base of a device can be routinely determined by exploiting of w_d dependence on voltage: $w_d \sim U_R^{1/2}$. However, carrier generation from deep levels is present in the irradiated

material, therefore barrier capacitance charging current changes should be supplemented by generation current variations $i_g=q_e n_i S w_d/\tau_g$ with depletion width and carrier generation lifetime τ_g. In common LRC-meters, capacitance evaluation is based on measurements of small ac test signal u phase shifts due to displacement current, when amplitude of the response and of the reference signals are actually controlled at fixed ac period instants, and then capacitance values are extracted by simple algebra calculations. Consequently, the presence of the leakage current introduces considerable difficulties for direct interpretation of the C-V profiling results. Nevertheless, the profiling technique can be based on phenomenological analysis of current components: the displacement current $i_C=C(U_R)(du/dt)$ and generation current $i_g=q_e n_i S\delta/\tau_g$, respectively. The latter component accounts for the generation current within δ-width layer of enhanced defect density, which prevails within full current $i_T=i_C+i_g\approx i_g|_{ig>>iC}$, at relatively large dc voltage U_R. Thus, position of the tested layer is determined by $N_{eff}(x,U_R)$, while a peak of i_T may appear due to i_g. Magnitude of the LRC-meter response signal, which is proportional to this test current peak, is caused by a width of damaged layer δ and by the ratio of test signal frequency ω and generation lifetime τ_g, i.e. $\omega\tau_g$.

C-V characteristics are commonly measured by employing small signal impedance measurements based techniques. Since diode is non-linear element, equivalent circuits are employed for the extraction of parameters [56]. The equivalent circuit of the diode is comprised of junction capacitance C, conductance G and serial resistance r_S (Fig. 3.3 (a)) [45]. The conductance depends on diode leakage current. A serial resistance r_S is determined by the volume and electrodes resistance. The capacitance can be measured employing two regimes assuming that it has parallel conductance or serial resistance (Figs. 3.3 (b) and (c)).

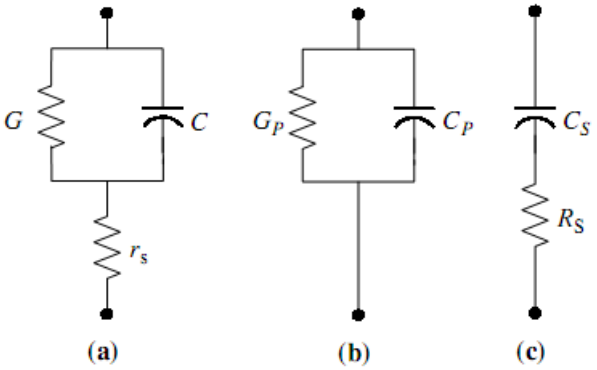

Fig. 3.3. Equivalent circuit of *pin* diode (a), equivalent circuits of measurement regimes by employing LRC meter – parallel (b) and serial (c).

The quantities of C_P, G_P, C_S and R_S can be expressed as:

$$C_P = \frac{C}{(1+r_S G)^2 + (\omega r_S C)^2}; \quad G_P = \frac{G(1+r_S G) + r_S(\omega C)^2}{(1+r_S G)^2 + (r_S \omega C)^2}; \tag{3.8}$$

$$C_S = C[1+(G/\omega C)^2]; \quad R_S = r_S + \frac{1}{G[1+(\omega C/G)^2]}. \tag{3.9}$$

Here, $\omega=2\pi f$ – angular frequency of the ac signal of LRC meter. The admittance of parallel circuit Y_P and impedance of a serial circuit Z_S are expressed as:

$$Y_P = G_P + j\omega C_P; \quad Z_S = R_S + 1/j\omega C_S, \tag{3.10}$$

Since $Y_P=1/Z_S$, then:

$$C_P = \frac{1}{1+D_S^2} C_S; \quad G_P = \frac{D_S^2}{1+D_S^2}\frac{1}{R_S}. \tag{3.11}$$

Here, $D_S=\omega C_S R_S$ is a dissipation factor. Similarly:

$$C_S = (1+D_P^2)C_P; \quad R_S = \frac{D_P^2}{1+D_P^2}\frac{1}{G_P}. \tag{3.12}$$

In the case of parallel circuit, the dissipation factor is $D_P = \frac{G_P}{\omega C_P}$. The dissipation factor of parallel and serial regimes can also be expressed through quality factor Q, which is a reciprocal quantity to D:

$$Q_S = \frac{1}{D_S} = \frac{1}{\omega C_S R_S}; \quad Q_P = \frac{1}{D_P} = \frac{\omega C_P}{G_P}. \tag{3.13}$$

It has been shown [45] that measurement of diode capacitance is correct when $Q \geq 5$. Then C_P coincides with C_S. When $Q<5$, a difference between C_P and C_S appears. Then the capacitance measurement is unacceptable. The quality factor might be small due to large G or r_S. The increase of G is obtained in heavily irradiated diodes containing generation centres.

Measurements of I-V characteristics in this study were performed by employing a commercial sub-femtoamp source-meter Keithley 6430 instrument. C-V characteristics were examined by using the small ac signal impedance measurement technique implemented by a high precision QuadTech 7600 LRC-meter. A computer controlled voltage bias source for the range of 0-500 V made of a set of batteries connected in series within a shielded box was exploited in order to arrange noiseless and galvanically insulated measurements. The latter source is inevitable for measurements of small ac signals within frequency range of 20 Hz – 2 MHz by employing high precision LRC-meter. Temperature dependent measurements were performed by placing a sample into a liquid nitrogen cryostat.

3.2.2. Deep level transient spectroscopy technique

Deep level transient spectroscopy (DLTS) technique allows evaluating the activation energy, concentration and capture cross-section of traps [44]. This technique is based on measurements and analysis of capacitance transients caused by trapping and emission of free carriers by defect associated levels. A diagram of the carrier capture and emission processes is shown in Fig. 3.4.

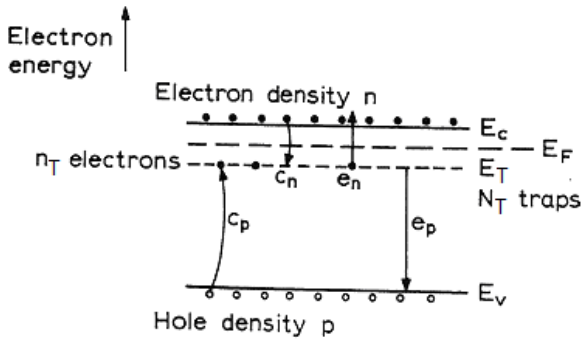

Figure 3.4. Diagram of carriers capture and emission processes for a trap with energy level E_T and density N_T containing n_T electrons [44].

Interaction between free carriers and deep centres is described by the rate equations:

$$c_n = \sigma_n \langle v_n \rangle n \,, \tag{3.14}$$

$$e_n = \sigma_n \langle v_n \rangle N_C \exp\left(-\frac{E_C - E_T}{k_B T} \right) , \tag{3.15}$$

$$c_p = \sigma_p \langle v_p \rangle p \,, \tag{3.16}$$

$$e_p = \sigma_p \langle v_p \rangle N_V \exp\left(-\frac{E_T - E_V}{k_B T} \right) . \tag{3.17}$$

Here, c_n, c_p are electron and hole capture rates, respectively. e_n, e_p denote electron and hole emission rates, respectively. σ_n, σ_p are electron and hole capture cross-sections, respectively. $\langle v_n \rangle$, $\langle v_p \rangle$ represent thermal velocities of electrons and holes, respectively. n, p denote free carrier density for electrons and holes, respectively; N_C, N_V represent density of states in conduction and valence bands, respectively. E_C is energy ascribed to conduction band minimum, while other symbols represent such quantities: E_V – valence band maximum, E_T – trap position within the bandgap, k_B – Boltzmann's constant, T – absolute temperature. It can be seen that carrier capture rates depend on free carrier density while carrier emission rates depend on trap position within the bandgap and on temperature. Thus carrier capture rates are the basic parameters of DLTS technique. Since $\langle v_n \rangle$, $\langle v_p \rangle$ are dependent on $T^{1/2}$, and while N_C, N_V are dependent on $T^{3/2}$, then e_n, e_p are proportional to T^2.

Variation of electron occupancy with time is expressed as:

$$\frac{dn_T}{dt} = \left(c_n + e_p \right)\left(N_T - n_T \right) - \left(e_n + c_p \right) n_T \,. \tag{3.18}$$

and a solution of Eq. (3.18) is:

$$n_T(t) = \frac{c_n + e_p}{c_n + e_p + c_p + e_n} N_T + \frac{e_n + c_p}{c_n + e_p + c_p + e_n} N_T \exp\left[-\left(c_n + e_p + c_p + e_n \right) t \right]. \tag{3.19}$$

It can be seen that, when the occupancy is deviated from equilibrium, n_T relaxes exponentially to its steady state with a rate constant $\tau^{-1} = c_n + e_p + c_p + e_n$.

Considering an asymmetric p^+n junction, the DLTS technique is implemented for the case of majority carrier traps in such a sequence. In the absence of reverse bias, traps are filled as carrier capture process dominates (c_n>e_n). When applied U_R causes a depletion region change, the emission process starts to dominate. The emitted electrons are extracted by the electric field from the depleted region by increasing the positive space charge in the depletion region, which increases the barrier capacitance. In asymptotic equilibrium (t=∞) when deep donors are empty within depletion region, charge of deep donors contributes to the shallow donors charge. Then, capacitance is expressed as:

$$C(\infty)=\left\{\frac{\varepsilon\varepsilon_0 S^2(N_D+N_T)}{2(U_{bi}+U_R)}\right\}^{\frac{1}{2}}. \tag{3.20}$$

For non-equilibrium case, when a system relaxes after trap filling, temporal variation of capacitance due to carrier emission is expressed as:

$$C(t)=\left\{\frac{\varepsilon\varepsilon_0 S^2(N_D+N_T-n_T(t))}{2(U_{bi}+U_R)}\right\}^{\frac{1}{2}}=C(\infty)\left(1-\frac{n_T(t)}{N_D+N_T}\right)^{\frac{1}{2}}. \tag{3.21}$$

A square root term in Eq. 3.21 can be expanded assuming N_T, n_T << N_D. Using Eq. 3.19 and c_n, e_p, c_p=0 conditions, the change of capacitance $\Delta C(t)$=$C(t)$-$C(\infty)$ can be expressed for the transient relaxation as:

$$\frac{\Delta C(t)}{C(\infty)}=-\frac{N_T}{2N_D}\exp(-e_n t). \tag{3.22}$$

It can be deduced that a differential capacitance value varies exponentially approaching to $C(\infty)$, as the carriers are emitted from the traps. The time constant of the capacitance transient gives the thermal emission rate, and the amplitude of the transient $\Delta C(0)/C(\infty)$, being equal to $N_T/2N_D$, gives a measure for traps concentration.

A peculiarity of DLTS method is to apply the “rate window” to a measured transient, which provides maximum output when time constant τ is equal to a known preset time constant τ_{ref}.

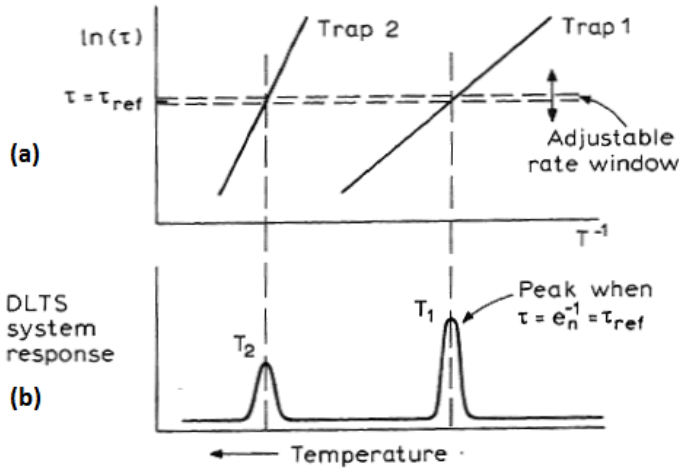

Fig. 3.5. Variations of the transient time constant $\tau=e_n^{-1}$ with reciprocal temperature for two different traps (a) and deep level spectrum which is produced by a rate window with reference time constant τ_{ref} [44].

The principle of operation of rate window is presented in Fig. 3.5. In the principle demonstration case, there are two different traps characterized by the linear relation between $\ln(\tau)$ and T^{-1}, however, having different activation energy E_{na} and capture cross-section σ_{na} values. As the emission rate increases with temperature, the peak occurs in the rate window output as $\tau=e_n^{-1}(T)$ by passing through τ_{ref} for each trap. By repeated scans with different values of τ_{ref}, sets of e_n values at fixed peak temperatures T_{pk} are obtained. These data sets are employed to plot the Arrhenius curves, representing the $\ln(e_n^{-1}T^2)$ dependence on T^{-1}. These Arrhenius plots are exploited for evaluation of E_{na} and σ_{na} parameters, determined for each trap. Either the plots of $\ln(e_n^{-1}T^2)$ versus T^{-1} or the sets of E_{na} and σ_{na} of parameters are called “trap signatures”.

In this work capacitance deep level transient spectroscopy measurements were performed by using a commercial spectrometer DLS-82E, to identify carrier generation centres. A temperature scan regime is usually employed to register spectra of deep levels.

3.2.3. Reverse recovery and forward voltage drop evaluation techniques

The reverse recovery transients were examined by using an industrial tester TA2050 installed at enterprise “Vilniaus Ventos Puslaidininkiai”. This

tester is designed for measurements of the reverse recovery time τ_{RR} values in the range from 10 ns to 4 µs. Reverse recovery time in diodes is commonly determined at 10 or 25% level relatively to the reverse recovery current I_{RP} peak value. Forward current peak values within pulses of duration of 30 µs for the reverse recovery time measurements can be varied within a range of 0.5 – 15 A. The ramp of current drop dI/dt is usually varied in the range of 10-50 A/µs. The reverse voltage of diode U_{RR} in this instrument can be fixed at values of 30 V, 50 V and 100 V.

Measurements of the forward voltage drop U_F are also performed by another industrial tester. Values of U_F on diodes are measured by applying current pulses of duration of milliseconds to prevent the tested diode against overheating. Values of the pulsed current are varied in the range of 0.5 - 20 A.

3.3. The developed device characterization techniques

3.3.1. Microwave probed photoconductivity transient technique

Microwave probed photoconductivity transient (MW-PCT) technique is commonly employed in our laboratory for the direct measurements and extraction of carrier lifetime values [54]. The specific instrumentation is designed and exploited for contactless scans of carrier lifetime in the simple carrier decay situations. The improved measurement regimes have been employed in this work for consideration of competing recombination processes in the systems of distributed parameters between surface and material bulk as well as for redistribution of carrier capture flows between recombination and trapping centres, by analyzing the shape and constituents of the photoconductivity relaxation transients.

MW-PCT technique is based on interaction of electromagnetic radiation and material, actually, the MW-PCT characteristics are modified due to absorption of microwaves by free carriers. For microwave region this interaction is described by Drude–Lorentz model when microwave frequency w_{MW} is much smaller than inverse lifetime of carrier scattering τ_{scat} ($w_{MW}\tau_{scat}<<1$). In this case, strength of interaction can be evaluated by

employing the absorption coefficient α_{MW} parameter, as the coefficient of free carrier absorption is nearly independent of frequency, being far from resonances. However, dispersion of the free carrier absorption determines the enhanced values of α_{MW} relatively to that for infrared light frequencies range α_{IR}, i.e. $\alpha_{MW} >> \alpha_{IR}$. Meanwhile absorption coefficient for infrared (IR) radiation α_{IR} is a function of frequency $\sim(w_{IR}\tau_{scat})^{-2}$. Thus, the higher sensitivity of registered signals is achieved for microwave probing regime compared to that for IR frequencies.

Variations of carrier concentration within the material modify the absorbed or reflected microwave radiation power. The amplitude of response of microwave probed photoconductivity transients U_{MW} as a function of excitation density and microwave radiation intensity can be written:

$$U_{MW} = \kappa[I_p \Delta K - I_n], \tag{3.23}$$

where I_p is the intensity of MW radiation, I_n – the intensity of scattered radiation noise, κ – the electrical signal transmission function of MW detector. The coefficient ΔK of MW power modulation due to light induced variations of material conductivity is expressed:

$$\Delta K = \frac{\Delta\sigma d\left[\sqrt{\frac{\mu_0}{\varepsilon_0}} + \frac{\mu_0}{2\varepsilon_0}\sigma_0 d + \frac{\mu_0}{4\varepsilon_0}\Delta\sigma d\right]}{\left[1+\left(\frac{1}{2}\sigma_0 d\sqrt{\frac{\mu_0}{\varepsilon_0}}\right)\right]^2\left[1+\left(\frac{1}{2}(\sigma_0+\Delta\sigma)d\sqrt{\frac{\mu_0}{\varepsilon_0}}\right)\right]^2}, \tag{3.24}$$

where ε_0, μ_0 are dielectric and magnetic permittivities, respectively, d – sample thickness. At equilibrium K depends on material conductivity when sample thickness and MW frequency are constant. At equilibrium, function $K(w)$ is at resonance when the denominator of Eq. 3.24 is minimal. The resonance of the MW system is achieved by adjusting the MW bridge, by varying the distance between sample and MW probe or by varying the MW frequency.

For the case of $\Delta\sigma/\sigma_0 << 1$ and $\Delta K/K << 1$, the change of MW power modulation is a linear function of conductivity changes $U_{MW} \propto \Delta\sigma \propto \Delta n$, where Δn is a concentration of excess carriers. When $\Delta\sigma/\sigma_0 > 1$, the characteristic of

MW absorption/reflection is a sub-linear curve, i.e. $\Delta K/K=1$, thus the amplitude of photoresponse saturates. MW-PCT measurements should be performed using a linear characteristic's regime when $\Delta\sigma/\sigma_0<<1$.

The measured transient photoconductivity response is determined by the decay of excess carrier concentration.

A sketch of instrumentation for implementation of the MW-PCT technique is shown in Fig. 3.6.

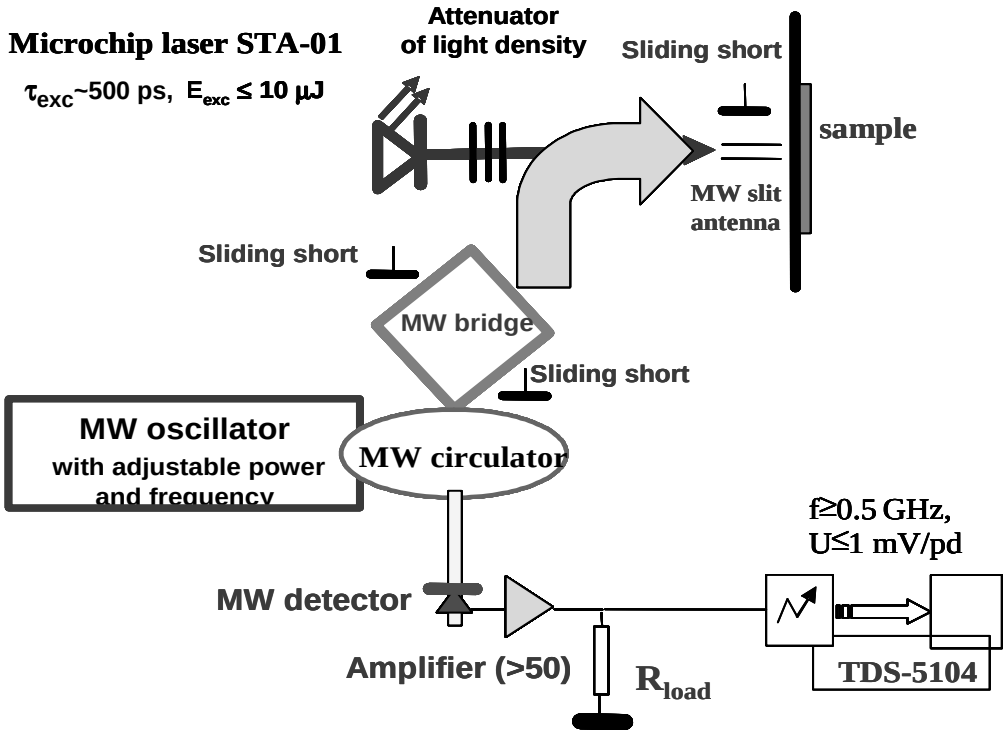

Fig. 3.6. Setup of MW probed photoconductivity transient measurement arrangement.

The instrument consists of the microwave bridge connected to either a slit or needle-tip antenna, of a microwave generator (Gunn diode), of a resonance chamber with microwave detector. Excess carriers are generated by a STA-01 microchip YAG:Nd laser with pulse duration of 500 ps at wavelength of 1062 nm. Excitation at 531 nm wavelength via single mode fiber is also applied when carrier lifetime variations within depth of wafer or layered samples are scanned on cross-sectional boundary of the sample. An excited area of the sample is probed by microwaves at 22 GHz by using either a slit antenna for depth integrated lifetime measurements or a needle-tip coaxial antenna for

cross-sectional scans to achieve high spatial resolution. The MW bridge is attenuated using sliding shorts to achieve a resonance of the MW system. The excess carrier decay transients are registered by using a 1 GHz oscilloscope TDS-5104. A PC computer is employed for control of the measurement procedure, and for data sampling, acquisition and recording.

In this work a surface passivation technology has been proposed and approved for MW-PCT measurements in rather thin samples with inherent rather long recombination lifetimes, when surface recombination cannot be neglected. For fast characterization of material recombination properties within the system of distributed parameters, the effective lifetime τ_{eff} approach is commonly used.

The effective lifetime τ_{eff} can be approximated by the phenomenological expression

$$\tau_{eff} = 1/[1/\tau_b + 1/(\tau_s + \tau_D)] \qquad (3.25)$$

being a result of both the bulk (τ_b) and the surface (τ_s) recombination components. The surface recombination can proceed after carriers diffuse to the surface during time $\tau_D = d_{eff}^2/\pi^2 D$. On the other hand, $\tau_s = d_{eff}/s$ can be expressed via surface recombination velocity s. Here, d_{eff} is the effective sample thickness and D is a coefficient of the carrier diffusion. Absolute values of τ_{eff} are rather good characteristics of the material and of surface passivation efficiency within qualitative analysis of recombination rates.

Values of carrier lifetimes of the 5.2 µs and of the 370 µs for non-passivated and surface passivated, respectively, have been obtained on pure FZ substrates by employing this IR microwave probed photoconductivity technique. Excess carrier decay transients measured on non-passivated wafer samples and samples passivated with iodine ethanol solution are presented in Fig. 3.7. The parameter of surface recombination velocity s has been evaluated being equal to 5.8×10^3 cm/s and 81 cm/s for non-passivated and passivated with iodine solution samples, respectively. The reduction of surface

recombination velocity to the value less than ≤100 cm/s indicates that surface recombination is considerably suppressed.

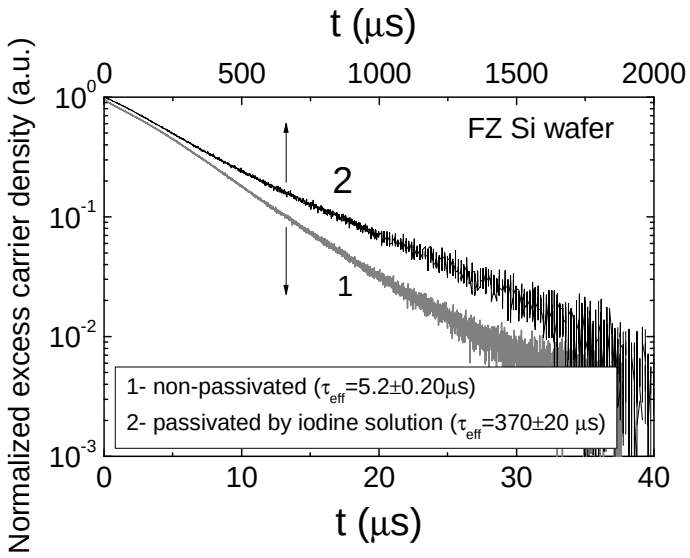

Fig. 3.7. Normalized excess carrier decay transients measured in non-passivated and passivated pure FZ initial Si material wafer samples.

Excess carrier decay transients measured on passivated and non-passivated initial FZ n-Si wafer samples (employed in this work) before irradiation are presented in Fig. 3.8.

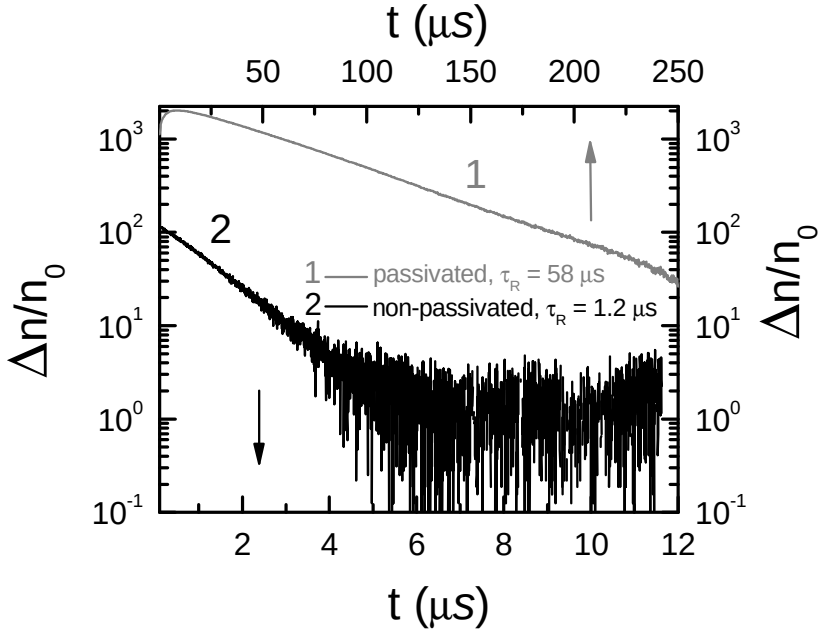

Fig. 3.8. Excess carrier decay transients measured in passivated and non-passivated FZ n-Si wafer samples.

It can be clearly seen that measured carrier lifetime is significantly increased in passivated sample, having value of τ_R=58 μs, relatively to a non-passivated sample, with τ_R=1.2 μs. After evaluation of bulk lifetime, the concentration $N_i=1/v_T\sigma_n\tau_R=1.6\times10^{12}$ cm^{-3} of intrinsic defects is evaluated, using $v_T=10^7$ cm/s and $\sigma_n\leq10^{-14}$ cm^2 values as known parameters. This intrinsic concentration of recombination centres is >10 times lower than dopants concentration ($N_D=1.74\times10^{14}$ cm^{-3}). Thus the initial FZ n-Si material is of sufficient quality for the formation of semiconductor devices.

3.3.2. Technique of barrier evaluation by linearly increasing voltage pulse

Barrier evaluation by linearly increasing voltage (BELIV) technique is based on measurements and analysis of barrier charging and charge extraction current transients. A sketch of measurement circuitry for implementation of different BELIV regimes is illustrated in Fig. 3.9. The measurement circuitry contains an adjusted output of a generator of linearly increasing voltage (GLIV), a diode under investigation, and a load resistor connected in series. Current transients are registered using a 50 Ω external resistor or load input of the Agilent Technologies DSO6102A oscilloscope. The other channel of the digital oscilloscope is exploited for synchronous control of linearity of a GLIV signal using a signal differentiating procedure installed within DSO oscilloscope. Linearity of the GLIV signal is essential within implementations of the BELIV technique.

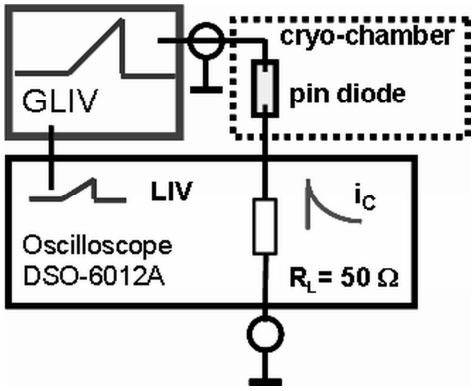

Fig. 3.9. Sketch of the measurement circuitry for implementation of the BELIV technique. GLIV - generator of linearly increasing voltage.

The diode under test is mounted on a cold finger within a vacuumed cryo-chamber for examination of the temperature dependent variations of BELIV characteristics, as sketched in Fig. 3.9.

3.3.2.1 Modelling of barrier charging pulsed characteristics

BELIV technique is implemented by analysis of current transients measured for reverse and forward biased junction. For reverse biased diodes, the BELIV technique is based on the analysis of barrier capacitance (C_b) changes with a linearly increasing voltage $U=At$ pulse. The C_b dependence on voltage and thereby on time t can be described using the depletion approximation [44] in the analysis of charge extraction transients in the trap-free material. This approximation leads to the simple relation $C_b=C_{b0}(1+U/U_{bi})^{-1/2}$ for an abrupt p^+n junction in the *pin* diode, where the barrier capacitance C_{b0} for the non-biased diode of area S is given by $C_{b0}=\varepsilon\varepsilon_0 S/w_0=(\varepsilon\varepsilon_0 S^2 q_e N_D/2U_{bi})^{1/2}$. Here, ε_0 is the vacuum dielectric constant, ε the material permittivity, q_e the elementary charge, U_{bi} the built-in potential barrier, $w_0=(2\varepsilon\varepsilon_0 U_{bi}/q_e N_D)^{1/2}$ is the width of depletion for non-biased junction, and $A=U_P/\tau_{PL}$ the ramp of the LIV pulse with amplitude U_P and of duration τ_{PL}.

The time dependent changes of the charge $q=C_bU$ within the junction, determine the current transient $i_C(t)$:

$$i_C(t)=\frac{dq}{dt}=\frac{\partial U}{\partial t}\left(C_b+U\frac{\partial C_b}{\partial U}\right)=\frac{\partial U}{\partial t}C_{b0}\frac{1+\frac{U_C(t)}{2U_{bi}}}{\left(1+\frac{U_C(t)}{U_{bi}}\right)^{3/2}}\cong AC_{b0}\frac{1+\frac{At}{2U_{bi}}}{\left(1+\frac{At}{U_{bi}}\right)^{3/2}}. \quad (3.26)$$

This transient contains an initial (t=0) step AC_{b0} due to displacement current and a descending component governed by charge extraction (Fig. 3.10 (a)). The latter component gives an additional relation to extract U_{bi} by taking the ratio $r_m=i_C(0)/i_C(t_m)\geq 1$ at a fixed time t_m. Subsequently the value of N_D ($N_{Deff}=N_D-N_A$) is evaluated by substituting the extracted U_{bi} in the initial current expression $i_C(0)=AC_{b0}$. To extract the barrier parameters more precisely, the

above mentioned procedure can be applied after the diffusion current is evaluated.

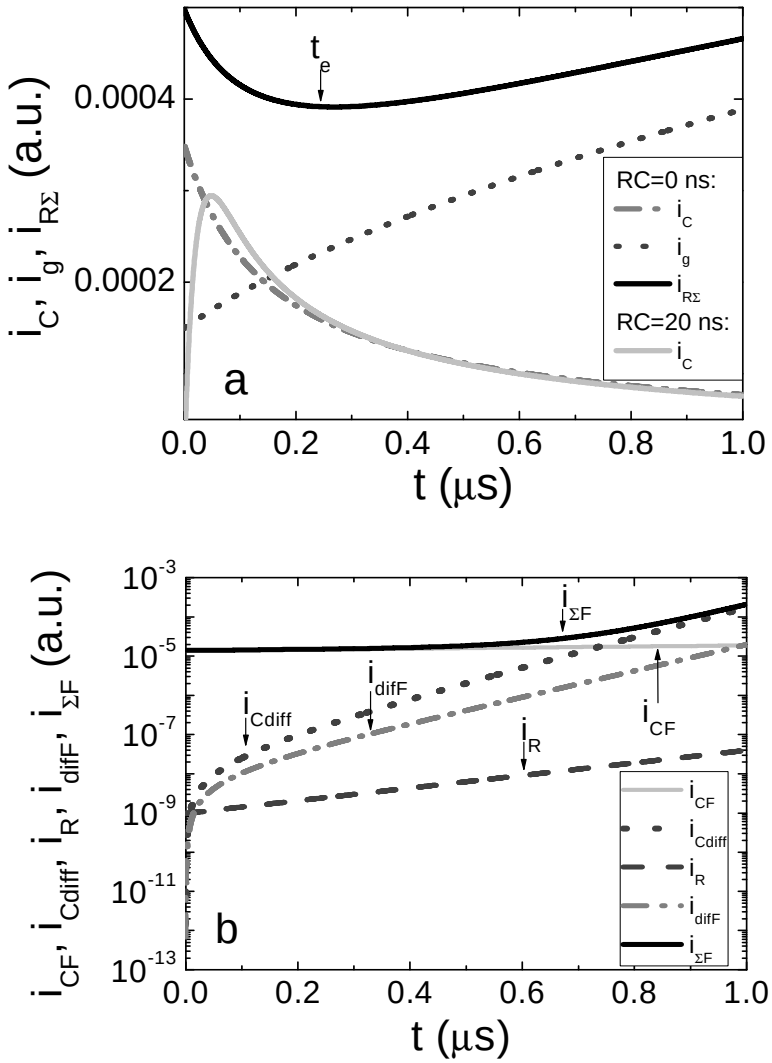

Fig. 3.10. Simulated barrier charging and charge extraction i_C, generation i_g, and total $i_{R\Sigma}$ current transients at reverse biased diode (a). The i_C component simulated using a convolution integral with RC=20 ns is also shown. Simulated barrier ($i_{CF}(t)$), diffusion (storage) capacitance charging ($i_{Cdiff}(t)$), recombination ($i_R(t)$) and injection/diffusion ($i_{difF}(t)$) currents at forward biased diode (b).

The diffusion current i_{diff} [A11, A13, A14] stabilises rapidly with reverse bias voltage. In reality, a delay in the initial part of the transient appears due to external circuit time constant and serial processes of dielectric relaxation within a boundary at quasi-neutral range of the non-depleted n-layer, drift and diffusion of carriers to complete the circuit. The resulting τ_{RC} modifies crucially the initial current step $i_C(0)$ by decreasing its amplitude $i_C(0)$ by a

factor $\exp(-t/\tau_{RC})$. The modified current $i_{CM}(t)$ transient, caused by τ_{RC}, is described by using the Green's function method [57,58] which leads to a convolution integral (with $\tau_{RC}=mRC$ dependent on the precision required)

$$i_{CM}(t) = \frac{1}{\tau_{RC}} \int_0^t i_C(x) \exp[-\frac{(t-x)}{\tau_{RC}}]dx \,. \qquad (3.27)$$

The qualitative changes of the transients, simulated by using Eqs. 3.26 and 3.27, are illustrated in Fig. 3.10 (a). It is clearly seen that both a reduction and a shift of the i_{CM}(t) peak appear. Fitting of the experimental transient $i_{CM}(t)$ by Eq. (3.27) with τ_{RC} as fitting parameter, allows extracting U_{bi} and C_{b0}.

3.3.2.2. Modelling of trap impact on barrier charging characteristics

In materials containing a considerable density of deep traps, modification of $i_{CM}(t)$ transient by τ_{RC} within the initial part appears to be more complicated when τ_{RC} is governed by carrier capture/release processes [44].

Radiation induced traps are responsible for a generation current [A11, A13, A14] within the depletion region. This current $i_g(t)=q_e n_i S w_0(1+At/U_{bi})^{1/2}/\tau_g$ increases with voltage $U(t)$ and can exceed the barrier charging current in the ulterior range of pulsed transient [A11, A13, A14] when the carrier generation lifetime τ_g is rather short. In a more detailed analysis of the impact of traps [44] on barrier capacitance changes with time, traps located below the mid-gap are assumed to be the compensation centres which modify the effective doping density (in the expressions for w_0 and C_{b0}). While deep centres, located in the upper-half of the band-gap, are able to rapidly response by majority carrier capture/emission which modifies the space charge in the time scale of the dielectric relaxation.

The transient of the total reverse current (including the diffusion current $i_{diff}(t)$) is described [A14] by the sum of the ($i_{R\Sigma}(t)= i_C(t)+ i_{diff}(t)+ i_g(t)$) currents:

$$i_{R\Sigma}(t) = AC_{b0}\frac{1+\frac{U_C(t)}{2U_{bi}}}{(1+\frac{U_C(t)}{U_{bi}})^{3/2}} + i_{diff\infty}(1-e^{-\frac{eU_C(t)}{k_BT}}) + \frac{q_e n_i S w_0}{\tau_g}(1+\frac{U_C(t)}{U_{bi}})^{1/2} \quad . (3.28)$$

In the diffusion current expression within equation (3.28) $i_{diff\infty}=q_e S n_i 2L_{Dp}/N_D\tau_p$, where $L_{Dp}=(D_p\tau_p)^{1/2}$.

The descending charge extraction and ascending generation current variation with LIV pulse time (voltage) implies [A11, A13, A14] the existence of a current minimum within the transient. The time instant t_e for this extremum can be found by using $\partial i_{R\Sigma}/\partial t|_{te}=0$ condition. This leads (at assumption $\partial i_{diff}(t)/\partial t=0$ for $t_e>>k_BT/q_eA$) to a relation for an extremum time instant t_e and to a minimal total current value, expressed by initial values of barrier charging $i_C(0)$ and generation $i_g(0)$ currents [A11, A14] as

$$t_e = \frac{U_{bi}}{Ai_g(0)}[\frac{i_C(0)}{4} - i_g(0) + \sqrt{(\frac{i_C(0)}{4})^2 + \frac{3}{2}i_C(0)i_g(0)}]. \qquad (3.29)$$

The initial current component ($i_{R\Sigma}(t)\approx i_C(t)+i_{diff}(t)>>i_g(0)$ for $t<<t_e$) can be used to determine the barrier U_{bi} by using Eqs. (3.26) and (3.27). Subsequently, the carrier generation lifetime can be determined by using Eq. (3.29). For a reverse bias LIV, a main voltage drop appears on the diode, and errors due to voltage distribution between diode and load resistor R_L can be ignored for small leakage currents, for small LIV voltages and for diodes with rather small barrier capacitance. The value of the GLIV voltage should be replaced by $U(t)=At-R_L i_{R\Sigma}(t)$ and voltage sharing between the load resistor and diode with consequent delay in $U_C(t)$ should be used during the second iteration of modelling. In a more rigorous approach, the non-linear differential equations and transcendental equations should be solved to simulate the variations of the BELIV transients.

Barrier current transients and their analysis become more complicated at forward biasing of a diode (a regime of minority carrier injection). In this case the voltage drop on a load resistor should be always included: $U_F(t)=At-R_L i_{\Sigma F}(t)$, to avoid phantom roots and poles within model equations. Generally,

current appears to be composed of the barrier ($i_{CF}(t)$) and of the diffusion (storage) capacitance charging ($i_{Cdiff}(t)$) currents and of recombination ($i_R(t)$) and injection/diffusion ($i_{difF}(t)$) ones, as (Fig. 3.10 (b))

$$i_{\Sigma F}(t) = i_{CF}(t) + i_{Cdiff}(t) + i_R(t) + i_{difF}(t) = \frac{\partial U_F(t)}{\partial t}[C_{b0}\frac{(1-\frac{U_F(t)}{2U_{bi}})}{(1-\frac{U_F(t)}{U_{bi}})^{3/2}} + \cdot$$

$$+ C_{diff\,0}(e^{\frac{q_e U_F(t)}{k_B T}}(\frac{q_e U_F(t)}{k_B T}+1)-1)] + \frac{q_e n_i w_0 S}{2\tau_R}(1-\frac{U_F(t)}{U_{bi}})^{1/2} e^{q_e U_F(t)/2k_B T} + \mathrm{i}_{diff\,0}(e^{q_e U_F(t)/k_B T}-1) \quad (3.30)$$

Here, additional symbols represent: $\tau_R=[1+2(n_i/n_0)\cosh(E_T-E_i)]/\sigma_c v_T N_T \approx 1/\sigma_c v_T N_T$, $i_{diff0}=q_e S n_i^2 D_p^{1/2}/N_D \tau_p^{1/2}$, $C_{diff0}= i_{diff0}/(dU/dt) \cong i_{diff0}/A$. The storage (diffusion) capacitance is routinely assumed to be $C_{diff}=d(\int_0^t i_{diff0}(\exp(q_e U(t')/k_B T)-1)dt')/dU$. At forward bias LIV, the initial stage of the BELIV transient is governed by a barrier capacitance current (first constituent in Eq. (3.30)), which rather slowly increases with $U_F(t)$. At $t \cong 0$, i.e. for $q_e U_F(t)/k_B T \approx 0$, diffusion capacitance and diffusion current are close to zero. Thus, at low injection level regime, the barrier capacitance component prevails over the diffusion and recombination current constituents within initial stage of the current transient. The geometrical capacitance determines the initial step and capacitor like BELIV transient behaviour, when a diode is fully depleted without external voltage. However, contrary to reverse biasing (Eq. (3.28), where charge extraction causes a negative constituent $U_R(dC_b/dU_R)$, the barrier capacitance current component shows a positive derivative $U_F dC_b/dU_F>0$ for the forward biased diode. This is determined by a denominator function within the first constituent of Eq. (3.30). The amplitude of the BELIV current, during rearward phase of BELIV current transient, exponentially increases due to i_{Cdiff} and i_{difF} for the short LIV pulses. Thereby both the barrier capacitance ($i_{CF}(t)$) charging current and the total current ($i_{\Sigma F}(t)$) increase with LIV. Actual voltage drop on a diode $U_F(t)=At - R_L i_{\Sigma F}(t)$ deviates from a linear increase, when $i_{\Sigma F}(t)$ is enhanced, even in the case when GLIV signal is perfect. This requires a solution of voltage sharing equation.

Then, the initial increase of $i_{CF}(t)$ is additionally modified by the RC_{b0} parameter of a circuit. Actually, only numerical simulations of time-dependent current $i_{\Sigma F}(t)$ variations should be employed for the precise evaluations of barrier parameters at elevated voltages.

3.3.3. Induced charge collection current techniques

Induced charge diode current (ICDC) and injected charge collection current (IChCC) techniques are based on measurements and analysis of current transients due to light induced surface charge domain photo-generated by a short laser pulse. This method allows evaluating carrier drift, diffusion and recombination parameters in diodes after and during irradiation. The circuitry for the implementation of current transient technique is presented in Fig 3.11.

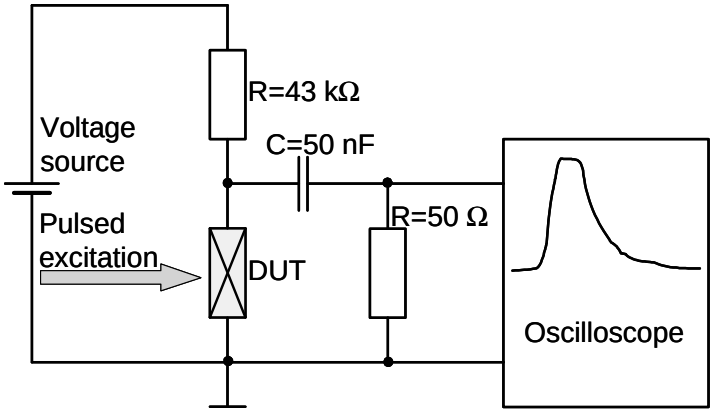

Fig. 3.11. ICDC/IChCC measurement circuitry. DUT is the diode under test.

The reverse bias on the diode is applied by a sub-femtoamp source-meter Keithley 6430. Excess carriers are generated by STA-01 microchip YAG:Nd laser pulse of duration of 500 ps at wavelength of 1062 nm for bulk and at 531 nm for surface excitation. The current transients are measured on 50 Ω load resistor and registered by Tektronix oscilloscope TDS-5104.

To determine the peculiarities of currents, it is necessary to examine variations of current transients as a function of the reverse voltage U_R at fixed excitation density n_{ex} (Fig. 3.12 (a)) and varying excitation intensity at fixed reverse voltage (Fig. 3.12 (b)). The enhancement of U_R shortens the duration and increases the amplitude of current transient due to larger charge $q=CU_R$

which can be extracted by electric field. Here, C is geometrical diode capacitance. The enhancement of n_{ex} increases the amplitude and duration in the rearward part of transient when $q>>CU_R$, because only charge $q=CU_R$ can be extracted by the electric field. The leftover carriers screen the electric field and diffuse towards the electrode before being extracted. In the presence of recombination centres, diffusion and recombination processes compete.

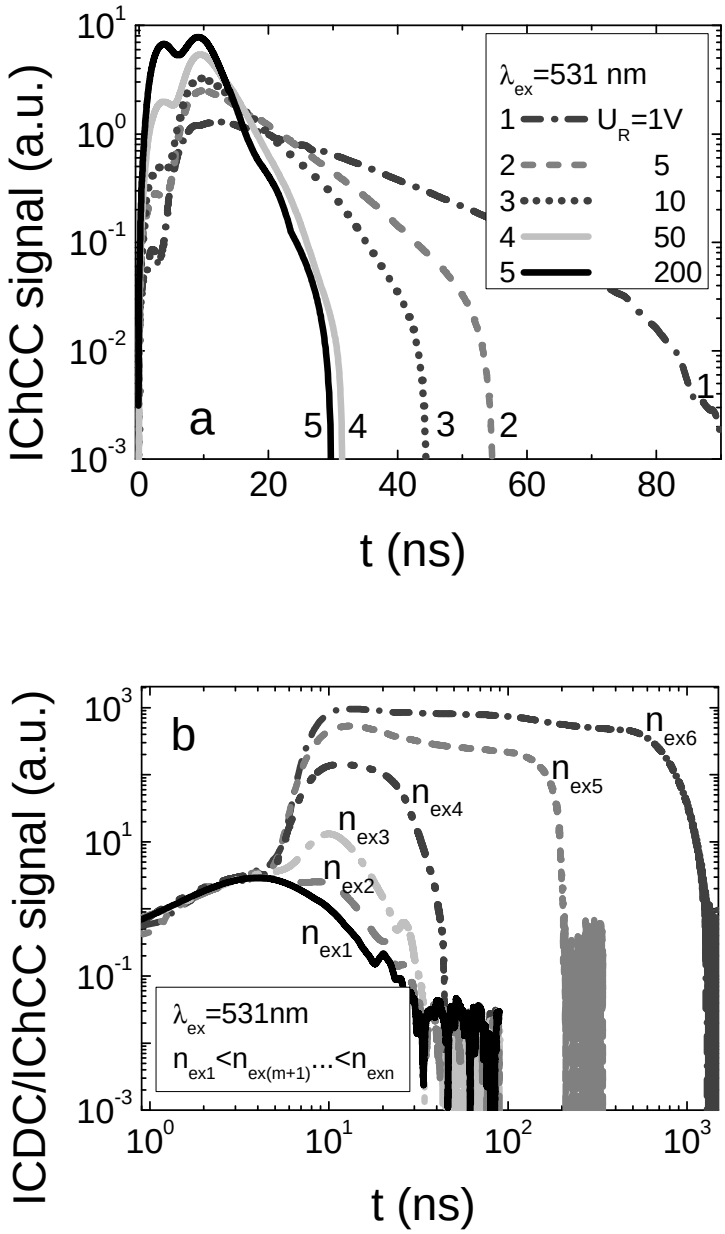

Fig. 3.12. Current transients measured in non-irradiated diode as a function of reverse voltage U_R at constant excitation density (a) and as a function of excitation density at fixed U_R=70 V (b).

3.3.3.1 Modelling of the induced charge pulsed current characteristics

In order to understand the nearly independent shape and duration of ICDC transients and to validate the procedures used to extract material parameters, the formation of the injected charge induced diode current (ICDC) transients require a more detailed discussion.

A sketch of the electric field distribution within the n-base of the diode under injected excess carrier pairs (n_{ex}=p_{ex}) is shown in Fig. 3.13. For applied voltages U_R<U_{FD}, current flows in the external circuit due to simultaneous extraction of majority carriers from the electrically neutral n-base and p^+ regions caused by separation of the injected excess carrier pairs due to the steady-state field and extraction of excess holes from the n-base region into the p^+ region. During this process, the first peak within the ICDC transient appears.

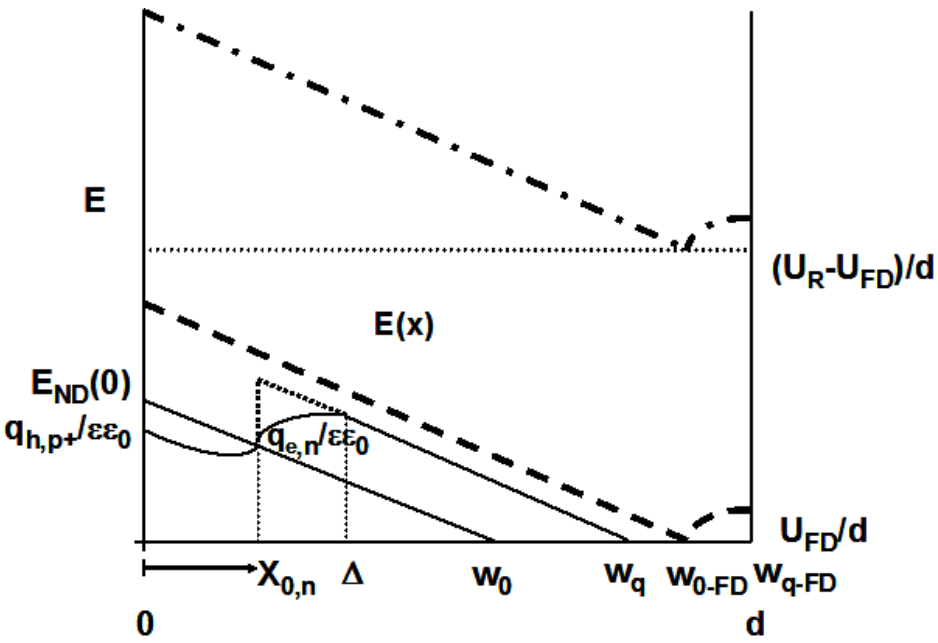

Fig. 3.13. A sketch of electric field distribution due to induced surface charge for different applied dc voltage values: U_R<U_{FD} – dotted and solid lines, U_R≅U_{FD} and w_q=d – dashed line, U_R>U_{FD} dash-dotted line. For U_R<U_{FD}, the enlarged details of field distribution are shown, where dotted line is attributed to an induced surface-charge field $q_{e,n}/\varepsilon\varepsilon_0$, while the solid line represents an excess carrier charge domain of width Δ.

The separation process induces a change of depletion width w_q (an increase relative to its steady-state value w_0) due to the surface domain field –

$q_{e,n}/\varepsilon_0\varepsilon$ of excess electrons. The extracted excess holes located at the p^+-side produce the same value of surface field. Thus, the overall charge balance ($w_{p+}N^-_{A,p+}=w_nN^+_{D,n}$ together with $q_{h,p+}X_{0,p+}=q_{e,n}X_{0,n}$) in the diode is maintained where $X_{0,p+}$ and $X_{0,n}$ - separation lengths of surface charges within p^+ and n regions, respectively. This balance in the n-base is supported by the applied dc voltage (U_R), together with the surface charge $q_{h,p+}/\varepsilon_0\varepsilon$ (in the p^+ layer, $X_{0,p+}<X_{0,n}$), if the $q_{e,n}$ domain is separated by $X_{0,n}$ from metallurgic boundary within the depleted region w_0 of the n-base. Then for $U_R<U_{FD}$, using the standard depletion approximation in device physics e.g. [7, 44], the depletion width is

$$w_q = \sqrt{\frac{2\varepsilon\varepsilon_0}{q_e N_{Deff}}(U_R + \frac{(\pm)q_{e,n}}{\varepsilon\varepsilon_0}X_0)}\,. \tag{3.31}$$

A sketch of the electric field distribution is illustrated in Fig. 3.13 by the dotted-line, for a surface charge $q_{e,n}$ separated by a length X_0. Here, a "depletion width" (w_0, w_q) means trivially that the material is electrically neutral (the potential together with the electric field are zero) at this point, e.g. [44]. The ICDC flows during $q_{e,n}(t)$ relaxation, (for instance due to capture by deep centres of excess electrons within the depleted n-base region), and changing of the separation length $X_{0,n}(t)$ (e.g., due to capture of excess holes in the depleted p^+ region and drift), until w_q recovers to w_0. The latter relaxation process can be found using condition for a duration of the domain drift within the space charge region $\int_{-t_0}^{t_{dr}} dt = \int_0^w [1/\mu E(x, q_{e,n}, X_0)]dx$. The temporal variation of the surface charge domain is clearly non-exponential, and should be described by the solution of a transcendental equation

$$q_{e,n}(t) = q_e N_{Deff} w_q(t) - \left[\frac{q_e N_{Deff} X_0(t)}{1-\exp\left(\frac{t+t_0}{\tau_M}\right)}\right]. \tag{3.32}$$

Here, t_0 is the duration of the induced carriers separation and formation of the $q_{e,n}$ domain, $\tau_M=\varepsilon_0\varepsilon/q_eN_{Deff}\mu_e$ is the dielectric relaxation time, $N_{Deff}=n_0$ is the

effective doping density. Infinitely narrow injected surface-charge, sketched by the dotted-line in Fig. 3.13, is an idealization.

In reality, a close to exponentially decreasing profile of the excess carrier density is induced by a light pulse. Thus, the excess carrier domain induced surface field can be found by combining the Poisson and Gauss integrals, and it can be evaluated as

$$E = q_e n_{ex0} \alpha^{-1} \frac{[1 - \exp(-\alpha\Delta)]}{\varepsilon_0 \varepsilon}. \qquad (3.33)$$

Here, α is the light absorption coefficient at the excitation wavelength, n_{ex0} is the excess carrier density photo-generated at the base layer surface and Δ is the effective width of the light injected charge domain. The latter should be taken as $\Delta = 5\alpha^{-1}$ if the averaged carrier density is to be controlled with a precision of 1% relative to n_{ex0}. The solid line in Fig. 3.13 shows the electric field distribution including the spreading of the injected surface charge domain. This spreading of the injected surface charge domain is the main reason for the transient of double peak shape formation, if the applied voltage approaches U_{FD}.

The first peak in the ICDC signal is again associated with excess hole extraction into the p^+ layer and simultaneous majority (p_0) hole extraction from the electrically neutral p^+ layer (with w_{p+} increment) towards metallic electrode and the external circuit. The second peak in the ICDC transient appears due to $w_q = d = w_{q,FD}$ at full depletion. At full depletion voltage (U_{FD}), the steady-state electric field is zero at $x_{FD} = w_{q,FD} - w_{0,FD}$. Thus, the last stage of excess carrier extraction runs within the increasing field region, i.e. self-acceleration of excess electrons appears to collapse the excess carrier domain at the external electrode (n^+ layer) (relatively to the base region). A similar (but opposite) effect appears in the extraction of excess holes from the n-base. These holes, extracted and localized at the p^+ layer ($X_{0,p+} < X_{0,n}$), reduce the steady-state field at $x=0$ (by an extent $q_e p_{ex0} \alpha^{-1} / \varepsilon_0 \varepsilon$) and slow down their later extraction. Therefore the ICDC initial peak is smoothed. The double peak transients inherent for ICDC are observed [A12, A16, 39]. As discussed above, a rather

"corrugated" electric field distribution appears for applied voltages $U_R \leq U_{FD}$. An enhancement of U_R above U_{FD} leads to an approximately uniform field distribution through the base of the *pin* diode, and the electric field is supported by planes of charge located at the external contact layers. The parallel plate condenser approximation can then be employed. At a fixed external voltage the electric field distribution within the considerably over-depleted base of the *pin* detector approaches a constant value, independent of depth within the base region. Operation of the diode with injected charge becomes similar to that of a capacitor in this case.

The smoothing of the field at $U_R > U_{FD}$ enables one to simplify evaluation of the mobility of excess carriers by using the well-known relation $\mu_e = d^2/\tau_{tr} U_R$ and drift time τ_{tr} measurements within the ICDC pulse. To evaluate changes of material during irradiation, measurements of carrier mobility at excess carrier densities $n_{ex} < n_0$, close to that values in dark are preferable, therefore the least possible excitation densities were maintained in our μ_e measurements. Commonly the drift time is evaluated as the time interval for the time of flight (TOF) pulse (at $U_R > U_{FD}$, when $\tau_{tr} < \tau_M$).

The ICD current, associated with the injected excess electron charge domain, for $U_R \leq U_{FD}$, varies due to temporal changes in $w_q(t)$. As $w_q(t)$ contains the product of the induced charge relaxation $q_{e,n}(t)$ (due to carrier capture to traps) and the pair separation length $X_0(t)$ parameters and the space charge density $N_{Deff}(t)$ changes (due to fast thermal emission from filled traps), the ICD current is generally composed of three components. Using the depletion approximation, this is [A12]

$$i_{ICD}(t) = \frac{C(t)U_R}{2} \frac{\left(\left(w_q(t)\right)_{U_R=0}\right)^2}{w_q^2(t)} \left[(\mp) \frac{v_{q,n}(t)}{X_0(t)} + \frac{1}{\tau_{capt}} + \frac{w_q^2(t)}{\left(\left(w_q(t)\right)_{U_R=0}\right)^2} \frac{(\pm) n_d(t)}{N_{Deff}(t)} \frac{1}{\tau_{em}} \right]. \quad (3.34)$$

Here additional symbols represent: $C(t) = \varepsilon_0 \varepsilon S / w_q(t)$, τ_{capt} is the excess carrier ($q_{e,n}$) capture lifetime within depleted region, τ_{em} is the carrier thermal emission

lifetime within depleted region, $n_d(t)=n_{d0}\exp(-t/\tau_{em})$ is the density of carriers trapped on the fast emission centres, $[(w_q(t))|_{UR=0}]^2 = 2q_{e,n}X_0/q_eN_{Deff}$, S is the area of a junction. The first component in $i_{ICD}(t)$ represents variations of separation length (for $v_{q,n}=dX_0/dt\neq 0$), and it is analogous to Ramo's [30] current within dielectric space between plates of capacitor. To keep this analogy, possibility of both ($\mp$) directions of drift current is denoted in Eq. (3.34), depending on induced charge sign and on direction of charged particle motion. The expression of this displacement current component, due to drift of charge domain within space charge region of a diode, is more complicated than that for the Ramo's current ($i=q_ev/w$) [30, 32], and it is governed by the barrier capacitance $C(t)$ temporal changes and depends on the ratio of the depletion width changes caused by the moving charge domain $q_{e,n}$ and normalized to space charge q_eN_{Deff}, as $[2q_{e,n}X_0/q_eN_{Deff}]/[(2\varepsilon\varepsilon_0/q_eN_{Deff})(U_R+q_{e,n}X_0/\varepsilon\varepsilon_0)]$. The second component of current within Eq. (3.34) is ascribed to excess carriers capture process (for $dq_{e,n}/dt=q_edn_{ex,S}/dt=-q_en_{ex,S}/\tau_{capt}$) within the depleted n-base region. It can be also deduced, that an enhancement of excess carrier density (of the $2q_en_{ex}/q_eN_D$) would be preferential to clarify the excess electrons trapping processes. The third component in Eq. (3.34) appears, when an influence of the fast carrier generation centres within space charge region is significant. Here, both ($\pm$) donor (+) and acceptor (-) type traps can be involved. Impact of the slow (deep) generation centres appears as a leakage current $i_g(t)=q_en_iw_q(t)S/\tau_g$. Including recombination/diffusion i_R [7] currents within n^+ and p^+ layers, the total diode current $i_\Sigma(t)$ can be expressed through a sum of the mentioned components: $i_\Sigma(t)=i_{ICD}(t)+i_g(t)+i_R(t)$.

There are several regimes of ICD current measurements (to clarify carrier capture/diffusion), depending on the ratio q_en_{ex}/q_eN_D. The n_{ex} density also determines the fraction of carriers (n_{tr}) which can be moved by the electrical field of the depleted barrier capacitance. For $n_{ex}\rightarrow n_0=N_D$ and $U_R\leq U_{FD}$, the current contains components $dq_{e,n}/dt$ and dX_0/dt, due to the external electric field during initial instants and the ambipolar diffusion of the

quasi-neutral domain of excess carriers after this electric field is screened. As a measure for the ratio of the carrier density which decays through carrier diffusion-recombination ($n_{D\text{-}R}$) and of that disappears from the depletion region via drift (n_{tr}) can be a threshold value of charge affordable to shift by applied dc external voltage. Carrier density involved in charge transit is evaluated by using the depletion approximation for a parallel plate capacitor of area *S*, and expressed as

$$n_{tr} = \frac{\varepsilon\varepsilon_0 U_R}{q_e w_q \Delta}. \tag{3.35}$$

Actually, the external electric field is rapidly screened (during a dielectric relaxation or transit time $\tau_{tr} = d^2/\mu U_R$ for carriers of mobility μ, if $\tau_{tr} << \tau_R$) owing to light generated excess carriers n_{ex0}, and n_{tr} vanishes ($n_{tr} \to 0$) within the initial transient stages if $n_{ex0} \approx n_0$ is sufficiently large.

3.3.3.2 Modelling of the charge collection pulsed characteristics

The light induced domain of excess electrons of large density is able to dissipate through (be collected at) the n^+ electrode due to diffusion across the base and carrier extraction by the electric field at the external electrode. The simplified approximation of carrier domain drift and diffusion process can be described by a classical expression [59] for carrier density variations dependent on time and position as:

$$n_{R-D}(x,t) = (n_{ex0} - n_{tr}(t)) \frac{\Delta}{\sqrt{4\pi D_A t}} \exp\{-[\frac{(x-\mu E t)^2}{4 D_A t} + \frac{t}{\tau_R}]\}. \tag{3.36}$$

Here, n_{ex0} is the initial (t=0) density of bipolar photo-excited carriers, D_A is the coefficient of carrier ambipolar diffusion. Depending on the probing (either through electrodes – IChCC or by microwave antennas MW-PCT-E) regime, the signal is sensitive either to carrier density at the collecting electrode ($n_{R\text{-}D}(t,d)$) or depth integrated carrier density $(1/d)\int_0^d n_{R\text{-}D}(t,x)dx$ for IChCC or MW-PCT-E response, respectively. In the *pin* diode, n^+ electrode collects electrons (and blocks holes), hence the injected charge collection current (IChCC) is measured. The MW-PCT-E transient appears as a relaxation pulse

with a vertex characterized by the descending slope of a trapezium-like pulse serving for the extraction of recombination lifetime.

At a rather high excitation density, $q_e n_{ex} \Delta > CU_R$, and low applied voltage the IChC current transient acquires a rising peak pulse shape with very small amplitude at initial instants and effective lifetime at the IChCC pulse vertex evaluated as $\tau_S=(\tau_D^{-1}+\tau_R^{-1})^{-1}$ with carrier recombination (τ_R) and diffusion $\tau_D \cong d^2/4\pi^2 D_A$ times.

The modelled and discussed peculiarities of induced charge determined current transients and of charge collection transients agree well with those experimentally recorded pulse variations, illustrated in Fig. 3.12.

Summary of the main results described in the chapter
[A1, A11, A13, A14, A16, A19, A20]

The proposed and employed in this work chemical surface passivation technique by iodine ethanol solution increases the effective recombination lifetime τ_{eff} from 1.2 μs for non-passivated to 58 μs for passivated FZ n-Si wafer layer of 60 μm width. This surface passivation technique is efficient for characterization of thin samples with rather long carrier bulk lifetime by using MW-PCT contactless technique. The developed measurement technique enabled evaluating of the concentration of intrinsic defects N_i of the order of magnitude of 1.6×10^{12} cm^{-3}.

A number of standard material and device characterization techniques (I-V, C-V, DLTS) employed in this work have been briefly described by demonstrating application range and restrictions for identification of the induced defects and their distribution within layered structures as well as for evaluation of operational device characteristics.

Several new techniques (BELIV, ICDC, IChCC) based on pulsed current transient measurements, grounded on induced charge domain and of pulsed biasing modification of current pulses, have been proposed, approved and applied.

The models of pulsed charging current transients, by analyzing the displacement as well as carrier drift, diffusion and generation components within changes of barrier and storage capacitance of junction structures, have been created for a design of transient techniques for evaluation of the operational particle detectors parameters and irradiated material characteristics in a wide range of induced charge densities and applied bias voltage pulse parameters. It has been demonstrated that fast electric field redistributions either by the barrier capacitance charging or by induced surface charge domain can be efficiently considered by using approach of temporal changes of the depletion width or surface charge on electrodes within junction structures. In the case of induced surface charge domain caused current pulses contain the displacement component equivalent to Ramo's current. The drift and diffusion current components, appearing due to carrier capture/thermal emission or other factors, scale the boundary of depletion width (between the space charge and neutral layers within structure with temporally varied electric field redistribution).

IV. Evaluation of radiation damage in particle detectors after irradiations

4.1. Samples and irradiations

A set of magnetic field applied Czochralski (MCZ) grown, high resistivity Si p^+nn^+ pad-detectors with active area of 5×5 mm^2 irradiated by reactor neutrons with fluence Φ in the range of 10^{12} - 10^{16} cm^{-2} was examined to clarify displacement damage factors and their impact on the operational characteristics of detectors.

The structure and a picture of detector are presented in Figs. 4.1 (a) and (b), respectively.

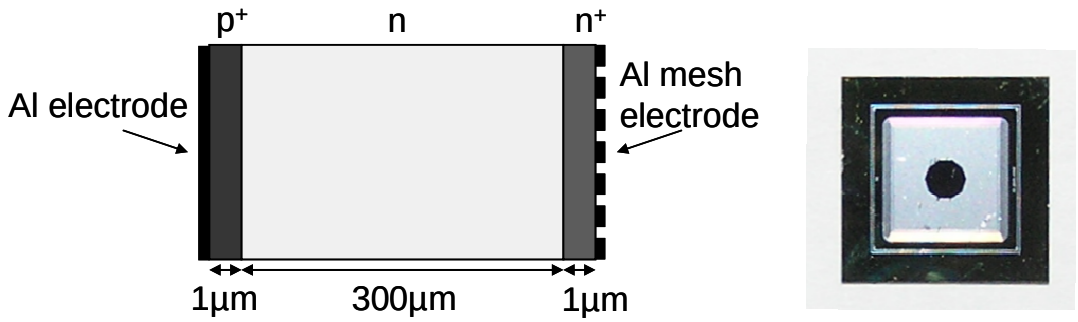

Fig. 4.1. The structure (a) and view (b) of investigated particle detectors.

The detector structure is composed of 300 μm thick high resistivity (N_D~10^{12} cm^{-3}) base region and 1 μm thick highly doped p^+ and n^+ regions which are formed by implantation. The structure has a solid metallized and the mesh Al electrodes on anode and cathode sides, respectively. Additionally, the pad-detectors contain a non-metallized hole of a diameter of ~1 mm within a centre of the main junction electrode for light excitation.

4.2. Current-voltage and capacitance-voltage characteristics

The I-V characteristics measured at room temperature by a Keithly-6430 electrometer show an increase of leakage current with irradiation fluence within a reverse bias branch (Fig. 4.2 (a)). Fluence dependent variations of leakage current (values measured at U_R=100V and U_R=200V) are presented in Fig. 4.2 (b). An increase of leakage current implies a reduction of carrier

generation/recombination lifetime (Fig. 4.2 (b)) as it is reciprocally proportional to the leakage current ($\tau_g \sim 1/I_L$) [A13, 7]. This results in the consequent enhancement of recombination current at forward bias and the earlier saturation of the forward current as can be observed in Fig. 4.2 (a). At irradiation fluence $\Phi=10^{16}$ cm^{-2} the I-V characteristic becomes symmetric. The observed decrease of the forward current in the heavily irradiated diodes hints to the reduction of the injection capability of the junction.

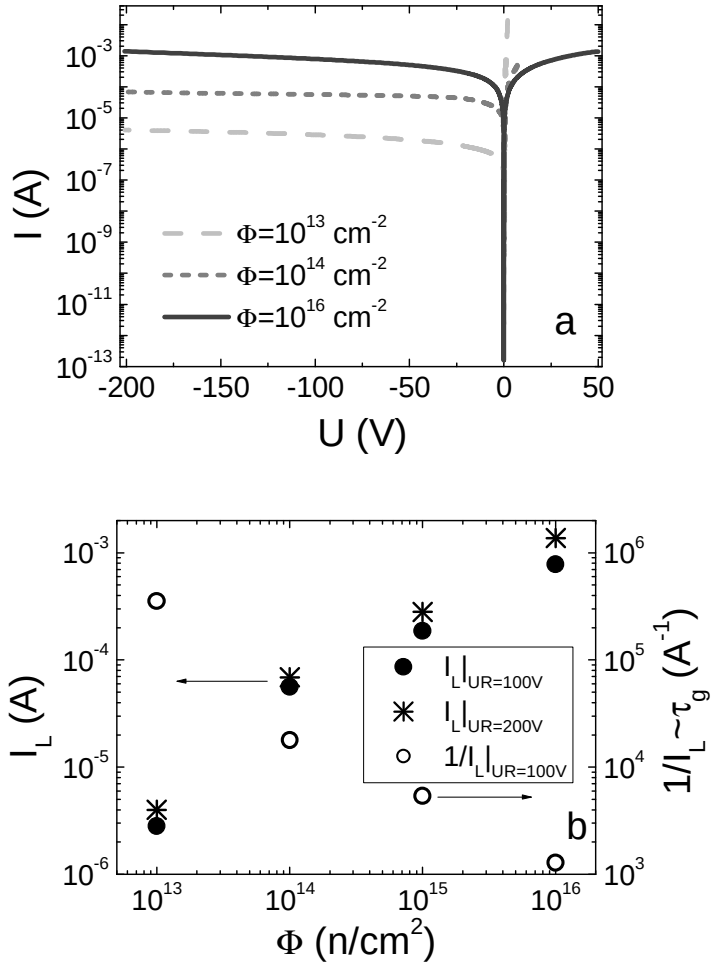

Fig. 4.2. a- Fluence dependent I-V characteristics measured in neutron irradiated MCZ Si diodes at room temperature (T=300 K); b- Leakage current variations in neutron irradiated diodes obtained from a reverse voltage branch of I-V characteristics at U_R=100V and U_R=200V compared with reciprocal leakage current $1/I_L \sim \tau_g$.

The C-V characteristics, measured at room and at low (T=120 K) temperatures and using both the parallel (C_P) and serial (C_S) circuit regimes at

100 kHz test signal frequency by a QuadTech-7600B LRC-meter, are illustrated in Fig. 4.3.

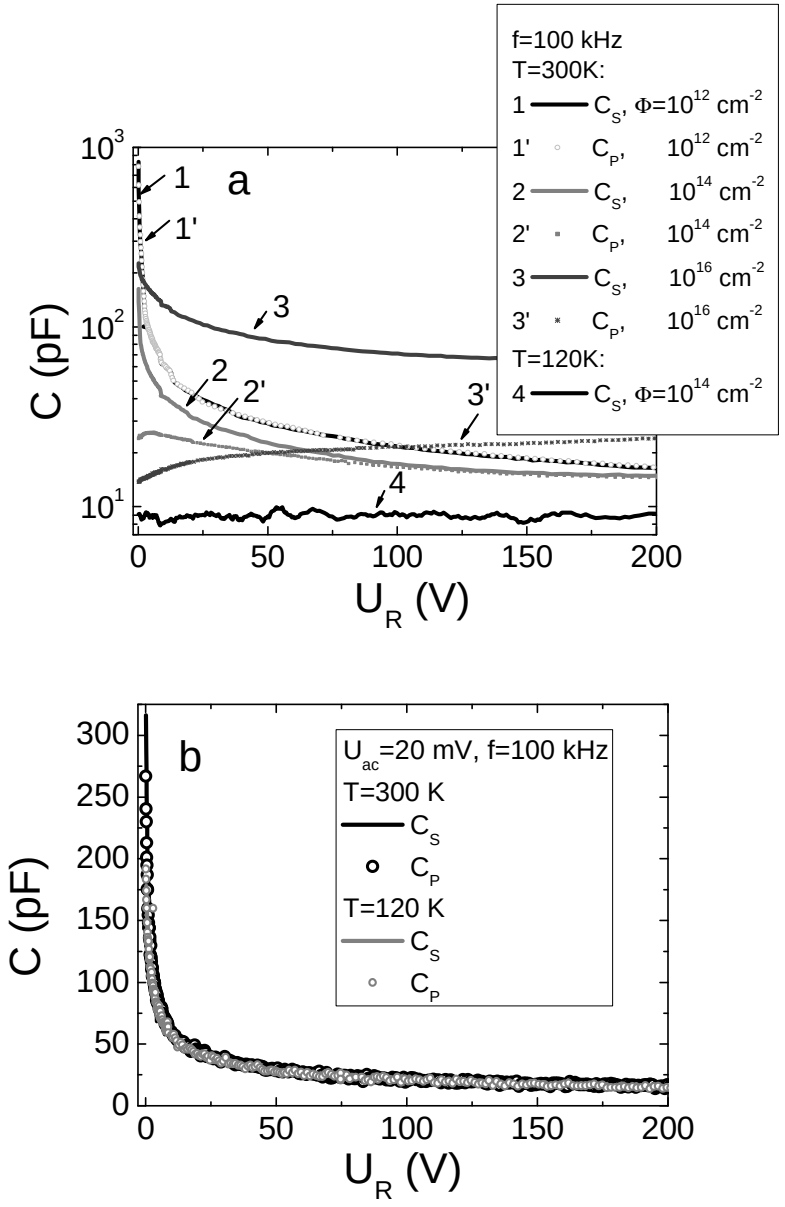

Fig. 4.3. a- Fluence dependent C-V characteristics measured in neutron irradiated MCZ Si diodes at room temperature (T=300 K) and compared with the one measured at low temperature (T=120 K) in neutron irradiated at a fluence of 10^{14} n/cm^2 MCZ Si diode. b- C-V characteristics measured in non-irradiated MCZ Si diode at room (T=300 K) and at low (T=120 K) temperatures in serial and parallel regimes.

The ac test signal was kept as small as possible, ≤ 20 mV. The parallel (C_P) and serial (C_S) circuit regimes have been used to control the requirement of low parallel conductance and of low series resistance, as discussed in [44], for correct C measurements. It is clearly observed that the C_P and C_S

dependencies on reverse voltage as well as the values of C_P, C_S coincide for samples irradiated with $\Phi \leq 10^{13}$ n/cm^2 (Fig. 4.3 (a)) and the absolute value of C_S decreases with increasing fluence. However, significant differences between C_P and C_S appear in heavier ($\Phi > 10^{13}$ n/cm^2) irradiated diodes. This result is in a quantitative agreement with published data on irradiated Si detectors [38], taking into account the differences in frequency. The differences between C_P and C_S indicate that the standard analysis for the extraction of C values is no longer valid for the diodes irradiated with $\Phi > 10^{13}$ n/cm^2. The main reason is the generation current and a non-linear voltage sharing between circuit elements within the LRC-meter due to the diode under test. The capacitance at low temperatures (120 K) appears to be independent of voltage for moderately irradiated ($\Phi \sim 10^{14}$ n/cm^2) diodes (Fig. 4.3 (a)) with its value equal to the geometrical one C_{geom}=10-15 pF. This result indicates that the diode is fully depleted starting from the lowest dc reverse voltages when carrier generation centres (via an enhancement of the thermal emission lifetime) are suppressed by a temperature decrease, in diodes irradiated with $\Phi > 10^{13}$ n/cm^2. However, the capacitance in non-irradiated diode at room and at low temperatures measured in C_P and C_S regimes coincide and satisfies the relation $C \sim U^{-1/2}$ (Fig. 4.3 (b)).

The measurements of C-V characteristics by employing a LRC meter can not further be applied for the characterization of heavily irradiated diodes. So, other techniques capable to resolve carrier capture, generation and recombination parameters should be used for characterization of the heavily irradiated diodes.

4.3. Evaluation of barrier parameters by BELIV technique

4.3.1. Fluence dependent BELIV characteristics

Variations of current transients measured by applying the linearly increasing voltage pulse (BELIV) at reverse and forward biasing in neutron irradiated detectors are presented in Figs. 4.4 (a) and (b), respectively. These

characteristics show clear dependence on neutron irradiation fluence. The BELIV characteristics are modified by radiation induced carrier capture and generation centres.

Generation centres can be observed within BELIV transients either due to depletion width modification (changing the electric field distribution) or by collected charge when depletion width is increased with LIV pulse. The modification of depletion width, accompanied with electric field redistribution, appears due to temporal variation of effective doping

$$N_{Deff}(t) = N_D\left[1-\frac{\left(N_{an}\pm\left(N_d^{\pm}-n_d(t)\right)\right)}{N_D}\right] \tag{4.1}$$

Here, N_D is doping density of non-irradiated material, N_{an} – density of radiation induced acceptors in n-type material within the lower half of the bandgap, $N_d^{\pm}$ – density of donor (+) or acceptor (-) type traps within upper half of the bandgap with their temporal filling $n_d(t)$. Temporal variation of $N_{Deff}(t)$ results in temporal variation of barrier capacitance as

$$\begin{aligned} C(t) &= C_{b0}\sqrt{1-\frac{\left(N_{an}\pm\left(N_d^{\pm}-n_d(t)\right)\right)}{N_D}}\times \\ &\times\left[1+\frac{1}{U_{bi0}}\left(U(t)+\frac{k_BT}{q_e}\ln\left(1-\frac{N_{an}\pm\left(N_d^{\pm}-n_d(t)\right)}{N_D}\right)\right)\right]^{-\frac{1}{2}}. \end{aligned} \tag{4.2}$$

Here, C_{b0} is expressed by the parameters of the non-irradiated diode. Then, the BELIV current can be derived as a time differentiated response

$$i(t) = \frac{dU_C}{dt}\times\left(C(t)+U_C(t)\left[\frac{dC}{dw_d}\frac{dw_d}{dU_C}+\frac{dC}{dw_d}\frac{dw_d}{dn_d}\frac{dn_d}{dU_C}\right]\right). \tag{4.3}$$

It is important to note that this regime is probable when single type fast traps dominate. In this regime measured transients in traps free and containing traps material coincide at the initial instants. For the charge collection regime, the generation current component is determined by carriers that are collected from the depleted bulk during evolution of LIV pulse and expressed as $i_g(t)=q_e n_i S w_0(1+U_C(t)/U_{bi})^{1/2}/\tau_g$. This component can increase the current starting from the very beginning of the BELIV transient.

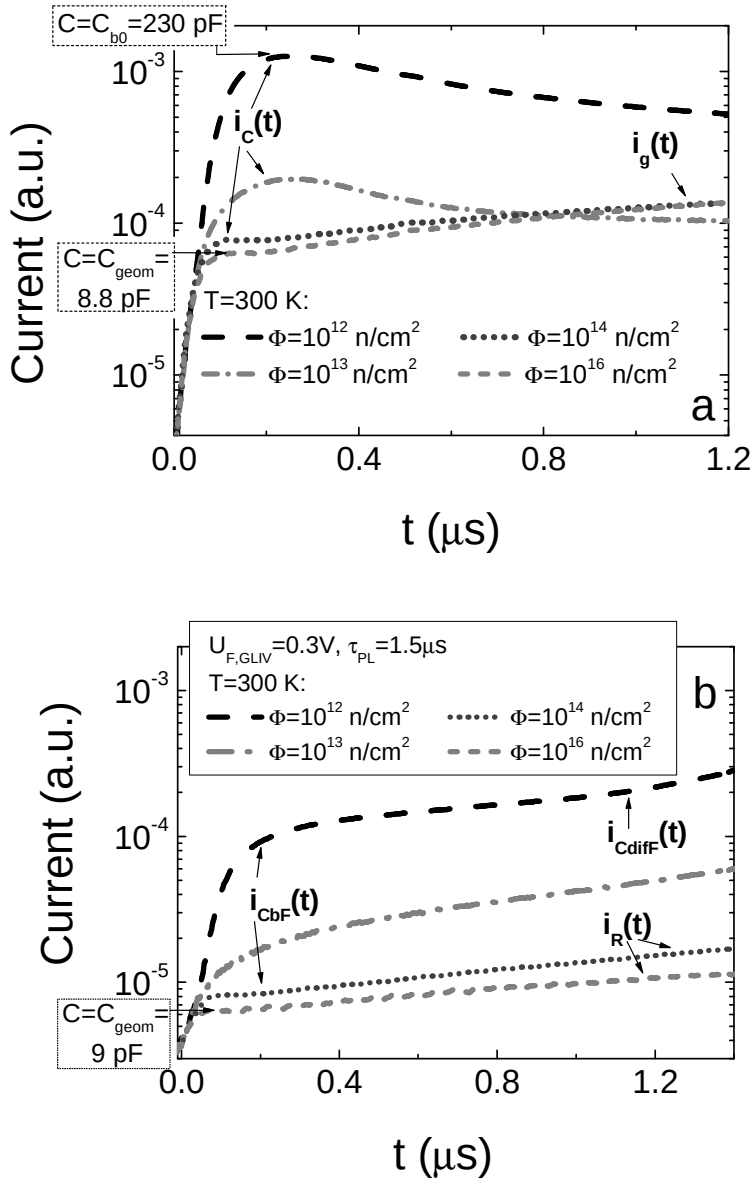

Fig. 4.4. Variations of barrier (a) and diffusion (b) capacitance charging currents dependent on irradiation fluence in Si *pin* detectors at reverse and forward biasing, respectively.

The charge extraction and generation current components can be determined from the fluence dependent experimental BELIV transients for reverse LIV pulses (Fig. 4.4 (a)). The reverse biased BELIV transient contains an initial peak ascribed to the equilibrium barrier capacitance C_{b0}, followed by a descending component of the charge extraction capacitance and an increasing component attributed to the generation current. The generation current component becomes dominant for higher voltages ($U_R \geq 0.7$ V, corresponding to $t > 200$ ns for a single transient) within transients measured on reverse LIV

pulsed diodes irradiated with $\Phi > 10^{13}$ n/cm^2, as illustrated in Fig. 4.4 (a). The fluence range for the dominance of the generation current is in agreement with that obtained when a separation between C_P and C_S characteristics appears in the C-V characteristics (Fig. 4.3 (a)). Thus, the evolution of the BELIV transients (Fig. 4.4 (a)) shows a monotonic increase of the generation current with increasing Φ which is corroborated by the reverse bias I-V characteristics (Fig. 4.2). The range of the dominance of generation current in BELIV and I-V characteristics corresponds well to the region of the "inversion sign" of effective doping [35, 36]. The dominance of the generation current hides/disturbs the current phase shift measurements (the increased current due to generation of carriers in the space charge region leads to the seeming phase shift) by the LRC technique, due to which erroneous values of U_{FD} and N_{Deff} are extracted. The dominance of generation current within BELIV transients indicates fast capture of carriers by high density of radiation induced traps (before emission). The decrease of the effective density of free carriers, caused by fast carrier capture, leads to an increase of a serial resistance (in the electrically neutral material) and to the reduction of the current for the forward voltage branch (Fig. 4.2 (a)).

The barrier and storage capacitance currents dominate within forward biased BELIV transients (Fig. 4.4 (b)), in the diodes irradiated with the smallest fluences of $\Phi < 10^{13}$ n/cm^2. The barrier capacitance, revealed by the initial amplitude for both the reverse and forward biased diode BELIV transients (Figs. 4.4 (a) and 4.4 (b), respectively), decreases with increasing fluence. For perfect diodes, the storage capacitance dominates in the ulterior stages of the BELIV transient. This is in agreement with measurements on the lowest fluence $\Phi \sim 10^{12}$ n/cm^2 irradiated diodes. For the storage capacitance induced current component, a fast current increase with time is observed. However, this storage capacitance component decreases with increasing fluence and it fully disappears for $\Phi > 10^{13}$ n/cm^2. It is out-rivalled by the recombination current component, which shows a nearly linear increase with

LIV voltage (for $\Phi > 10^{13}$ n/cm^2). This result shows, that even for the moderately irradiated diodes, the forward voltage does not govern the junction and the carrier injection. This can happen, if the diode is completely depleted at equilibrium. Then the diode behaves like a capacitor, where the initial BELIV step represents the geometrical capacitance for $\Phi > 10^{13}$ n/cm^2.

Thus, the observed fluence dependent variations (Fig. 4.4 (b)) of the forward biased BELIV transients, for $\Phi > 10^{13}$ n/cm^2, are in agreement with changes in the I-V characteristics for the forward voltage (FV) branch (Fig. 4.2 (a)): the decrease of the forward current relative to its values in the less irradiated diodes and the possibility to apply a relatively large forward voltage on heavily irradiated diodes indicate the full depletion conditions. Built-in full depletion can be reached when radiation defects compensate completely the dopants. In that case nearly all "native" doping induced free carriers are captured by the large density of radiation induced traps, while only a small fraction of these traps are filled due to lack of free carriers. The routine interpretation of C-V measurements is incorrect in such a situation, as the ac voltage only mediates the recombination–generation current variations, especially if ac signal amplitude $u > k_B T/q_e$. The dielectric relaxation time for fully compensated material becomes very long.

The total BELIV current for the above described full depletion voltages can be calculated (similarly to the method used in [A14, 44]) by considering the conductivity and displacement current components over the sample thickness d for variable voltage and surface charge changes on electrodes using standard boundary conditions (for electric field $E|_{x=d} = 0$, $dE/dx|_{x=d} = 0$ and potential $V|_{x=d} = 0$). This solution is expressed as

$$i(t)_{FD} = q_e S \frac{d}{2}\left(\frac{dn}{dt} + \frac{dp}{dt}\right) + \frac{\varepsilon\varepsilon_0 S}{d}\frac{dU_C}{dt}. \qquad (4.4)$$

The solution (for over-depleted diode and nearly equal carrier transit τ_{tr} and thermal emission τ_{em} lifetimes, $\tau_{tr} \sim \tau_{em}$, as well as using relations $|dn/dt| = n_0/\tau_{em} \approx n_0/\tau_{tr}$, $n \approx n_0 = N_D$), can be approximated as

$$i(t)_{FD} \approx q_e S \frac{d}{2}\frac{n_0}{\tau_{tr}} + C_{geom}\frac{dU_C}{dt} = q_e \frac{S}{2d} n_0 \mu_n U_C(t) + C_{geom}\frac{dU_C(t)}{dt}. \qquad (4.5)$$

Hereby, it is assumed that the geometrical capacitance C_{geom} is given by $C_{geom}=\varepsilon_0\varepsilon S/d$, μ_n is mobility of electrons, $\tau_{em}=1/\sigma_c v_T N_C \exp(-E_d/k_B T)$, $\tau_{tr}\cong d^2/\mu_n U$. It is clear that for insulating material the BELIV transient takes the shape typical for a pure capacitor with a current value of $i_{CFD}=C_{geom}(dU_C/dt)$. The voltage drop on a load resistor (being a solution of current equation for RC circuit with LIV pulse) represents the square-wave pulse if C is constant. For compensated material full of traps, a further increase of the voltage above U_{FD} shows the current enhancement transient $i_{emFD}(t)=q_e(S/2d)n_0\mu_n U_C(t)$ which is added to i_{CFD}.

A similar situation appears in C-V characteristics for harmonic ac voltages of frequency f, capable of ensuring the necessarily short carrier transit time $\tau_{tr}\cong d^2/\mu_n U < \tau_{em}\cong f^{-1}$. The emission time τ_{em} for trapped (n_T) carriers depends on the capture cross-section σ_c and thermal velocity v_T and on the effective density of band states N_C as well as on the thermal activation energy E_d of the trap. Then, if the dc voltage is sufficient to collect all the trapped charge (of value close to equilibrium density n_0 of "native" carriers) within built-in fully depleted material, the measured C-V response saturates. This voltage seems to be wrongly ascribed to a full depletion state and to the space charge sign inversion effect in [35-39].

4.3.2. Temperature and bias illumination dependent BELIV transients

For the non-capsulated diode structures, trap determined modifications of the BELIV current transients of $i_C(t)$ can be suppressed through the priming of the trap filling by infra-red (IR) continuous wave illumination. Additionally, the initial component of BELIV current transient can be manipulated by a pedestal of varied polarity of the dc voltage primaring together with a LIV pulse. Variations of the mentioned external factors can be combined with temperature variations to modify filling of the traps.

In Fig. 4.5 (a), variations of BELIV current transients (for reverse biased diode) measured with and without bias illumination (BI) are presented.

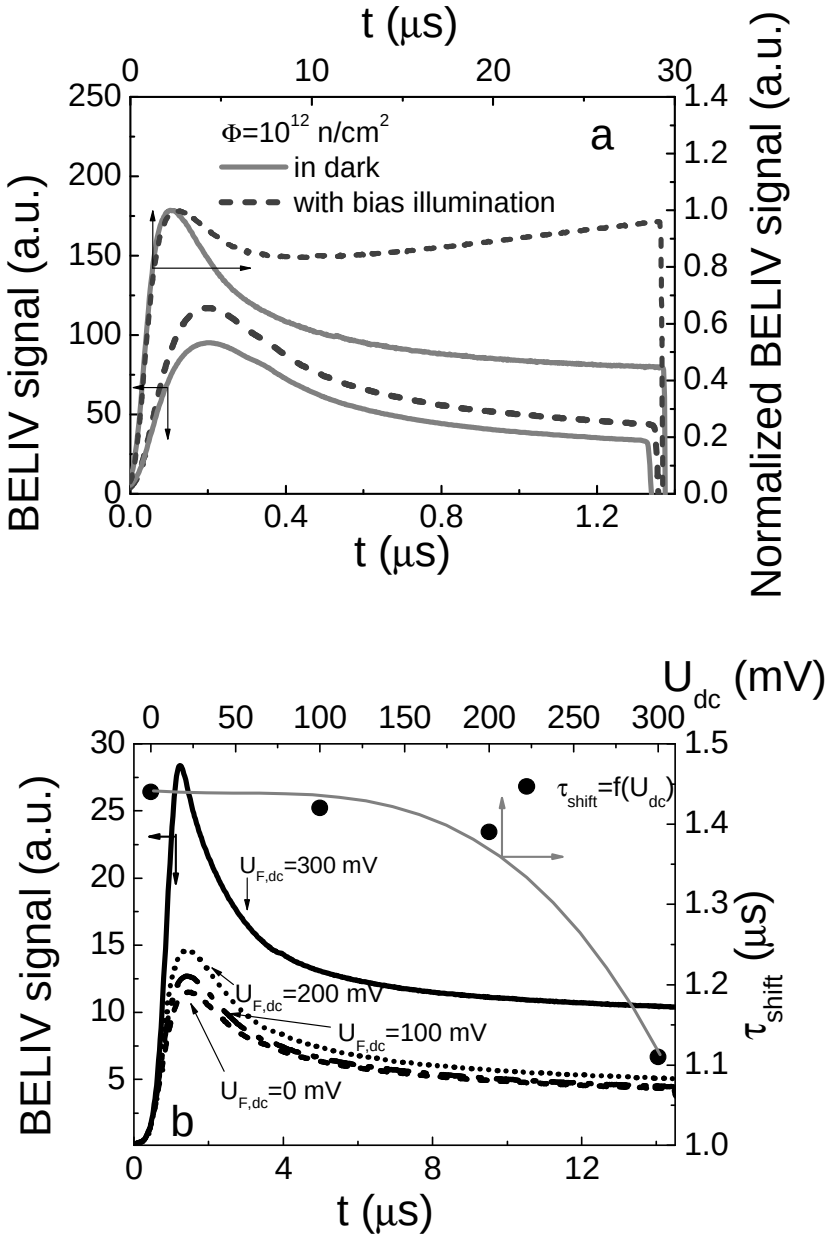

Fig. 4.5. a- Bias illumination (BI) dependent charge extraction current transients measured at τ_{PL}=1.4 μs and τ_{PL}=30 μs LIV pulse durations on the same irradiated diode. Transients measured at τ_{PL}=30 μs pulse duration are normalized to the peak amplitude. b- Variations of BELIV transients and a shift of the barrier capacitance charging current peak position within transients recorded in Φ=10^{12} cm^{-2} neutron irradiated diode for reverse biased LIV dependent on forward dc voltage bias ($U_{F,dc}$) pedestal.

The primary steady-state illumination modifies the initial filling of traps for electrons and holes. Depending on duration of LIV pulses and on density of

traps, the time scale of carrier generation processes can be highlighted, as illustrated in Fig. 4.5 (a). The absolute value of the initial amplitude of BELIV current transient for a reverse biased diode increases proportionally to the intensity of the bias illumination. Simultaneously, a component of generation current within ulterior stages of transient is increased with BI. Increment of generation current is more obvious for the normalized (to the amplitude of the initial step) transients, shown in Fig. 4.5 (a). This result clearly proves that generation current is caused by several traps characterized by a wide spectrum of levels within the upper half of band-gap, as discussed in chapter 4.3.1. For rather long LIV pulse, duration of which corresponds to the thermal emission time scale (characteristic for a definite sample), the generation current becomes dominant within the rearward component of a transient. BELIV current transients for reverse bias LIV pulses can be manipulated by the external light only in diodes irradiated by rather moderate fluences, $\leq 10^{13}$ n/cm^2, at room temperature.

Complementarily, filling of the minority carrier trap can be implemented by dc forward voltage pedestal $U_{F,dc}$ combined with BELIV current transient measurements using the reverse biased LIV pulses. Injection of minority carriers enables one to eliminate minority carrier traps (those seems to be efficient as the compensation centres within a lower half of band-gap), and to regenerate barrier capacitance, as shown in Fig. 4.5 (b). Enhancement of a forward dc voltage pedestal leads to filling of these traps. This determines an increase of the BELIV current signal amplitude and a shift of the peak to the initial time instants within a transient. However, a suppression of compensating centres at room temperature has been reached only for moderately irradiated ($\leq 10^{14}$ n/cm^2) diodes.

An impact of radiation induced generation centres can be also suppressed by reduction of temperature, as carrier emission lifetime increases about exponentially with reduction of temperature. The temperature dependent BELIV current transients are illustrated in Fig. 4.6 (a) for heavily irradiated (10^{14} and 10^{16} cm^{-2}) and reverse biased *pin* diodes. It is clearly seen that the

component of the carrier generation current decreases with reduction of temperature. Then BELIV current transient approaches to that inherent for dielectric capacitor, at 172 K. Thus, heavily irradiated diode is fully depleted at equilibrium, although at room temperature this capacitor-inherent characteristic is masked by the large generation current component.

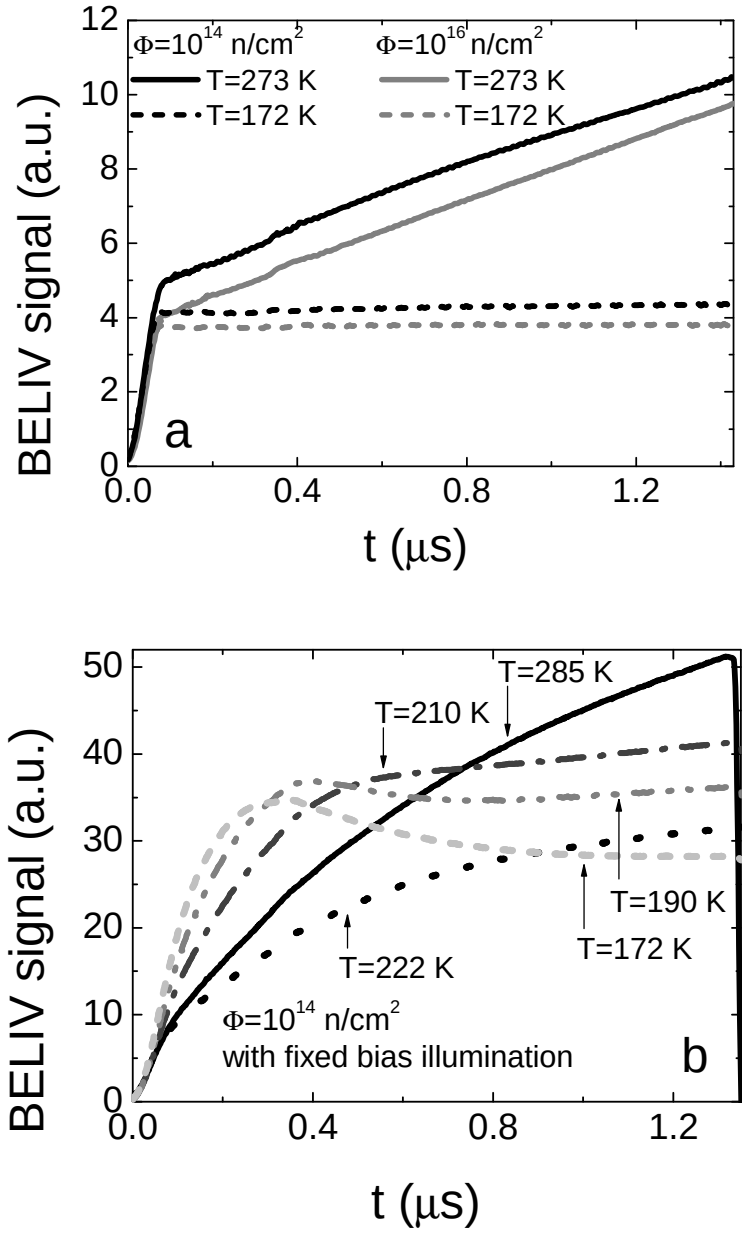

Fig. 4.6. a- Temperature dependent variations of BELIV current transients in heavily (10^{14} and 10^{16} n/cm^2) irradiated Si *pin* diodes. b- Temperature and bias illumination dependent variations of the BELIV current transients.

With reduction of temperature, which leads to a consequent increment of carrier emission time and to a decrease of density of the empty capture-emission centres, the steady-state bias illumination becomes sufficient for suppression of the carrier capture centres. It can be seen in Fig. 4.6 (b), the barrier capacitance in moderately irradiated ($\leq 10^{14}$ n/cm^2) diodes restores to values inherent for lightly irradiated diodes when a combined conditioning made by the temperature lowering and additional illumination is applied. However, neither steady-state biasing by dc forward voltage nor continuous wave illumination is sufficient to suppress charge compensation and carrier capture/generation centres in heavily irradiated ($> 10^{15}$ n/cm^2) diodes.

4.3.3. Evaluation of barrier and generation current parameters

Analysis of different aspects in the measured BELIV transient changes, shown in Figs. 4.4, 4.5, 4.6, provide qualitative information about the fluence and temperature dependent variations of the junction parameters and their possible modifications by external conditioning (dc voltage/IR illumination priming and temperature). To extract the barrier parameters more precisely, fitting of the measured transients by simulated ones is inevitable. There are several approaches in implementation of fitting procedures dependent on the observed initial delays relatively to LIV pulse, on the regularity of LIV pulses, on the values of applied LIV voltages, on the values of barrier capacitance (area of junction) and on the prevailing processes within junction (impact of space charge generation current, of rapid carrier capture/emission by fast deep centres in the upper half of band-gap, etc.). It is also necessary to discuss the impact of nonlinear voltage sharing within nonlinear RC circuit elements of load resistor R_L for registration of the BELIV current transients and diode with barrier capacitance C_{b0}.

The solution of a simple differential equation $R_L di/dt+(1/C)i=A$, derived for the linear elements, as a capacitor C and a resistor $R_L=R$ connected in serial, and for a LIV pulse $U=At$, when using an initial condition of $i(t=0)=0$, leads to the expressions:

$$i(t) = AC(1-e^{-\frac{t}{RC}}),$$

$$U_R(t) = ACR(1-e^{-\frac{t}{RC}}) = \begin{cases} At\,|_{t<<RC} \\ ACR\,|_{t>>RC} \end{cases}, \tag{4.6}$$

$$U_C(t) = A[t - RC(1-e^{-\frac{t}{RC}})] = \begin{cases} A\frac{t^2}{2RC}\,|_{t<<RC} \\ A(t-RC) \cong At\,|_{t>>RC} \end{cases}.$$

Equations (4.6) imply that the linear voltage drop on a capacitor (and on a diode under test - DUT) appears for time instants $t>>RC$. The maximal barrier capacitance C_{b0} for DUT is obtained during the initial instants of LIV pulse (when $At<U_{bi}$). Thus, the fastest initial component of the BELIV current transient is determined by the transition time constant RC_{b0}. The linear RC_{b0} modifications (for instance, a shift) of the initial current step $i_C(t\approx 0)$ in equation (3.26) can be roughly emulated by a convolution integral (3.27). A kink (at $t\approx RC$) within the initial rise front of the simulated BELIV transient and a peak position of the experimental one might be employed for the evaluation of the C_{b0} using rough linear approximation (by a convolution integral) of a BELIV transient.

However, variation of the voltage drop $U_C(t)=A(t\text{-}RC(t))$ on a nonlinear DUT can be assumed being a linear function of t only in time scale $t>2RC$ (Eq. (4.6)). For the precise description of BELIV transient, a generalized non-linear differential equation

$$\frac{dU_C(t)}{dt}\frac{(1+\frac{U_C(t)}{2U_{bi}})}{(1+\frac{U_C(t)}{U_{bi}})^{3/2}} - \frac{U_p(t) - U_C(t)}{RC_{b0}} = 0 \tag{4.7}$$

with the initial conditions $U_p(t=0)=0$ and $U_C(t=0)=0$ should be solved to determine $U_C(t)$. This equation (Eq. 4.7) is derived assuming the time-dependent voltage drops on DUT, as $U_C(t) = U_p(t)\text{-}U_R(t)$. Only the numerical solutions of the Eq. (4.7) can be obtained. Using a solution $U_C^*(t)$ of equation (4.7), a voltage drop on the load resistor, as $U_R^*(t) = U_p(t)\text{-}\ U_C^*(t)$, represents the simulated BELIV transient. Thus, a fitting procedure, of the numerically

simulated BELIV transients $U_R^*(t)$ to the experimental ones, is inevitable and should be employed for precise extraction of the junction parameters.

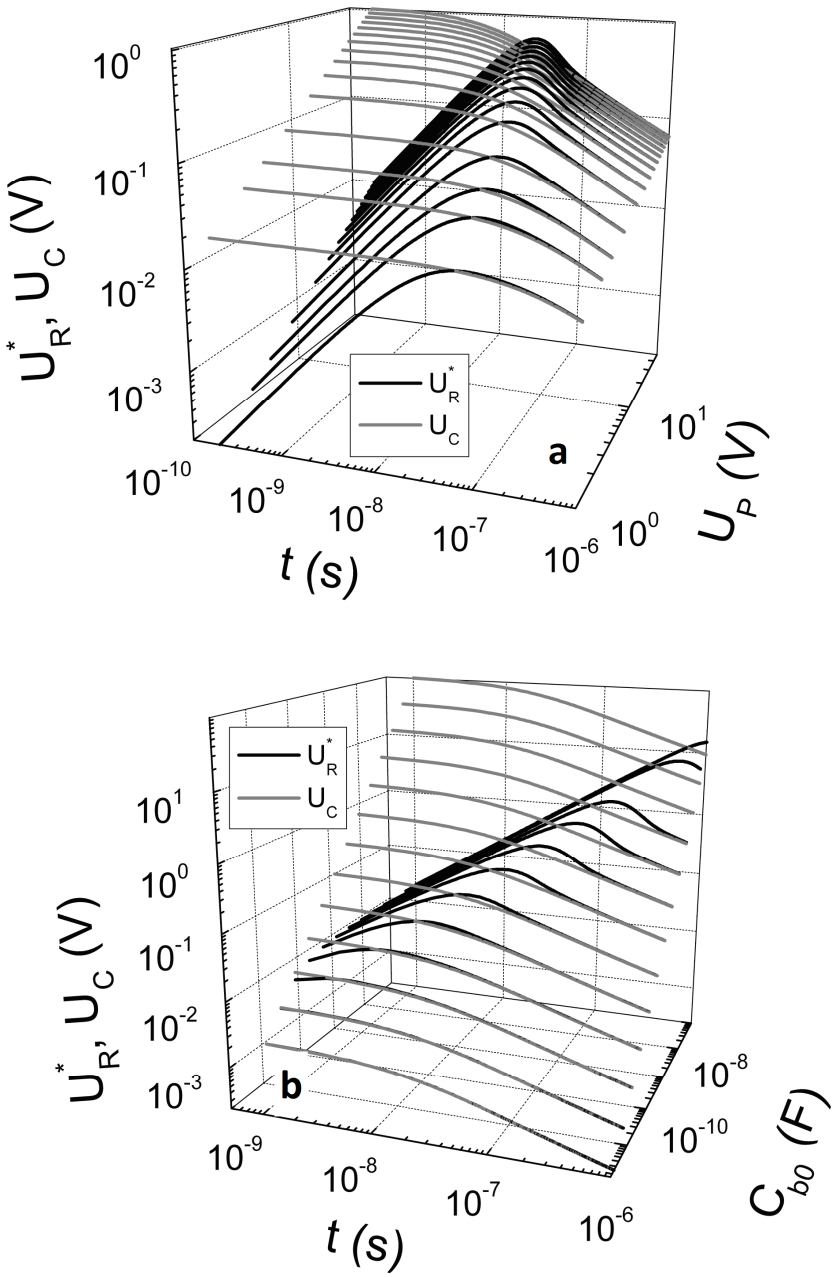

Fig. 4.7. a- Numerically simulated BELIV voltage transients $U_R^*(t)$ as a function of a LIV pulse peak voltage U_P compared with those simulated by analytical approximation (U_C). b- Numerically simulated BELIV voltage transients $U_R^*(t)$ as a function of initial barrier capacitance values C_{b0} compared with those simulated by analytical approximation (U_C).

Comparison of the simulated voltage transients (using $U_R^*(t)$ obtained by solution of Eq. (4.7), and using $U_C(t)$ (Eq. (4.6)) values evaluated for fixed

C using analytical approximations (Eqs. (3.26) and (3.27), for *RC*=20 ns) are presented as a function of LIV pulse peak voltage U_P and as a function of value of the equilibrium barrier capacitance C_{b0} in Figs. 4.7 (a) and (b), respectively. It can be noticed that a deviation from the analytically simulated curves appears in the range of the BELIV voltage peak. This deviation increases with increment of U_P and of C_{b0} values. These deviations can be explained by the relative enhancement of barrier charging current through the load resistor. This current increase modifies non-linearly the voltage drops (as included in Eq. (4.7)) on a load resistor and on a diode. Thus, the analytical approximation (Eqs. (3.26, 3.27 and 4.3)) can be exploited for primary analysis of the BELIV transients only in the range of small i_C currents, including *RC* shift.

A sketch of fitting procedure applied on BELIV transients measured at 295 K temperature on a diode irradiated with 10^{13} cm^{-2} neutron fluence is presented in Fig. 4.8. The impact of traps on space charge generation and diffusion currents is estimated from the primary qualitative analysis. In order to have a closed system of equations, the set of LIV voltage varied BELIV transients (Fig. 4.8 (a)) are simultaneously fitted, keeping a fixed set of adjustable parameters (N_D, τ_g and $i_{diff\infty}$). The fitting procedure is finished when the best fit of required precision (controlled by the non-linear least square (NLS) algorithm) is obtained for all the included (in Fig. 4.8 (a)) transients, and values of N_D, τ_g and $i_{diff\infty}$ are simultaneously extracted.

The input of the required set of independent equations (transients) and parameters in the optimization of fitting task is determined by the primary step of fitting. This procedure is illustrated in Fig. 4.8 (b). There a possibility to fit the experimental transient with minimal current components and their parameters is analyzed. In the discussed fitting procedure, the barrier charging current, the generation current and the diffusion current components (shown by the broken curves in Fig. 4.8 (b)) should be involved. It is assumed that parameters, as U_{bi}, C_{b0}, w_0 are defined by an adjustable value of N_D for $i_C(t)$ simulations using Eq. 3.27. There, a simple solution of a linear RC-circuit for a

LIV pulse, leading to a time-dependent voltage drop on a barrier under test, expressed as $U_C(t)=A[t-RC(1-\exp(-t/RC)]$, is used. N_D, τ_g and $i_{diff\infty}$ values.

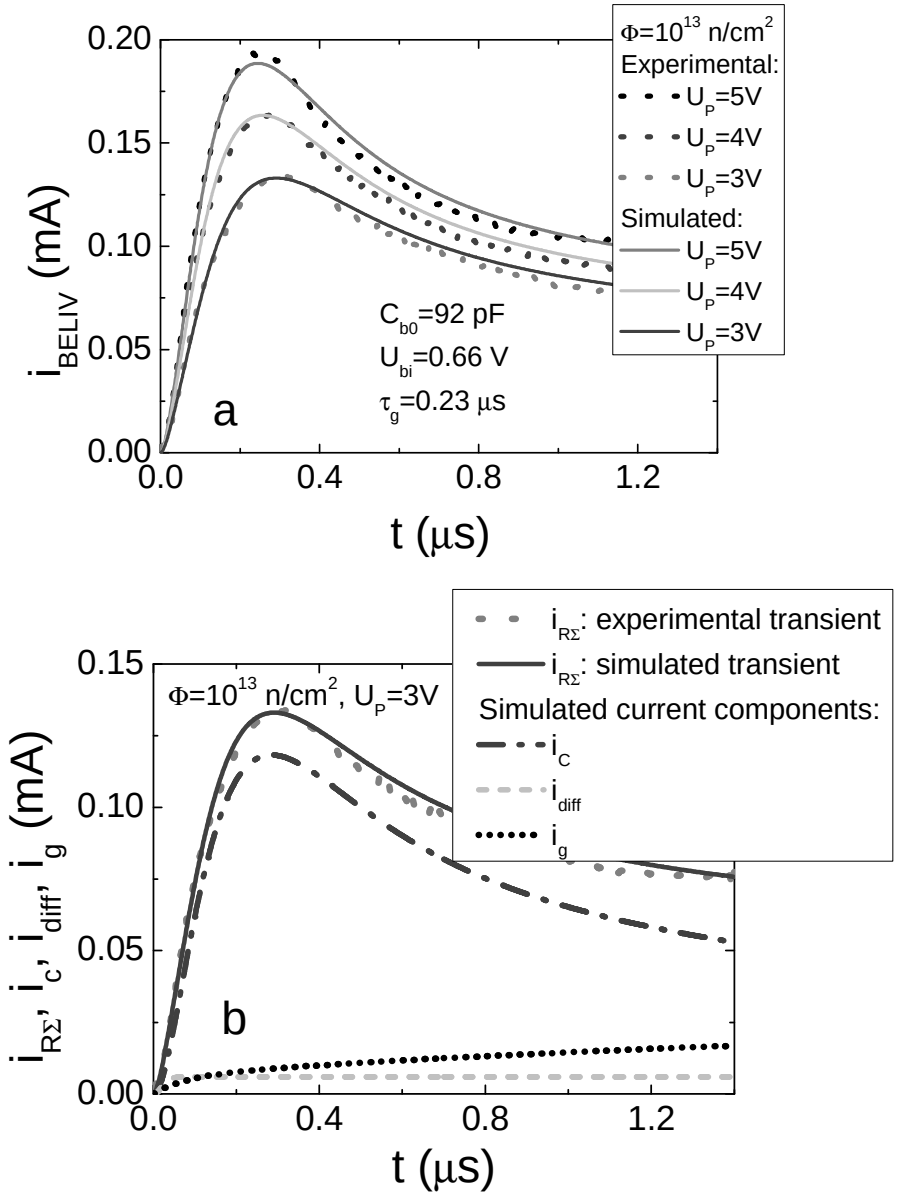

Fig. 4.8. a- A set of barrier capacitance charging current transients (dots), measured by the BELIV technique at different (3, 4 and 5 V) LIV voltages on a Si diode irradiated with neutron fluence of 10^{13} cm^{-2}, simultaneously fitted by simulated (using Eqs. 3.26, 3.27) ones (lines), keeping a fixed set of adjustable parameters: N_D =1.05×10^{12} cm^{-3}, τ_g=0.23 μs and $i_{diff\infty}$= 6 μA. b- Comparison of the barrier capacitance charging current transient (dots) measured for a 3 V LIV pulse with the simulated total barrier current (solid line), composed of the barrier capacitance charging current (dash-dot), of the diffusion current (short-dash) and of the generation (short-dot) current.

It is worth noting, that for a pure capacitor and for time instants $t>>RC$ (after the initial rising), a voltage on a load resistor

$U_R(t)=ACR[1-\exp(-t/RC)]|_{t>>RC}\cong ARC$ is invariable, due to the exact compensation of voltage changes on capacitor and on resistor (at every time instant). Thus, for a LIV pulse $U_p(t)=At$, the RC circuit with linear elements of R and C exhibits a step-like transient shape with a flat vertex. This can be an indication (Fig. 4.6 (a)) for degradation of a barrier of diode, when material of a diode base mutates from the semiconducting state to an insulating one, due to heavy irradiation. The parameter RC is defined by the characteristics of the load resistor and of the diode under test. Then, the transient for the fixed LIV pulse is simulated to fit the experimental transient of the total current shown in Fig. 4.8 (b) and to get the primary set of

The extracted set of parameters reveals a reduction of N_D to 1.05×10^{12} cm^{-3} (compared to the value for a non-irradiated diode, N_D $=2.3\times10^{12}$ cm^{-3}), an increase of generation (with τ_g=0.23 μs) and of diffusion ($i_{diff\infty}$=6 μA) currents, after neutron irradiation with a fluence of 10^{13} cm^{-2}. This fitting approach works even better for diodes irradiated with lower fluences, whereby larger values of N_D are obtained.

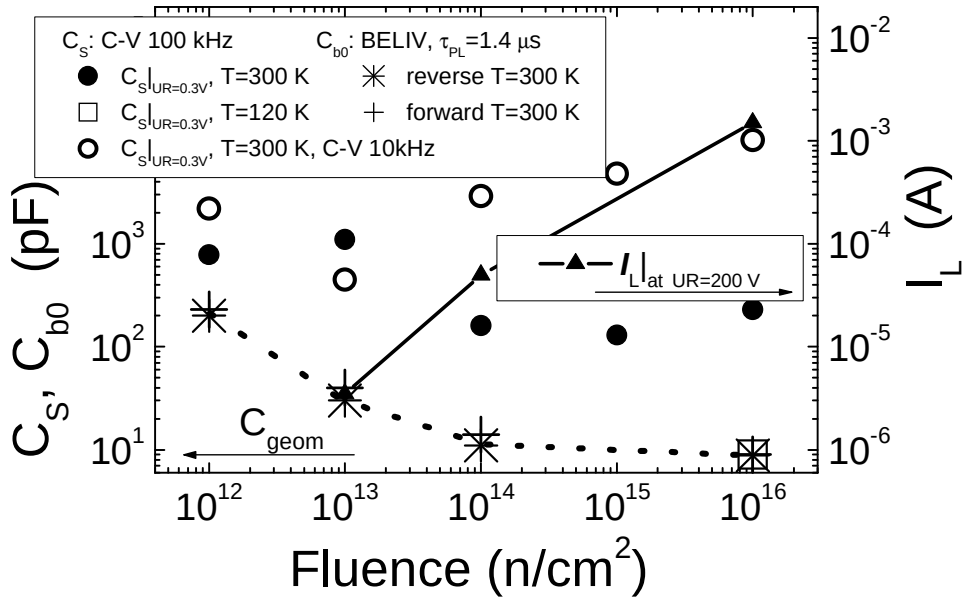

Fig. 4.9. Comparison of the fluence dependent variation of serial capacitance C_S (circles) at reverse voltage of about 0.3 V measured using 10 kHz (open circles) as well as 100 kHz (solid circles) at 300 K and 120 K (open squares) temperatures, of the barrier capacitance C_{b0} measured by BELIV technique using both reverse (stars) and forward (crosses) LIV pulses (left scale) at T=300 K, and of leakage current (right scale) extracted from I-V characteristics at 200 V reverse voltage.

Variations of C_S extracted from C-V characteristics, of the leakage current for a 200 V biased diode measured by I-V characteristics, and of the initial barrier capacitance C_{b0} evaluated by both reverse and forward LIV pulses are generalized in Fig. 4.9.

It is obvious, that the barrier capacitance estimated by the BELIV technique approaches to the geometrical C_{geom} for fluences $\Phi > 10^{13}$ n/cm^2. These C_{b0} values are significantly smaller than C_S extracted from the C-V characteristics at $U_{R,C\text{-}V} \sim 0.3$ V values comparable to the BELIV regime for $t < 200$ ns. This result can be understood by the elevated generation currents and the significantly increased dielectric relaxation time in the C-V characteristics. The C_S values measured by C-V at small reverse voltage (Fig. 4.9) do not show any clear dependence on fluence and the measured values considerably depend on test signal frequency, while experimental errors are rather large. The initial barrier capacitance C_{b0} evaluated by both the reverse and forward BELIV pulses lies within the measurement errors that do not exceed the size of the symbols in Fig. 4.9. This result represents a clear indication of the decrease of absolute C_{b0} values due to the increase of depletion width.

Summary of the main results described in the chapter

[A11, A13, A14]

Analysis of the neutron irradiated Si detectors by combining C-V, I-V and BELIV techniques enabled us to clarify the conditions of the full depletion in heavily irradiated Si detectors. It has been shown that built-in full depletion (the insulating state) is inherent for 300 μm thick n-type Si diodes doped with 10^{12} cm^{-3} donors and irradiated with hadron fluences above 10^{13} cm^{-2}. In other words, high resistivity material irradiated with fluences $\Phi > 10^{13}$ n/cm^2, becomes an insulator, and common concepts (used in the analysis of device and of junction operation) such as depletion width, effective doping density should be used with care.

It has been shown that the barrier evaluation by the linearly increasing voltage (BELIV) method can be a useful extension of transient techniques for the separation of barrier charging and carrier capture/emission currents. The BELIV pulsed technique enables one to clarify a few significant aspects: to identify the charge extraction regime and to estimate the barrier capacitance, to clarify the competition between barrier and storage capacitance and the generation/recombination currents, and to clarify the full depletion state for heavily irradiated diodes.

Procedures for the precise extraction of the set of barrier and depletion layer parameters by using BELIV technique have been demonstrated.

It has been shown that radiation defects induced space charge sign inversion effects and fatally elevated voltages of full depletion are artefacts due to the application of the standard C-V measurements in the complicated case of transition from semiconductor to insulator, when carrier emission and capture currents approach values of the barrier charging currents.

V. Examination of evolution of the radiation defects during irradiation

5.1. Instrumentation and arrangements of the *in situ* experiments

The experimental arrangement for the remote measurements of the microwave probed photoconductivity (MW-PCT-E) and induced charge diode current (ICDC) signals is sketched in Fig. 5.1.

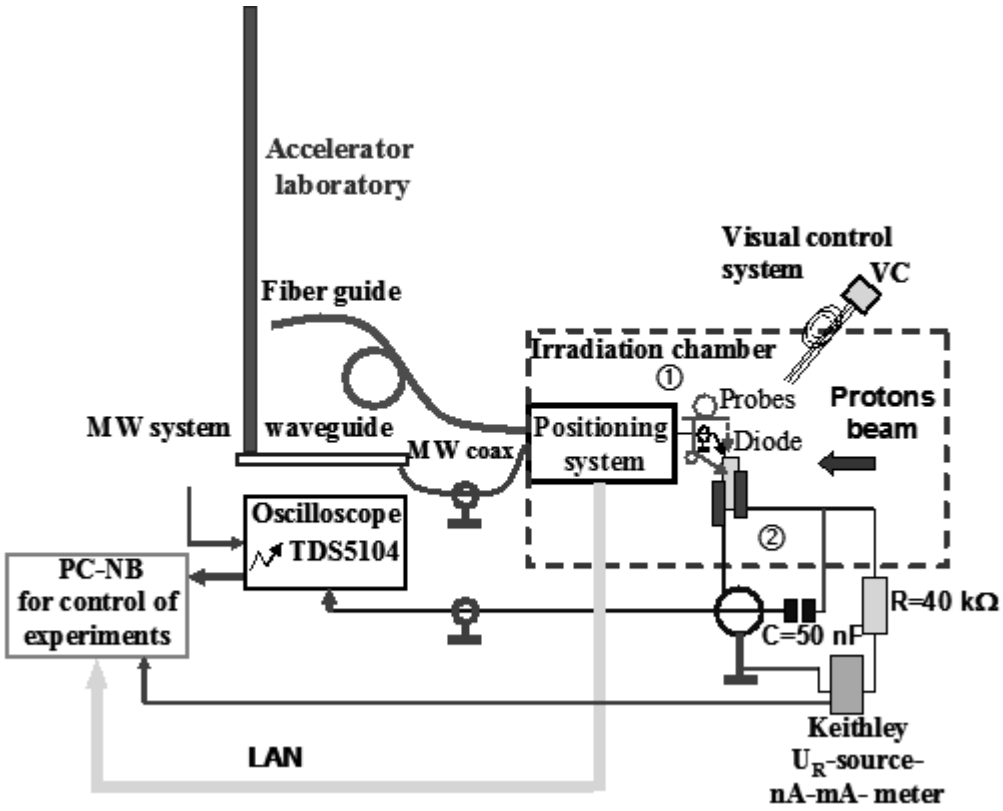

Fig. 5.1. Instrumentation for the remote control of carrier transport and recombination parameters.

The transient MW-PCT-E and ICDC signals are synchronously registered outside the accelerator control area on different channels of the 1 GHz Tektronix oscilloscope TDS-5104, using 50 Ω load resistors. A proton beam current has been kept rather small (of about 0.5 nA) to decrease noises within ICDC signals and to avoid excess carrier induced the impact ionization avalanche breakdown effect, inherent for the elevated proton fluxes [60]. Various regimes of the simultaneous measurements of the injected charge induced diode current (ICDC) and injected charge collection current (IChCC) transients have been employed.

A special sample holder was designed to enable proper electrodes for the electrical circuitry, containing windows for the proton beam and for optical excitation. A freshly cleaved cross-sectional boundary of a pad-detector broken into halves was used for perpendicular bulk excitation and MW-PCT-E probing by the coaxial needle-tip MW antenna using a 3D step-motor driven stage containing a flexible bellow.

For barrier capacitance charging current measurements, a *pin* diode was mounted on a sample holder (which was attached to the bottom of the irradiation chamber) and connected by the electrodes to an external measurement circuitry by a coaxial cable, as sketched in Fig. 5.2. Current transients have been registered using the 50 Ω load input of the DSO6102A oscilloscope. The measurement circuitry contains an adjusted output of a linearly increasing voltage generator (GLIV) and the diode under investigation, connected in series.

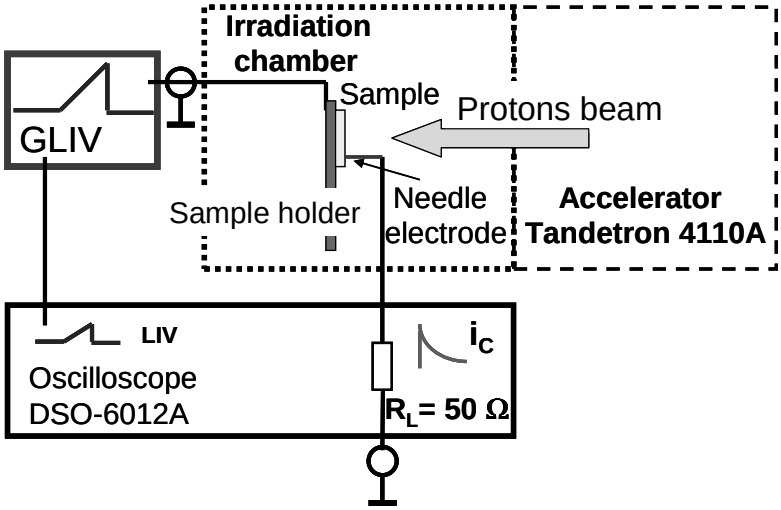

Fig. 5.2. Sketch of the experimental setup for the *in situ* measurements of the barrier capacitance charging current.

5.2. Evaluation of carrier transport and recombination parameters

In order to understand the nearly independent shape and duration of ICDC transients and to validate the procedures used to extract material parameters, the formation of the injected charge induced diode current (ICDC) transients have been examined. The double peak transients inherent for ICDC are observed in Fig. 5.3 (a). As discussed in chapter 3.3.3.1, a rather

"corrugated" electric field distribution appears for applied voltages $U_R \leq U_{FD}$. An enhancement of U_R above U_{FD} leads to an approximately uniform field distribution through the base of the *pin* diode, and the electric field is supported by planes of charge located at the external contact layers. The parallel plate condenser approximation can then be employed. At a fixed external voltage the electric field distribution within the considerably over-depleted base of the *pin* detector approaches a constant value, independent of depth within the base region. Operation of the diode with injected charge becomes similar to that of a capacitor in this case.

The smoothing of the field at $U_R > U_{FD}$ enables one to simplify evaluation of the mobility of excess carriers by using the well-known relation $\mu_e = d^2/\tau_{tr}U_R$ and drift time τ_{tr} measurements within the ICDC pulse. To evaluate changes of material during irradiation, measurements of carrier mobility at excess carrier densities $n_{ex} < n_0$, close to that values in dark are preferable, therefore the least possible excitation densities were maintained in our μ_e measurements. Commonly the drift time is evaluated as the time interval for the time of flight (TOF) pulse (at $U_R > U_{FD}$, when $\tau_{tr} < \tau_M$). In our case, however an initial delay appears within the risetime. This delay is caused by excess carrier temporal variations during laser pulse (τ_L) and by the measurement circuitry time constant $RC \approx 0.6$ ns. Actually, the risetime to peak τ_f should be taken as $\tau_f = 5RC$, to increase precision. A value of $\tau_f = 2.5$-3 ns is obtained in practice (Fig. 5.3 (a)). Therefore the more reliable way to extract τ_{tr} is from an estimation of the time interval between the ICDC peaks, which really indicate the steady state excess carrier generation and separation process. The extracted values of electron mobility $\mu_e = d^2/\tau_{tr}U_R \cong 1300$ cm^2/Vs (for a non-irradiated sample) validate the chosen interval for the drift time measurement. The ICDC current amplitudes slightly decrease with irradiation exposure time (due to capture of carriers on radiation induced traps), while drift time is nearly invariant, as shown in Fig. 5.3 (b). The mobility value variations $\Delta\mu/\mu < 20\%$, estimated from the dispersion of τ_{tr} values during

irradiation and illustrated in Fig. 5.3 (b), show the small impact of irradiation on the carrier scattering parameters. This is in qualitative agreement with results published in Refs. [41-43], while absolute values of μ_e obtained during irradiation appear to be lower than the value μ_e =1600-2000 cm^2/Vs evaluated after irradiation [41, 43] and μ_e =1000-1200 cm^2/Vs published in Ref. [42]. The explanation might be the different models exploited for extraction of μ_e values and the injected excess carrier domain width Δ.

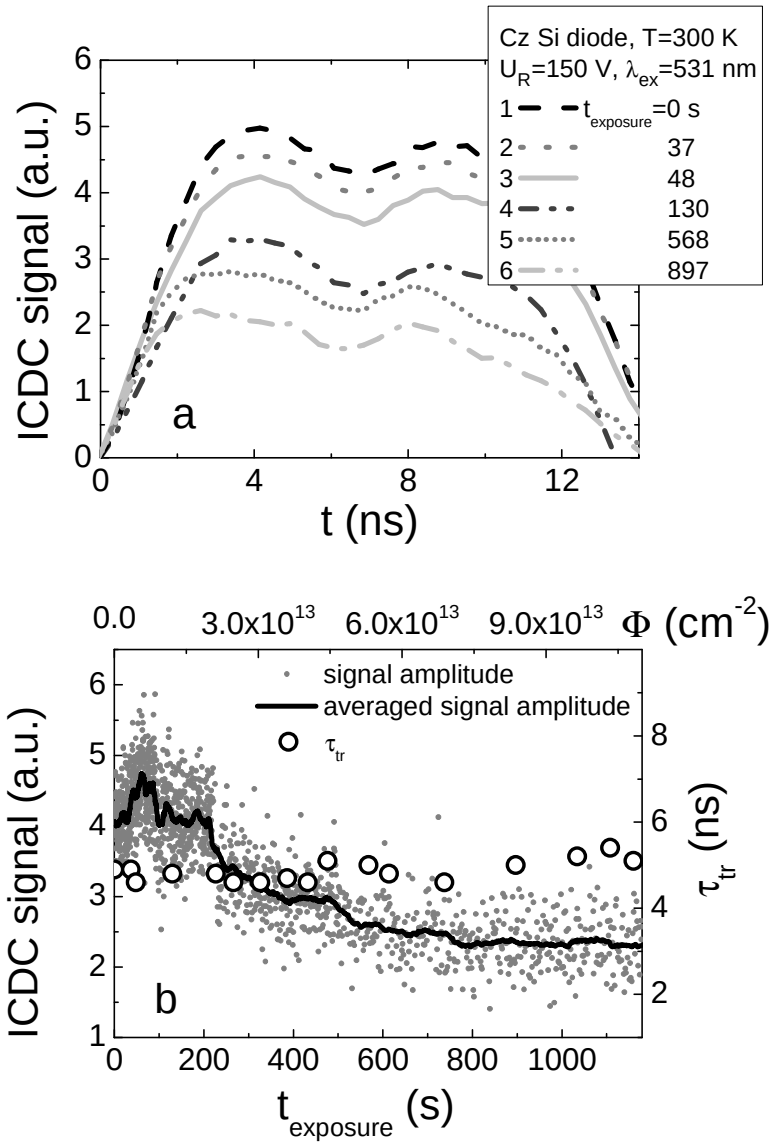

Fig. 5.3. Variations of the induced charge diode current (ICDC) transients (a) and of ICDC signal amplitude as well as excess carrier drift time (b) as a function of exposure time measured for 8 MeV protons using the surface excitation regime when carriers are generated in vicinity of the p^+n region of the diode structure (drift of electrons).

At a rather high excitation density, $q_e n_{ex} \Delta > CU_R$, and low applied voltage the IChC current transient acquires a rising peak pulse shape with very small amplitude at initial instants and effective lifetime at the IChCC pulse vertex evaluated as $\tau_S=(\tau_D^{-1}+\tau_R^{-1})^{-1}$ with carrier recombination (τ_R) and diffusion $\tau_D \cong d^2/4\pi^2 D_A$ times.

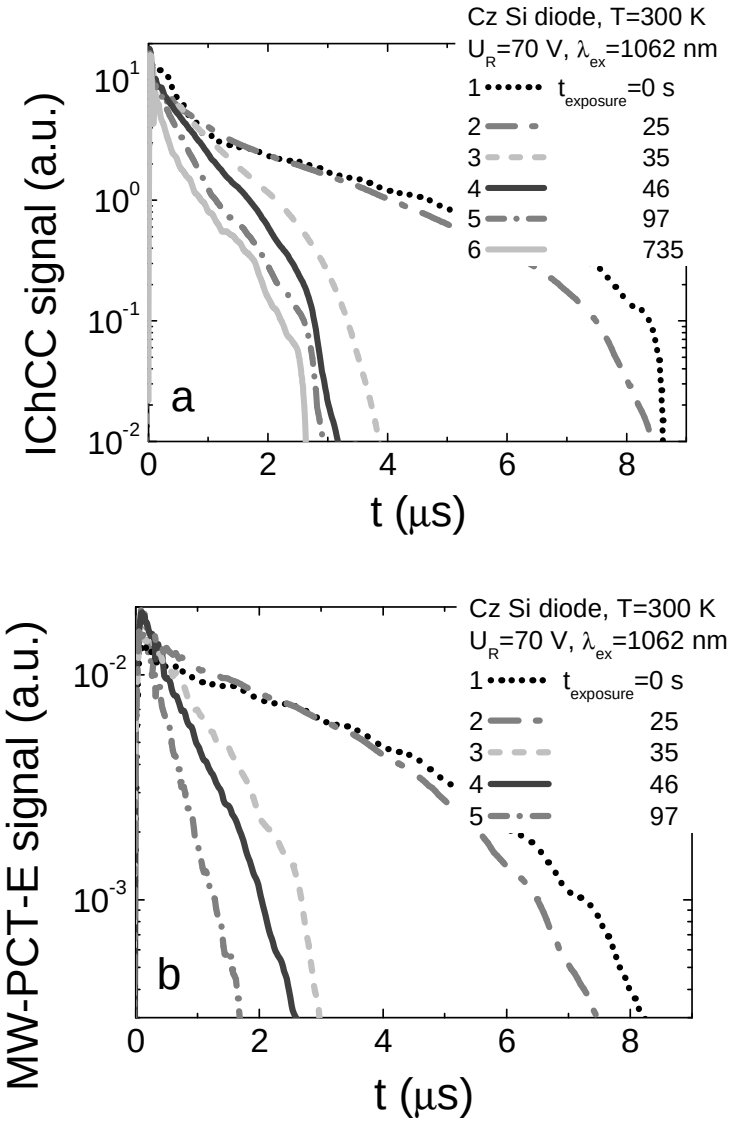

Fig. 5.4. Variations of the injected charge collection current (IChCC) (a) and microwave-probed photoconductivity (MW-PCT-E) (b) transients registered *in situ* during 8 MeV proton irradiation of a Si pad-detector when the bulk excitation density and applied bias voltage $U_R \geq U_{FD}$ were fixed.

Values of $\tau_S=f(\tau_D, \tau_R)$ estimated from the IChCC transients (Fig. 5.4 (a)) and the parameters measured by the MW-PCT-E technique (τ_R) (Fig. 5.4 (b))

and (μ, τ_D) estimated from ICDC transients (Fig. 5.3 (a)), are shown in Fig. 5.5 as a function of irradiation exposure time $t_{exposure}$. Here leakage current, proportional to the thermal emission/carrier de-trapping within the space charge region current, is presented. The reciprocal recombination lifetime (Fig. 5.5) increases with exposure time (irradiation fluence is assumed to be proportional to exposure time) nearly linearly during initial irradiation stages. At elevated fluences, however, values of the effective recombination lifetime τ_R measured by the MW-PCT-E technique on diodes with applied electric field start to saturate. This can be easily understood by a manifestation of multi-trapping effects, when several (recombination and trapping) centres act together, due to effective point defect generation during irradiation by protons. Saturation of the effective recombination lifetime, (which averages the carrier recombination and multi-trapping rate), correlates well with enhancement of leakage current relative to the irradiation exposure time scale.

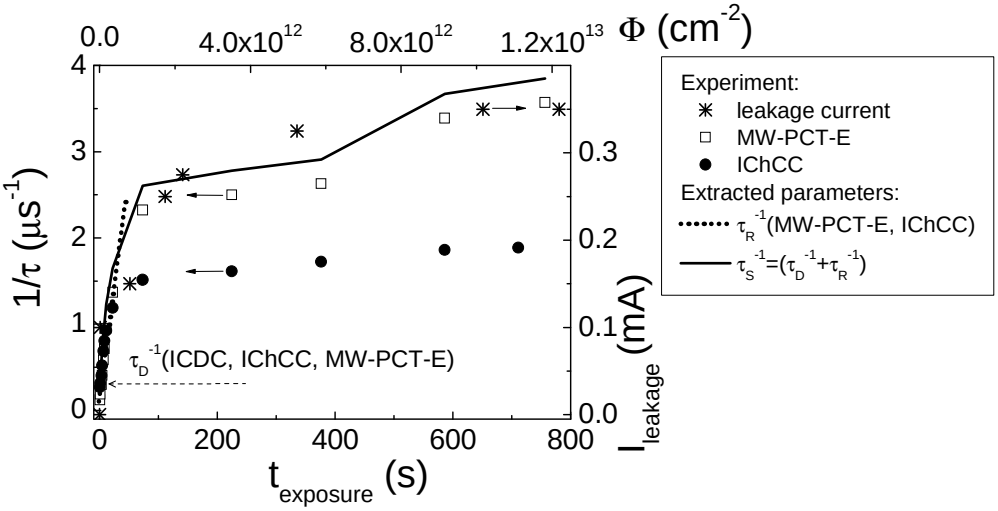

Fig. 5.5. Correlation among the carrier drift/diffusion, recombination and generation characteristics measured *in situ* (symbols) and extracted parameters (lines) ones. These characteristics were measured during 8 MeV proton irradiation of a Si detector by using the induced charge diode current (ICDC) and injected charge collection current (IChCC) transient method (circles) and by the technique of microwave probed photoconductivity with applied electric field (MW-PCT-E) (squares), respectively. Leakage current variations with fluence (stars) are also presented.

The presented techniques enable an estimation of variations of the excess carrier drift and trapping parameters. However, improved precision in

extracting parameters on high resistivity material is limited by the long Debye length for Si ($5L_D \geq 40$ μm for 1 kΩcm Si) in the evaluation of the steady-state depletion width, and by the finite width of the injected excess carrier domain ($\Delta > 6$ μm for excitation wavelength 531 nm and $\Delta > 80$ μm for red light). These widths also limit the precision in evaluating the depletion voltage values.

5.3. Variations of barrier capacitance parameters during implantation

The evolution of barrier capacitance charging current transients (Fig 5.6) was measured on diodes of *pin* structure during 1.5 MeV protons implantation. The protons beam current was kept I_{beam}=1 nA. Evolution of barrier capacitance charging current transients with irradiation exposure time can be explained by simultaneous increase of the space charge (SC) region generation current, of the dielectric relaxation time and of the consequent enhancement of series resistance within diode base region, as can be seen in Fig. 5.6. For the very initial irradiation stages, the typical barrier capacitance charging current ($i_C(t)$) transients are observed (Fig. 5.6 (a)) for the rather short (4.5 μs) LIV pulses. These transients indicate rather fast dielectric relaxation processes with $\tau_M << \tau_{PL}$. An increase of the irradiation exposure time leads to the enhancement of the SC generation current and to the increase of the total current, observed as the increment of the BELIV signal amplitude in Fig. 5.6 (a). For rather short LIV pulses this amplitude saturates, as τ_{RC} is increased, due to enhanced series resistance within electrically neutral region (ENR), as the density of equilibrium carriers rapidly falls down through recombination, when the density of radiation induced defects increases with fluence. This also leads to an elongation of τ_M. Therefore the typical transients of barrier charging currents can be observed only when the duration of the LIV pulses is significantly increased (Fig. 5.6 (b)). The SC generation current also increases and it is observed as an increment of the BELIV signal amplitude. The prevailing of SC generation current over barrier capacitance charging current can be resolved for LIV pulses in the time scale of τ_{PL} =450 μs (Fig. 5.6 (b)).

Then, the time instant, for which total current minimum ($t_e \cong$ 150 μs) is reached, can be separated.

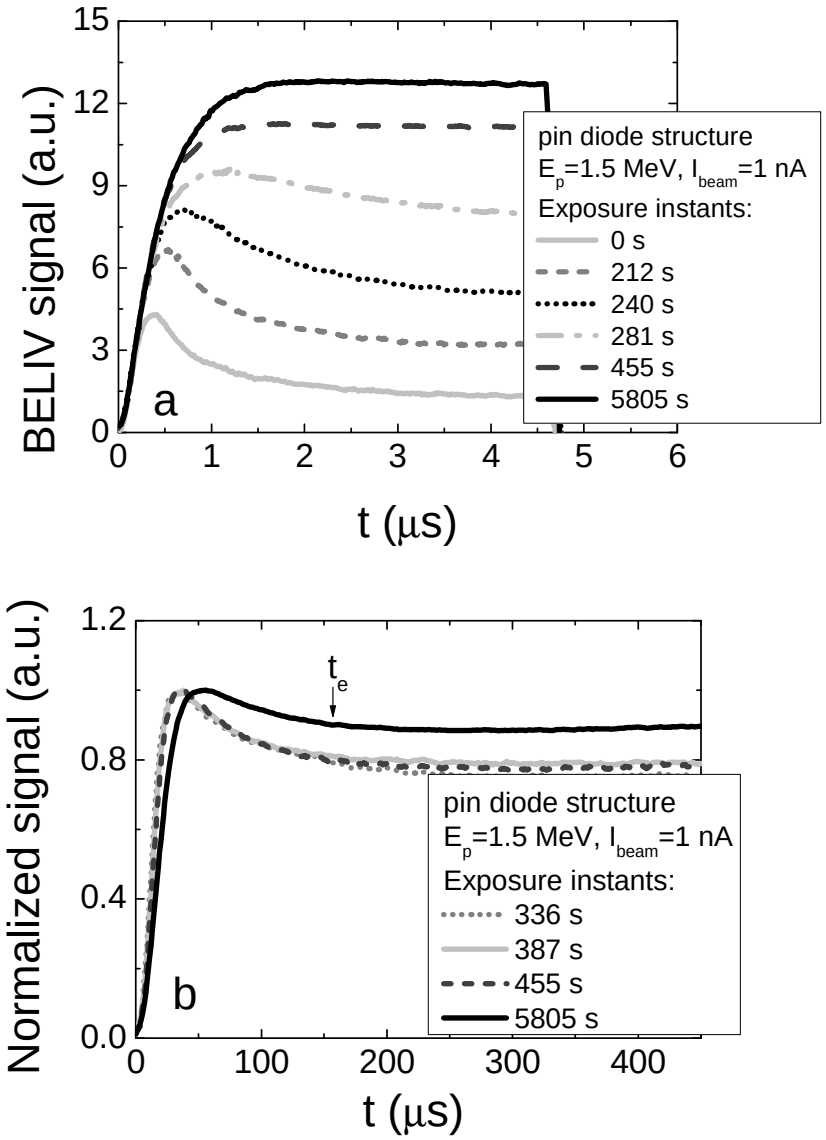

Fig. 5.6. Evolution of BELIV current transients during 1.5 MeV protons implantation at different LIV pulse durations: 5 μs (a) and 500 μs (b).

The decrement of carrier recombination lifetime [A17], revealed by the MW-PCT measurements, leads to a reduction of equilibrium carrier density within ENR and to an increase of generation current, due to emission of these captured carriers within SC region. So, the results of these *in situ* measurements of the MW-PCT and BELIV characteristics correlate well, when comparing the controlled characteristics as a function of irradiation fluence.

5.4. *In situ* control of leakage current characteristics

Control of the leakage current in diode structures during the *in situ* experiments was employed to follow changes of the penetrating particle *in situ* generated excess carriers, of impact of the nuclides reactions and relaxation as well as of the cumulative increase of the leakage current due to collected irradiation fluence.

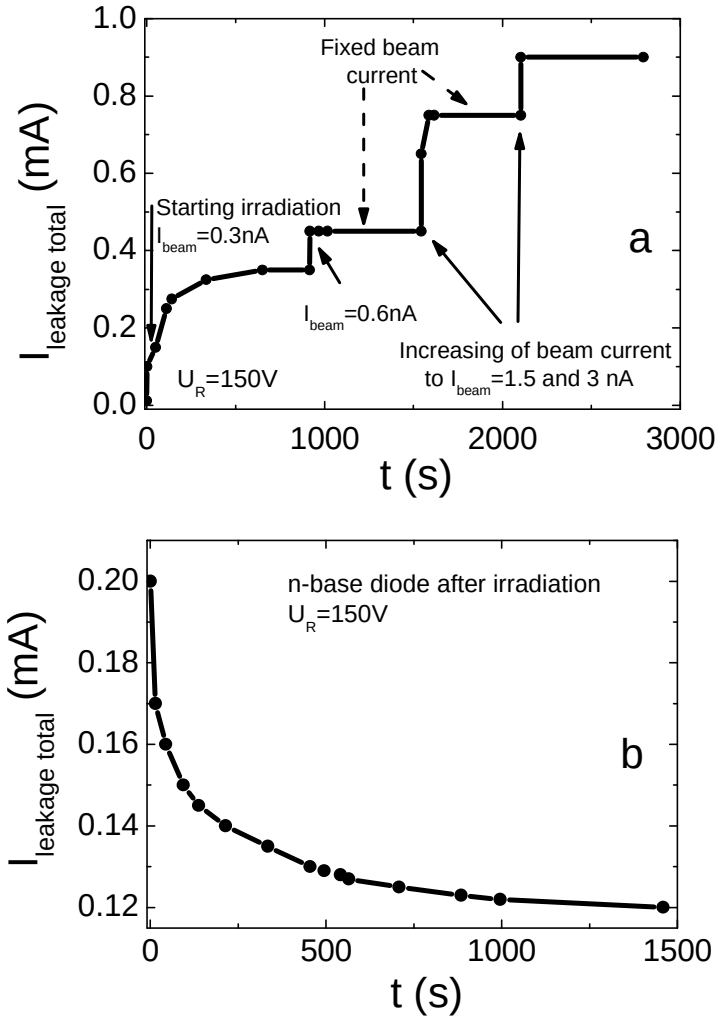

Fig. 5.7. a- Diode leakage current as a function of irradiation time. The steps correspond to increase of the proton flux. b- Leakage current relaxation due to radio-nuclide decay just after proton beam is switched-off.

During the initial irradiation stages, a proton beam current was kept rather small (of about 0.5 nA) to decrease noises and the impact ionization avalanche breakdown effects, inherent for the elevated proton fluxes [60]. During the irradiations also the beam current (i.e. flux) was altered to measure more precisely variations of the carrier recombination/transport parameters

within the diode base material ascribed to different exposure instants. The simultaneous monitoring of the leakage current revealed the corresponding (to change of proton beam current) clear steps of leakage current increase, as seen in Fig. 5.7 (a).

These changes appear due to excess carrier generation by protons [60, 61], and due to enhanced thermal emission from radiation induced carrier traps. Control of the total leakage current is also useful for estimating the impact of radio-isotopes produced by nuclear reactions during the proton bombardment. The impact can be deduced by measuring the relaxation characteristic of leakage current (Fig. 5.7 (b)) either in between of beam current change steps or just after switching off the protons beam.

Summary of the main results described in the chapter
[A10, A12, A16, A17, A19]

A multi-functional instrument and techniques suitable for the *in situ* (during procedure of irradiation by high energy protons) and simultaneous (combining various techniques) monitoring of the evolution of radiation defects and of changing of functional characteristics of Si particle detectors have been proposed, designed and approved. There, characteristics measured by techniques based on microwave probed variations of carrier recombination parameters with applied electric field, and those examined by the current transients and based on charge collection due to carrier drift-diffusion flows correlate well. Changes of the operational parameters of the Si detector structures have been additionally monitored during irradiations by measurements of leakage current which is remotely controlled.

Thereby, the designed technology of combined measurements of barrier capacitance charging current and of induced charge current pulsed transients as a function of irradiation fluence enables one to examine *in situ* an evolution of radiation defects and to determine a degradation of operational characteristics of device structures post-irradiation, by evaluating the changes of depletion width and of leakage current device characteristics and of

simultaneous variations in carrier recombination, generation and transport parameters in the irradiated material.

A small impact of radiation defects on both sign carrier drift/diffusion parameters and more complex variations of excess carrier recombination trapping lifetimes during irradiation have been revealed. The excess carrier transit, recombination and diffusion lifetimes have been evaluated by combining ICDC/IChCC current and microwave probed photoconductivity transient techniques. It has been revealed that values of the effective recombination lifetime measured by the MW-PCT-E technique on diodes with applied electric field start to saturate. This saturation is explained by manifestation of multi-trapping effect, when several centres of different species act together. Saturation of the effective recombination lifetime (which averages the carrier recombination and multi-trapping rate) correlates well with enhancement of leakage current relatively to the irradiation exposure time scale.

In situ experiments of barrier capacitance charging currents measurements during protons implantation revealed that carrier recombination processes determine the increase of dielectric relaxation time within electrically neutral region (ENR) of a diode base. This leads to the elongated time scale of stabilization of depletion width. Carrier capture/emission processes within space charge (SC) and transition layer (between ENR and SC) regions lead to an increase of generation/recombination currents in the irradiated diode.

VI. Spectroscopy and profiling of defects in device structures

6.1. C-DLTS and C-V techniques

The distribution of defects within semiconductor structures strongly determines the functional characteristics of a device. The distribution of defects and certain impurities within structures containing *pn* junction can be resolved by C-V and C-DLTS techniques.

C-V technique for the resolving of defects distribution profile is applied by analysis of the ac small test signal response $R(U_R)$ dependence on applied voltage. The $R(U_R)$ dependence for a non-irradiated *pin* diode sample, shown by black circles (Fig. 6.1), exhibits almost no variation.

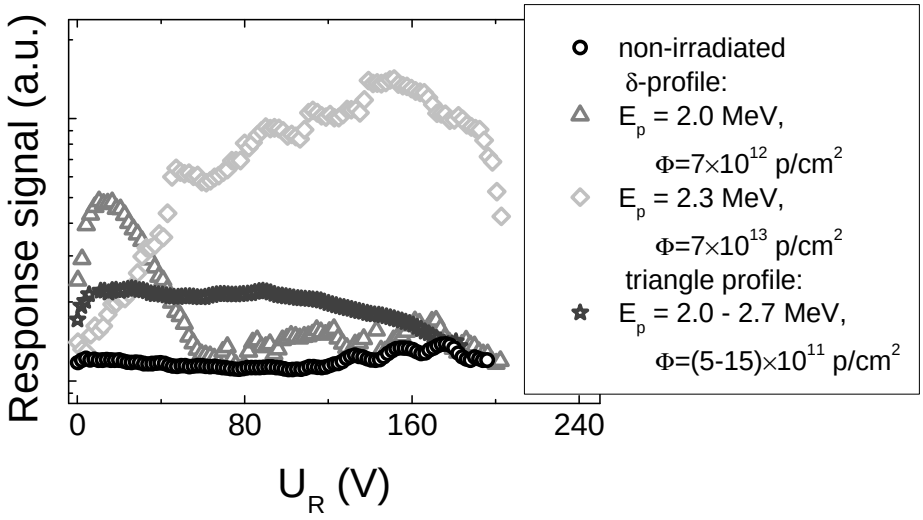

Fig. 6.1. Response signal dependence on applied voltage of the irradiated and reference industrial FZ Si *pin* diodes.

The response peaks at 14.5 V and 147.5 V appear in these dependences for samples irradiated with 2.0 MeV (grey triangles) and 2.3 MeV (light grey diamond symbols) protons, respectively (Fig. 6.1). Complementary, a profile of response *R* variations obtained for the sample with a triangle-shape radiation damage profile, is represented by dark grey stars in Fig. 6.1 and shows an increase of *R* going from the metallurgic junction to the most damaged layer position. *R* reaches a maximum at the same voltage, as determined for 2.0 MeV protons. Then, signal *R* slowly decreases with enhancement of depletion layer width over the rest base region. These observations are explained by the

competing impact of the displacement and generation currents on *R*, when dc voltage U_R governed depletion boundary crosses the differently damaged material layers.

Variations of DLS signal corresponding the distribution of density of S impurities for majority carrier traps and C, Cu for the minority carrier traps within depth (*x*) of technological *pnp* structure, obtained by differential C-DLTS technique, is presented in Fig. 6.2. Measurements were performed by controlling the variations of peaks within DLTS spectrum ascribed to S, C and Cu impurities. Variations of the amplitudes of trap filling pulses allowed of scanning of 20 μm depth within the base region in *pnp* structures.

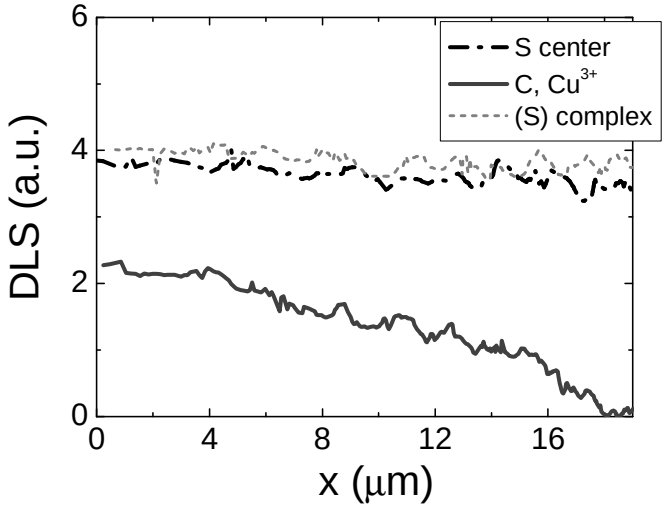

Fig. 6.2. Variations of the DLS signal corresponding to a distribution of density of impurities within depth of *pnp* structure obtained. The distance is measured in respect to the *pn* junction.

It can be seen that density distribution of majority carrier traps is almost homogeneous within structure while minority carrier traps exhibit a diffusive profile. This result indicates that S impurities might have been existed within initial Si substrate, while C and Cu impurities might have been unintentionally introduced during high temperature technological procedures.

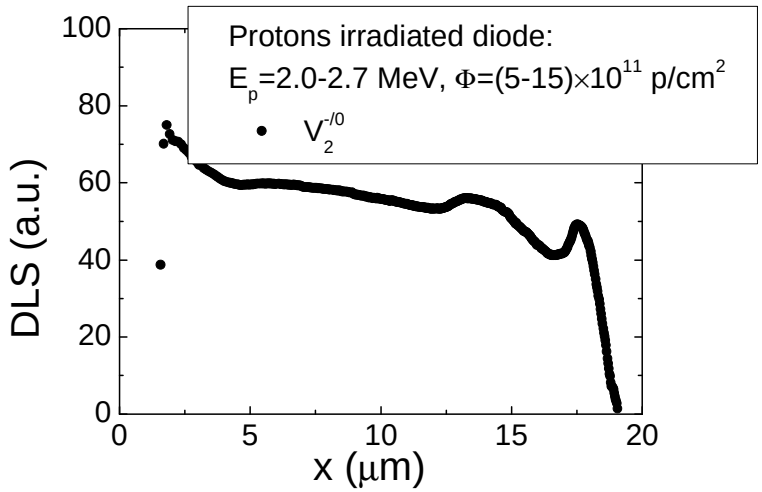

Fig. 6.3. Variations of DLS response signal corresponding the distribution of density of divacancies $V_2^{-/0}$ (0.43-0.46 eV) within diode base region irradiated by 2.0-2.7 MeV protons at a fluence of Φ=(5-15)×10^{11} cm^{-2}.

Variations of the DLS signal, correspondent to a distribution of density of divacancies ($V_2^{-/0}$) in Si *pin* diodes with induced triangle defects distribution profile of radiation defects, formed by the 2.0-2.7 MeV protons with Φ=(5-15)×10^{11} cm^{-2} fluence irradiation, is presented in Fig. 6.3. A decrease of density of $V_2^{-/0}$ is observed moving away from the metallurgic junction. However, the voltage source for the depletion of the base region provides 20 V, therefore the diode base can not be fully depleted and the signal is reduced at higher depletion voltages. Nevertheless, the $V_2^{-/0}$ density distribution within vertex of the triangle profile can be easily deduced from Fig. 6.3.

6.2. Photo-ionization spectra probed using BELIV technique

Deep level transient spectroscopy is traditionally used for the monitoring and characterization of deep levels in semiconductors by measuring changes of either capacitance [44, 62] or current [63]. Photo-ionization spectroscopy [64] can be an alternative tool with the advantage that the measurements can be performed at room temperature. Common measurement regimes in application of the mentioned methods include temperature scans or low temperature experiments, when only processes of carrier emission from deep levels are controlled. In this section, a technique for spectroscopy of deep

levels within junction device structures based on measurements of barrier capacitance charging current transient changes due to additional spectrally resolved pulsed illumination is proposed. This technique allows simultaneous monitoring of the changes of excess carrier capture and short emission lifetime based on spectrally varied deep level filling/emptying in the junction structures of semiconductor devices.

To describe principles of the BELIV-IR (infrared) pulsed spectroscopy technique, a common depletion approximation [44] is applied. Then, the barrier capacitance $C_b(t) = \varepsilon\varepsilon_0 S/w_d(t)$ temporal (t) changes under LIV pulse in n-type junction layer is ascribed (within this simplified approach) to variation of a depletion width

$$w_d(t) = [\frac{2\varepsilon\varepsilon_0(U_{bi} + At)}{q_e(N_D + (N_d - n_d(t))}]^{1/2}. \qquad (6.1)$$

Without additional IR illumination, the time dependent changes of the charge $q=CU$ within the junction, determine the current transient $i_C(t)$:

$$i_C(t) = \frac{dq}{dt} = \frac{d[C_b(t)U(t)]}{dt} = AC_b(t)[\frac{1+\frac{At}{2U_{bi}}}{1+\frac{At}{U_{bi}}} + \frac{t}{2\tau_{em}}\frac{n_d(t)}{N_D + (N_d - n_d(t))}]. \qquad (6.2)$$

This transient contains the displacement and conductivity current components. The latter component arises within transitional layer (due to free carrier "tail") at depletion boundary caused by prevailing of carrier thermal generation (from N_d traps) with increase of the depletion width $w_d(t)$ under reverse bias LIV. Here, it is assumed that trapped (at N_d) carriers are released according to $n_d(t)=n_{d0}\exp(-t/\tau_{em})$, with steady-state ($N_d$ filling) concentration n_{d0}. The thermal generation lifetime $\tau_{em}=1/[\sigma_{dth}v_T N_C\exp(-E_d/k_BT)]$ is a function of the emission cross-section σ_{dth}, of the thermal velocity v_T, of the density of states in the conduction band N_C, and of activation (E_d) as well as of thermal (k_BT) energy. As usually, several trap species of different types appear. Generation currents from slower and deeper traps contribute simultaneously to the leakage

current, which is expressed as $i_g(t)=q_e n_i w_d(t) S/\tau_g$, through the averaged lifetime τ_g as well as through intrinsic carrier density n_i.

At room temperature, values of carrier thermal generation lifetimes, even for moderately deep ($E_i<E_d<E_C$) donor-type centres in Si, appear to be in the range from a few ns to μs (Fig. 6.4 (a)) for traps with σ_{dth} in the range of 10^{-16} – 10^{-14} cm^2. Therefore, only traps with short carrier capture lifetimes ($\tau_{capt}/\tau_{em}<1$) can be filled. Carrier capture lifetime τ_{capt} is a reciprocal function of the trap density, N_d: $\tau_{capt}=1/\sigma_{dth} v_T N_d$. Thus, impact of generation current ascribed to the single type traps can be observable as an initial recess within the BELIV transients when density of these traps approaches to or exceeds the concentration N_D of shallow dopants. The simulated (using Eq. 6.2) BELIV transients (curves 1-3) obtained varying n_{d0} are illustrated in Fig. 6.4 (b). It can be noticed in Fig. 6.4 (b), that initial recess within the barrier charging current transient is observed when rather large density of initially filled traps exists. In the opposite case, when several species of traps compete in capturing free carriers, only partial and rather low filling of these traps is possible (carriers of low density are redistributed among different traps). Then, generation-leakage current i_g increases with LIV voltage, At, and can exceed the barrier charging current in the rearward phase of the transient. The descending charge extraction (displacement current) component and the ascending generation i_g current component imply the existence of a current minimum in the current transient [A12], which can be highlighted using increased LIV pulse duration.

Photo-ionization of trapped carriers n_d by using short (fs) pulses of spectrally well resolved IR light enables one to determine parameters of deep traps and state of their filling. Short IR pulse with incident $h\nu$ energy photons of surface density $F(h\nu)$ integrated per pulse duration makes a δ-shape (~0.2 ps within scale of BELIV μs pulses) optical emission of trapped carriers, if $h\nu$ fits to E_d and cross-section $\sigma_{p\text{-}e}$ of photon-electron interaction is sufficient.

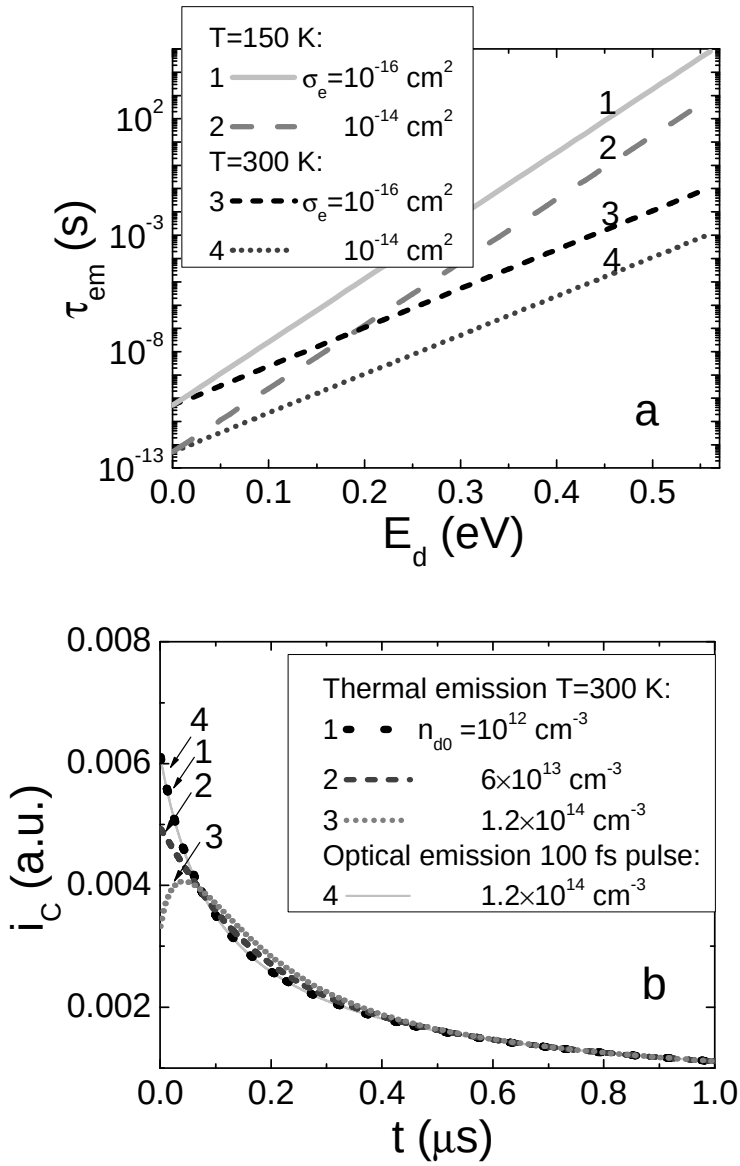

Fig. 6.4. a- Simulated thermal emission lifetimes at 150 K (1,2) and 300 K (3,4) temperatures for traps with emission cross-section σ_e=10^{-16} cm^2 (1,3) and σ_e=10^{-14}cm^2 (2,4), respectively. b- Simulated barrier (N_D=7×10^{13} cm^{-3}) charging current transients when carriers of different density n_{d0} trapped at deep donor centres (N_d=1.2×10^{14} cm^{-3}) are released thermally (1-3 curves) and by short IR light pulse (4).

The cross-section $\sigma_{p\text{-}e}$ for electrons located in deep levels is widely [44, 64] described by the Lucovsky model [65]:

$$\sigma_{p-e}(h\nu) = \frac{BE_d^{1/2}(h\nu - E_d)^{3/2}}{(h\nu)^3} \tag{6.3}$$

where B is a multiplicative factor. The spectral changes of the absorption coefficient $\alpha(h\nu)$ due to photo-ionization can be described by

$$\alpha(h\nu) = \sigma_{p-e}(h\nu) n_{d0}. \tag{6.4}$$

This change of the absorption coefficient can be controlled by *hν* light induced optical transmission measurements. IR induced absorption measurements are performed in nearly wave-guide regime within layered device structures. Illumination by IR light pulse of surface density $F(h\nu)$ leads to density of the photo-emitted carriers:

$$n_d^* = \sigma_{p-e}(h\nu) n_{d0} F(h\nu) . \qquad (6.5)$$

By substituting n_d^* Eq. (6.5) (with $n_d^* = n_d(t)$), into Eq. (6.1), a value for the barrier capacitance charging current due to photo-ionization can be extracted. The simulated (using Eqs. 6.1 and 6.5) BELIV transient (curve 4) is illustrated in Fig. 6.4 (b). The filling factor n_d/N_d can be controlled by combined measurements of i_C peak value or $\alpha(h\nu)$ (as well as n_d^*) as a function of $F|_{h\nu}$, and saturation of these characteristics indicates the complete photo-ionization of N_d traps. Generation current parameters can be extracted by combined analysis of the BELIV current transients measured with and without IR illumination. Photo-ionization within electrically neutral region leads to a reduction of the dielectric relaxation time and of the serial resistance in the junction structure. The enhanced density of excess carriers within electrically neutral region decreases duration of the initial rise to peak current, as discussed elsewhere [A14], and results in a thinner Debye length of the transitional layer nearby the depletion boundary.

Activation energy E_d of N_d traps can be evaluated by spectral measurements of changes in BELIV current transient shape and initial peak amplitude and using Eqs. (6.3-6.5). These spectral measurements are as usually started from the long wavelength wing to avoid simultaneous trap filling/emission from deeper centres. Value of E_d can be evaluated as quantum energy *hν* for which the red-threshold of the IR modified i_C increase is observed. Alternatively, E_d and $\sigma_{p\text{-}e}(h\nu)$ can be estimated by combining simulations of the BELIV current amplitudes based on Eqs. 6.3-6.5.

The simplified description of principles of the technique of photo-ionization probed barrier capacitance charging transients is presented above by

analyzing the donor type traps. Both acceptor and donor type defects acting together can be found in real experimental practice. Analysis of such models (when acceptors behave like compensating centres, while donors are able to follow fast changes in pulsed voltage) could be found e.g. in monograph [44]. The BELIV-IR (infrared) pulsed spectroscopy technique is preferential to evaluate material characteristics at room temperature when density of traps is large. However, an impact of the electron-phonon interactions within room-temperature photo-ionization spectroscopy should be estimated. In high resistivity materials, deep traps of high density are partially filled due to lack of free carriers.

6.3. Instrumentation for pulsed spectroscopy

A schematical representation of the measurement set-up needed for implementation of BELIV-IR pulsed spectroscopy is shown in Fig. 6.5.

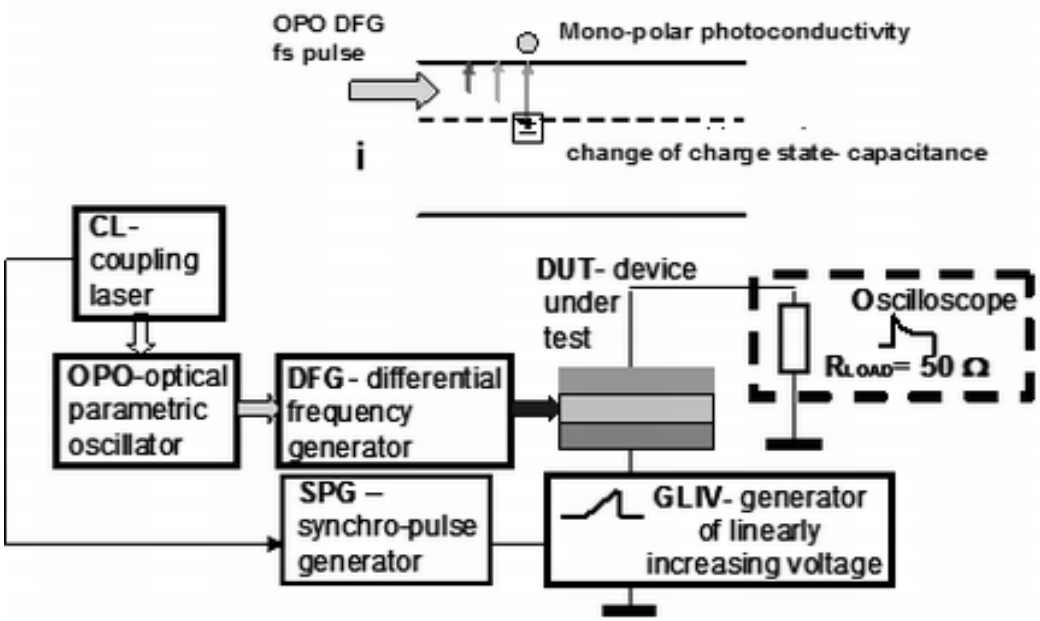

Fig. 6.5. Schematic representation of the measurement setup. In the inset (i) the illustration of monopolar excess carrier generation is sketched.

The barrier charging current transients have been used as a probe for the analysis of the excitation spectrum resulting from pulsed illumination with variable wavelength light of the device under test using a differential frequency generator (DFG) coupled with an optical parametric oscillator (OPO). The

OPO-DFG laser system enables to vary the illumination wavelength (λ) in the range between 1.2 and 10 μm with a precision of 100 nm using 100 fs pulses of the main coupling laser (CL). The triggering system of the main laser also generates synchronization pulse which starts the LIV generator (GLIV) through a synchronization pulse generator (SPG).

The SPG forms a pulse of suitable duration to handle the sequence of LIV pulses and, thus, the optical (OPO-DFG) and electrical (LIV) pulses are synchronized. The OPO-DFG illumination of the device under test (DUT) leads to photo-ionization of carriers from the filled deep traps. The pulsed light biasing has been used to modify the occupation of the trap states and to highlight the dominant components of current. The illumination wavelength range of 2 to 10 μm determines a monopolar excess carrier generation (as sketched in the inset of Fig. 6.5), which causes both a generation current (i_g) within the space charge region (SCR) of the junction and a monopolar photoconductivity within the electrically neutral region (ENR). The photo-ionization caused current changes are analyzed by control of the shape and the amplitude of the barrier capacitance charging current (BCC) transients. These BCC transients are registered using a 50 Ω load input of a DSO6012A oscilloscope. Additionally, the measurement circuitry contains the adjustable output of a generator of linearly increasing voltage (GLIV) and the device under test (DUT), connected in series. The other channel of the digital oscilloscope is used for synchronous control of the linearity of the GLIV signal using a signal differentiating procedure installed in the DSO oscilloscope.

6.4. Deep level spectra in thyristor structures and irradiated detectors

The BELIV-IR (infrared) pulsed spectroscopy technique was applied to analysis of deep level spectra in the Si thyristor and *pin* detector structures. Industrial non-capsulated Si thyristor n^+pnp structures with well defined layer thicknesses and doping (N_D=7×10^{13} cm^{-3}, phosphorus doped n-layer) densities were used for recording deep level spectra in a 350 μm thick n-Si layer. The

tentative measurements on deep level transient spectroscopy (C-DLTS) in these n^+pnp structures showed technological contaminants of significant density within n-layer. Also, a set of *pin* diodes of CERN standard were investigated.

6.4.1 Deep level spectra in thyristor structures

For an n-layer containing a high density of deep traps, the barrier capacitance charging (BCC) current transient (**A-** and **C**-type transients illustrated in Fig. 6.6 (a)) contains an initial recess. This recess within a BCC transient indicates a reduced $AC_b(t \cong 0)$ barrier charging current due to trap filling. It can be seen in Fig. 6.6 (a) (**B**-type transients), that an illumination pulse of fixed density and at a fixed wavelength (λ=4 μm) restores the initial peak associated with the barrier charging current. This happens when emptying of the carrier capture donor-type centres in the material is saturated by a sufficient density of illumination ($F(h\nu)$). Due to the emptied centres, the initial recess disappears in the BELIV transient. It can be also inferred that value of the carrier capture lifetime determines the relaxation of the value of the initial current peak associated with the barrier charging (Fig. 6.6 (a), **B**-type transients). The photoconductivity current can be additionally estimated by analysis of the pedestal signal between the sequences of **B**-type transients. The amplitude of this pedestal signal decreases together with that of the BCC signal. The evolution of BCC transients illustrated in Fig. 6.6 is obtained only for fixed wavelengths of IR illumination.

Varying the wavelength of this OPO-DFG IR pulsed illumination, a spectrum of deep levels is obtained. Additional measurements of the capacitance voltage (C-V) and current-voltage (I-V) characteristics on thyristor structures, by separately connecting the different junctions of the structures to a measurement circuitry and by using the same samples, indicated a large leakage current. The capacitance dependence on the ac test signal frequency suggests that the characteristic lifetimes of carrier capture are of the order of magnitude ~ 1 μs. This is directly corroborated by the analysis of the shape of

BCC transients observed for different intensities of the OPO-DFG IR illumination, whereby the generation (leakage) current dominates over the barrier capacitance current for GLIV pulse durations of τ_{PL}>1 μs.

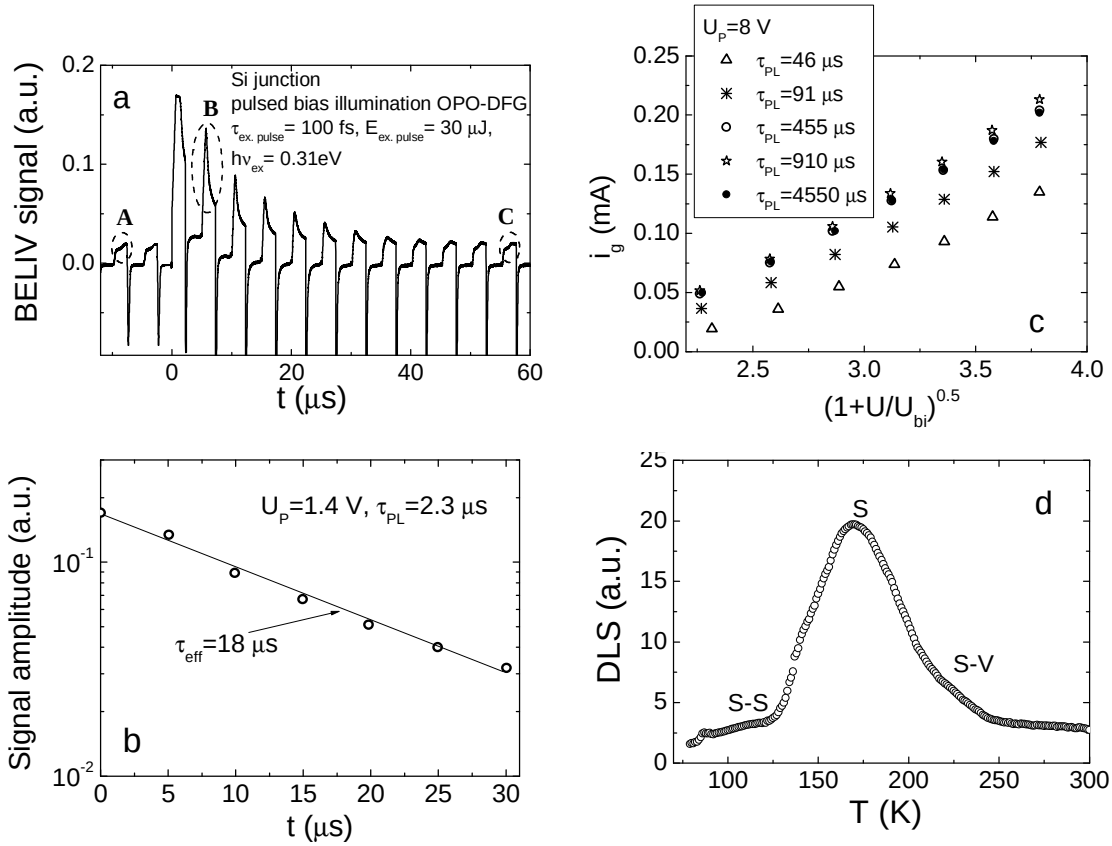

Fig. 6.6. a- A sequence of BCC transients measured in a Si thyristor junction structure. **A** indicates a typical transient determined by carrier capture into deep traps before IR illumination pulse, **B** shows a modified BCC transient just after IR illumination (λ=4 μm) by 100 fs pulse, and **C** illustrates the recovered BCC transient after photo-ionized carriers are re-trapped by deep centres. b- Relaxation of the initial amplitude of the B-type transients within semilog scale and evaluation of the carrier recombination/capture lifetime. c- Generation current as a function of $(1+U(t)/U_{bi})^{1/2}$ and LIV pulse duration. d- C-DLTS spectrum measured in the Si thyristor junction structure. The DLTS peak ascribed to a single charged sulphur (S) dominates, and S_i –S_s as well as sulphur vacancy (S-V) associated peaks, interpreted according to [66-68], are also denoted.

To verify the existence of defects in the n-base region and to identify the traps responsible for the generation current, C-DLTS spectra have also been recorded on the same device structures (Fig. 6.6 (d)). The prevailing peak in the range of 150 -200 K is obtained in the C-DLTS spectrum which is ascribed to the sulphur contaminant impurities [66-68] with activation energy

of 0.3 eV and cross-section of σ_{dth}~5×10^{-16} cm^2. Due to high density of technological contaminants, only qualitative evaluation of trap concentration and other DLTS signatures is possible when trap density approaches to or exceeds the doping density.

The obtained DLTS spectra actually corroborated the existence of deep traps as revealed by the BELIV-IR spectroscopy measurements. Our results illustrates that the proposed BELIV-IR pulsed spectroscopy technique permits time resolved spectroscopy with the simultaneous determination of carrier capture and emission lifetimes. Calibration of the illumination density at each wavelength (simultaneously measured in our experiments) would enable to determine the concentration of each of the deep traps resolved as a spectral peak in the n-layer of the n^+pnp structures.

6.4.2 Deep level spectra in the irradiated detectors

Prevailing of the barrier charging current (Fig. 6.7) has been observed in Si *pin* detectors irradiated with a rather low fluence of reactor neutrons ($\Phi\leq10^{13}$ n/cm^2). The photo-ionization peaks probed by the BELIV current transients are determined varying illumination quanta $h\nu$.

Evolution of the barrier capacitance charging (BCC) transients, illustrated in figure 6.7 (a), as a function of the illumination wavelength for the same quanta flux (calibrated OPO-DFG energy per pulse) shows photo-ionization peaks. These peaks associated with activation energy values of E_1=0.3±0.02 eV, E_2=0.41±0.01 eV and E_3=0.51±0.01 eV (ascribed to divacancies of different charge state $V_2^{=/-}$, $V_2^{-/0}$ and defect clusters, respectively) have been revealed in an n-Si layer with a dopant density of $N_D\approx10^{12}$ cm^{-3} irradiated with $\Phi=10^{13}$ n/cm^2. The best fit of these peaks, simulated by using Eqs. 6.1-6.5 (and $[N_D-(N_a-n_a(t))]$ when necessary, with N_a the density of acceptor-type traps and their temporal filling $n_a(t)$) can be associated with well-known [5] deep centres ascribed to radiation defects. In Fig. 6.7 (a), it can also be noticed, that the capture lifetime varies for different

deep traps, as deduced from the BCC amplitude reduction rate within a sequence of transients at fixed illumination wavelength.

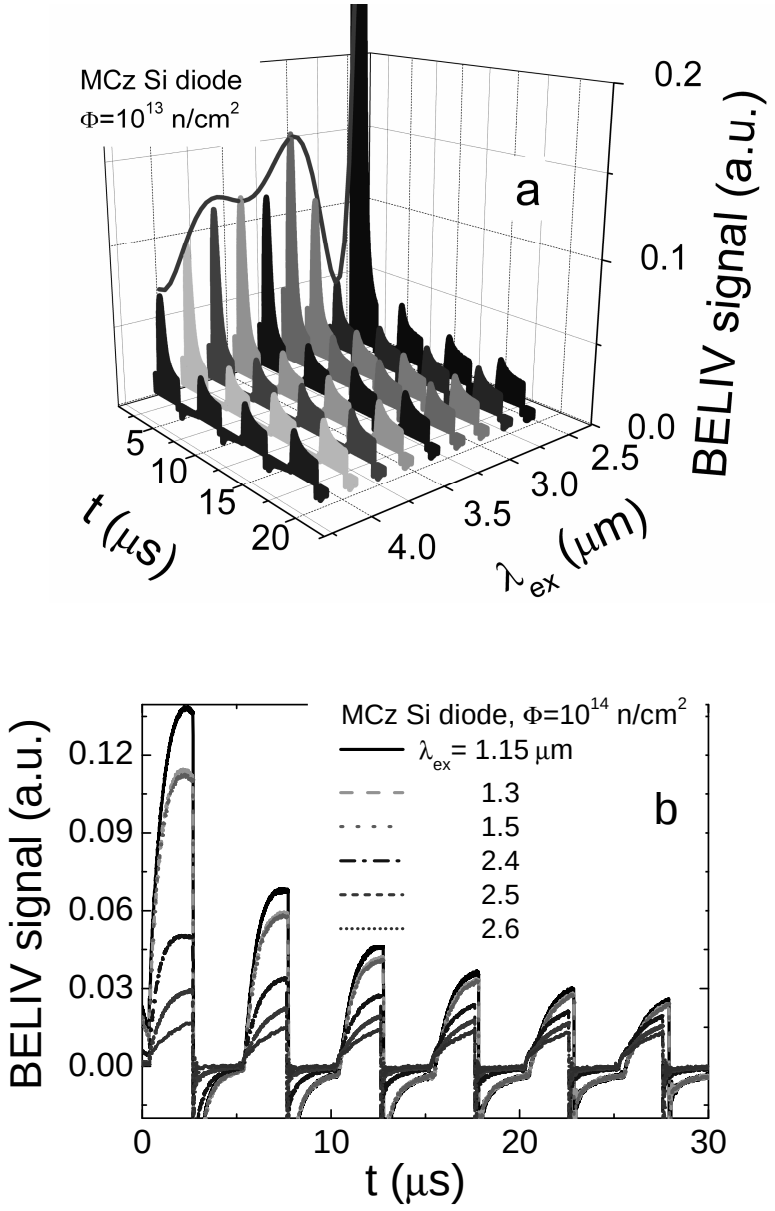

Fig. 6.7. BCC transients as a function of wavelength and time measured in Si *pin* detector structures irradiated with 10^{13} (a) and 10^{14} (b) n/cm^2 reactor neutrons fluence.

In Si *pin* detectors irradiated with $\Phi \geq 10^{14}$ n/cm^2 fluence, when the deep trap density exceeds that of the shallow dopants, the generation current i_g dominates in the BCC transients, even when using the highest illumination density of the OPO-DFG source, being the IR spectrum brightest laser, and rather short LIV pulses. The evolution of the BCC transients shown in Fig. 6.7

(b) can be explained by a simultaneous increase of the SC generation current (i_g) and of the dielectric relaxation time. This leads to an increase of series resistance of the ENR n-Si region. A high density of deep traps also leads to a partial filling of the different deep centres due to a lack of "native" equilibrium carriers which is determined by the shallow dopants of low ($N_D \approx 10^{12}$ cm^{-3}) concentration. Then, deep traps characterized by the longest carrier emission lifetime (i.e. the deepest centres) which exceeds the carrier capture lifetime can be filled. This prediction is proven in our experiments on the Si *pin* detectors heavily irradiated with neutron fluences in the range of $\Phi = 10^{14}$ to 10^{16} n/cm^2, when a threshold for photo-ionization is observed for quanta of energy $h\nu \geq 0.5$ eV. The BELIV-IR spectral peak revealed in Fig. 6.7 (b) can only be obtained for an OPO illumination wavelength of $\lambda \approx 1.2$ μm, which is close to the inter-band excess carrier photo-generation. This illustrates that the BELIV-IR spectroscopy technique is applicable even in the case of a high density of traps.

One of the limiting factors in extracting the activation energy value (when using threshold wavelength for photo-ionization of definite traps) is spectral width $\Delta(h\nu)$ of OPO radiation. The spectral broadening of fs pulsed radiation is about $\Delta(h\nu)$=10-80 meV, and this broadening increases with wavelength. However, at room temperature, relatively shallow levels are thermally ionized, and $\Delta(h\nu)/h\nu \cong$ 2-20 % for the observed peaks. OPO pulses of ps duration are preferential to reduce spectral broadening of tuneable wavelength IR illumination. Actually, illumination at peak wavelength dominates within photo-ionization of trapped carriers when using fs pulses. The BELIV-IR spectroscopy technique is preferential when traditionally used methods (e.g. TSC – thermally stimulated currents at 300 K and DLTS at high density of several species traps in samples with large leakage currents) are non-operational.

6.5. Instrumentation for pulsed profiling of dopants and traps

The distribution of dopants density and depth of junctions within layered structures can be resolved by employing slightly modified measurement setup of the BELIV technique. A sketch of measurement setup is presented in Fig. 6.8. Current transients are measured using a 50 Ω load resistance and measured by oscilloscope. Additionally, the measurement circuitry contains an adjusted output of a generator of linearly increasing voltage (LIV) and a junction structure under investigation, connected in series.

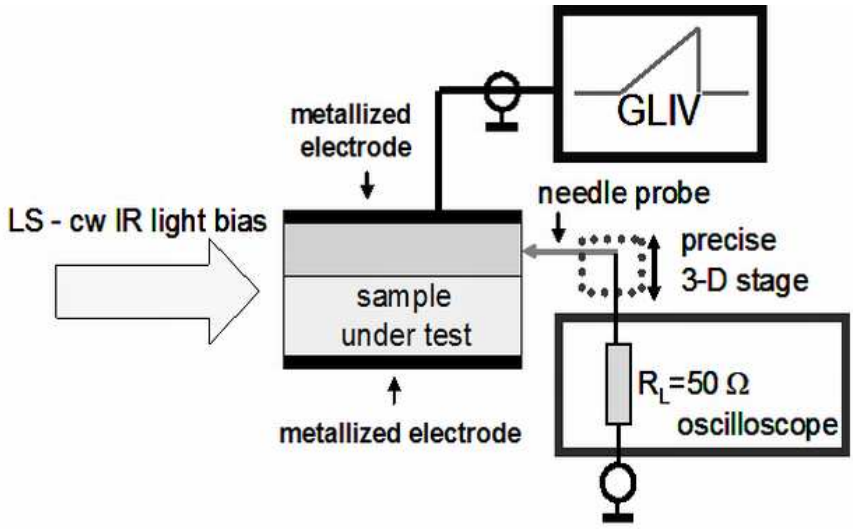

Fig. 6.8. Sketch of the circuitry for the implementation of BELIV profiling.

The cross-sectional boundary of a layered junction structure is scanned by a gold needle-tip positioned by a precise 3-D stepper. The micro-structure of the needle-tip (making a slightly non-ohmic electrical contact) determines the appearance of the spreading currents between the main plate electrode (a deposited metal layer) of a relatively large area and the needle-tip on a boundary of a structure located (perpendicularly to the main electrode) within a definite layer and at definite depth point. The electrical contact between the needle-tip probe and sample is controlled by reaching the maximum current and manipulated by pressing the needle probe. Position of the probe on boundary is changed by pull-shift-press procedures in sequence using a 3D stage and keeping a fixed pressure on probe. The boundary of the samples for depth profiling must be as smooth as possible. The needle-tip is

sharpened by mechanical/chemical procedures. A complementary continuous-wave infrared (IR) light source, either a laser with wavelengths in the range of 1 - 5 μm or a photo-metric 350 W lamp, is employed to vary the filling of deep centres.

6.6. Profiling of *pin* and thyristor structures using BELIV technique

The models presented in chapter 3.3.2 (for parallel configuration of plate electrodes) are employed to describe the measured transients. For electrodes of the perpendicular configuration, when a needle-tip is positioned on the cross-sectional boundary of a parallel-plate layered structure, the current spreading effect should be included. The spreading of current in a material of resistivity ρ acts as a serial resistor $R_S=\rho l_{eff}/S_{eff}$ introduced into the BELIV measurement circuit. Here, l_{eff} and S_{eff} are the effective length integrated over the current trajectories and an effective area in formation of spreading currents, respectively. The latter is very sensitive to R_S changes. The simulated (using TCAD software for specific configuration of probes) distribution of potential is illustrated in Fig. 6.9.

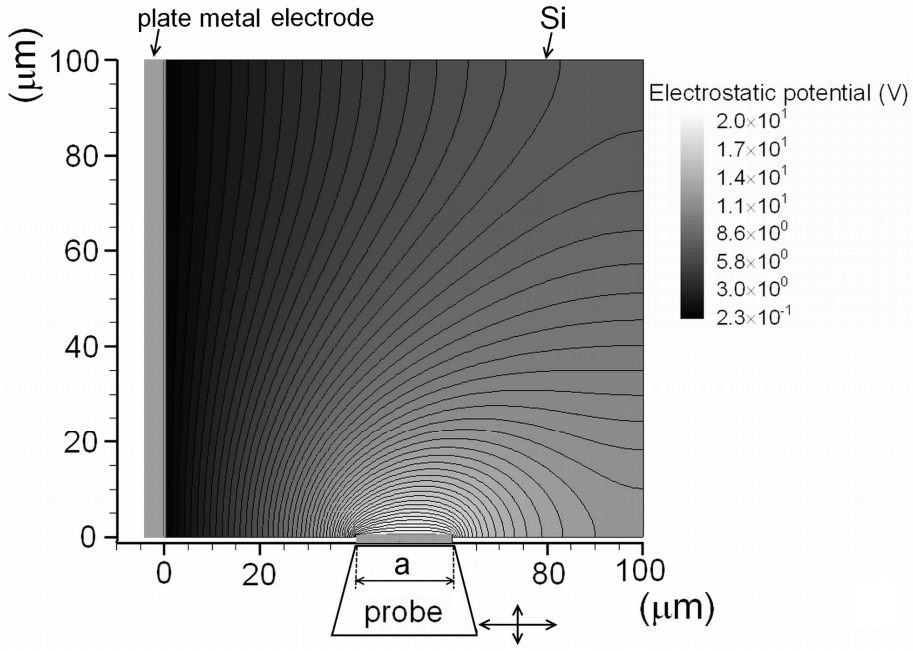

Fig. 6.9. The simulated (using TCAD software for specific configuration of probes) distribution of potential.

For a high symmetry of the measurement configuration, as in common spreading resistance measurements, the approximation $l_{eff}/S_{eff}=1/2a$ (here a is the diameter of the probe) can be used. Actually, the rather low symmetry of the geometrical configuration used in the present study, does not allow simplifications. Therefore, complicated numerical simulations (starting from the solution of the Poisson equation) are inevitable to model the changes of the transients during profiling. It can be noticed in Fig. 6.9 that the concentration of the electric field and consequently of the current density is significantly enhanced at the beginning (edges) of the probe. Thus, the spatial resolution of profiling can be higher than that evaluated using the diameter (a) of the needle-tip-probe. To evaluate the ratio of l_{eff}/S_{eff} and the absolute values of R_S, $N_{D,}$ a calibration procedure should be used which can be performed by varying U_P, τ_{PL}, R_L and using a set of material samples combined with a definite probe system.

This profiling technique was applied for the *pin* diode structures (presented in Fig. 3.1 (b)) for evaluation of dopants distribution and depths of junctions. The specific variation of the BELIV transients is illustrated in Fig. 6.10 (a).

Profiles of the peak amplitudes and of durations of the BELIV pulse τ_{BELIV} are shown in Fig. 6.10 (b). τ_{BELIV} is the time interval between the barrier charging current peak and the end of LIV pulse whereby these peculiar points can be distinguished precisely. For locations of an Au probe within a cross-sectional boundary (shifting the probe by 3D stage) in the vicinity of the metallic plate electrode and of the high conductivity emitter (p^+) layer, the amplitude and shape of the BELIV transient is close to that of the LIV pulse (Fig. 6.10 (a)). The decrease of the peak amplitude for probe locations within a relatively high resistivity layer is determined by the spreading resistance (due to the needle-tip probe). Thus, the BELIV transient is governed by the main junction of the diode under investigation.

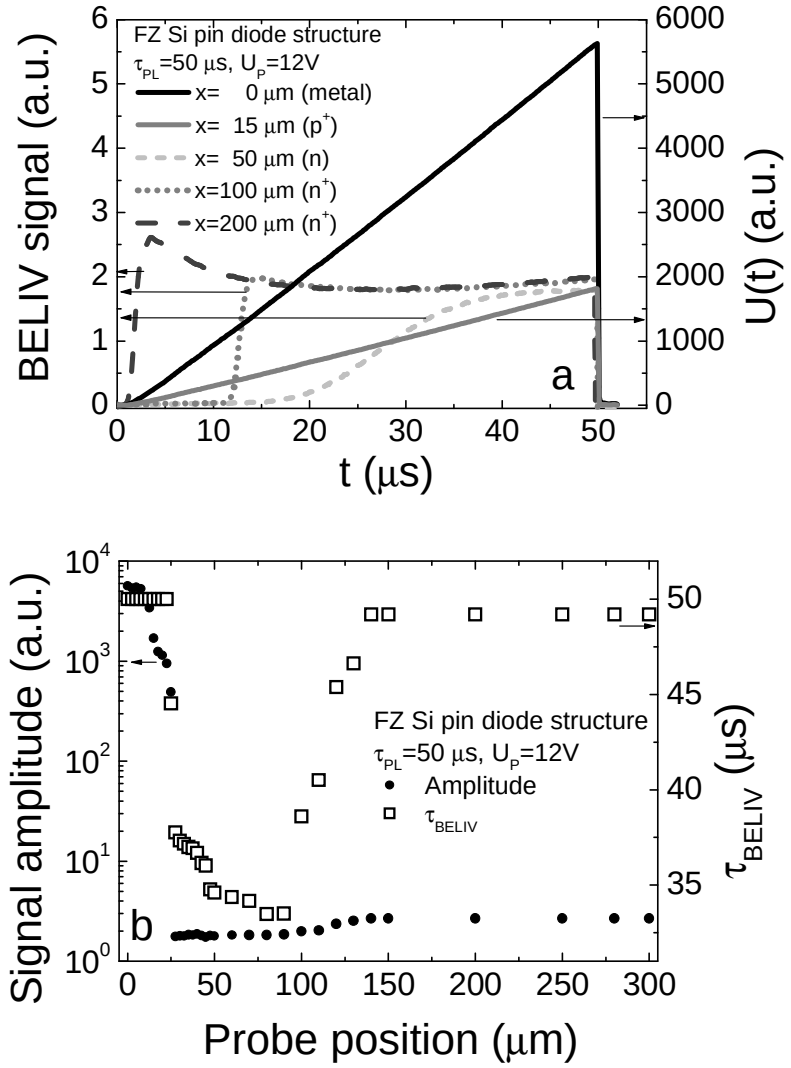

Fig. 6.10. a - Variations of the BELIV transients in a p^+nn^+ structure of a *pin* diode for a probe positioned (x) within different layers. b- Variations of the amplitude and the BELIV pulse duration, obtained by depth-scans of the p^+nn^+ structure.

The shape of the registered transient is inherent for the diode which is reverse biased by the LIV pulse, in this case. Then, a rise of this current is either significantly stretched within the initial front of the BELIV pulse or even shifted over the time scale (Fig. 6.10 (a), curves for location of probe at 50 and 100 μm) causing a shortening of τ_{BELIV}. An increment of R_SC_{b0} induces a shift of the current peak (AC_{b0}) towards the longer time scale relatively to the beginning of τ_{PL} and to the initial step of dU_P/dt for the LIV pulse.

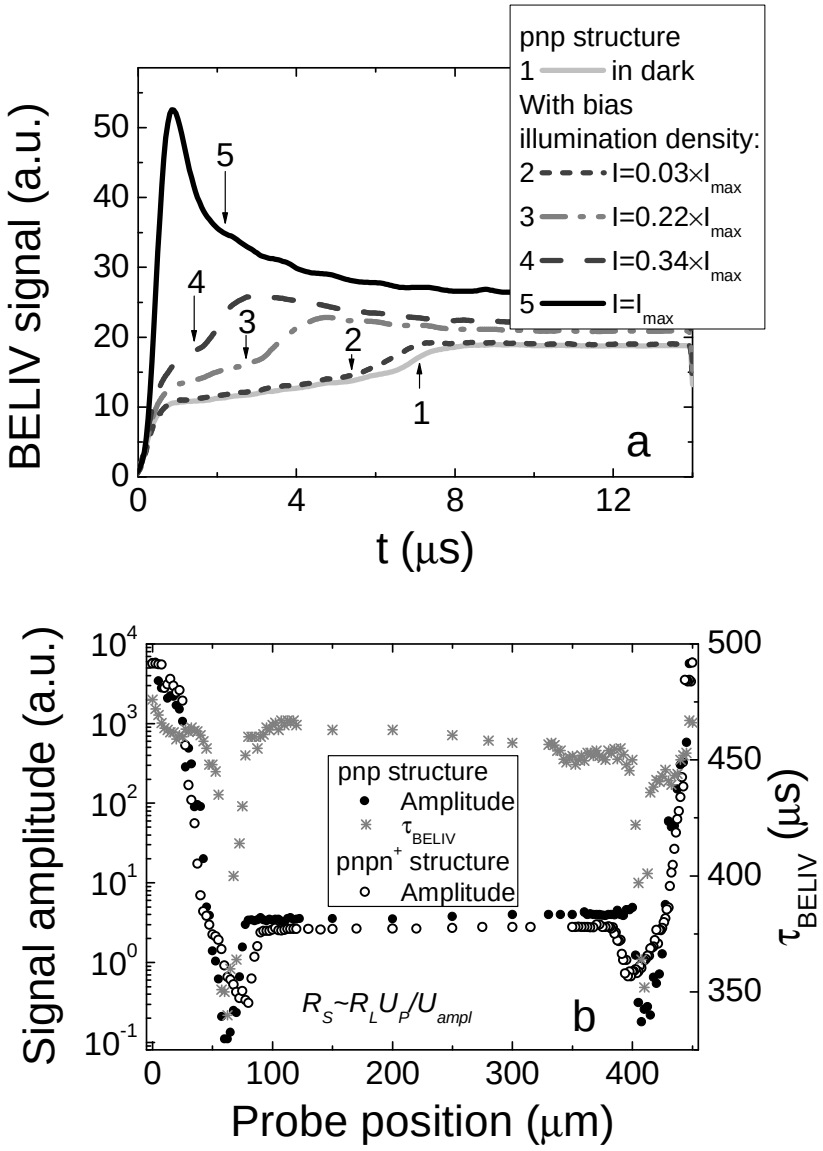

Fig. 6.11 a- Bias illumination (BI) density dependent charge extraction current transients measured at a fixed position of a needle probe (within the n-type bulk of the *pnp* structure) for the same reverse (U_P) voltage of LIV pulses. b- Comparison of the amplitude (black solid symbols) and τ_{BELIV} (grey stars) profiles for *pnp* (solid symbols) and completely fabricated thyristor (open symbols) structures.

The amplitude and duration (τ_{BELIV}) of the BELIV transient are restored (Fig. 6.10 (b)), by moving the probe from the highest resistance (n-base) region towards enhanced conductivity layer (n^+). The regeneration of the amplitude and the reduction of the delay for transients registered behind the n/n^+ interface are caused by the decrease of the resistivity within the n^+-layer and by the decrement of R_S. Then, nearly the whole n/n^+ interface acts as another parallel-plate electrode leading to an increased effective area. The range of the inherent

changes in the BELIV transient (for both the amplitude and τ_{BELIV}) clearly indicates the geometrical dimension of the layer of the highest resistivity over the structure, Fig. 6.10 (b). Fitting of the simulated characteristics to the experimental data enables to extract the parameters of spreading resistance and of barrier parameters.

A crucial impact of impurities induced deep centres on the BELIV profiling has been found within *pnp* structures and on commercial (n^+pnp) thyristor structures. Therefore, the BELIV technique has been applied in this case using also additional steady-state infrared bias illumination (BI). For layers containing a high density of traps, the BELIV transient (illustrated in Fig. 6.11 (a)) recorded for a single scan point contains an initial recess. The latter observation indicates a reduced AC_{b0} barrier charging current due to traps filling, if density of BI is insufficient. This impact of traps can be highlighted or suppressed by the enhancement of the steady–state BI density. The initial recess in the BELIV transient disappears with increasing IR light density, Fig. 6.11 (a). The disappearance of the initial recess in the BELIV transient indicates that carrier capture centres are filled and recombination current is reduced. The profiles of the amplitude of the BELIV response (measured with proper BI) obtained for *pnp* and n^+pnp structures are illustrated in Fig. 6.11 (b). These scanned profiles are associated with the extent (spatial dimension) of the doped layers and of interfaces (*pn* and *np*) between them. The drop of the BELIV amplitude, obtained going from p- to n-layer, represents a change in doping from 10^{17} to 10^{13} cm^{-3}.

Summary of the main results described in the chapter

[A14, A15, A18, A20]

It has been demonstrated that distribution of defects and of certain traps can be alternatively evaluated by employing C-V and C-DLTS techniques.

The proposed BELIV-IR pulsed spectroscopy technique can be employed as a powerful tool for the examination of deep levels in the junction area of semiconductor device structures at room temperature. This technique

allows for the simultaneous measurements of the excess carrier capture and short emission lifetime within the resistive junction layer of a semiconductor device structure. Spectra measured by the BELIV-IR pulsed technique have been compared with those registered by C-DLTS on the same Si thyristor structures in the case that the dopant density is close to that of the trap concentration showing good agreement between both techniques.

The activation energy of the trap within bandgap was evaluated to be 0.3 eV and ascribed to sulphur impurity within the sample of p^+npn structure. The photo-ionization peaks (within measured spectrum) with activation energy values of E_1=0.3±0.02 eV, E_2=0.41±0.01 eV and E_3=0.51±0.01 eV in an n-Si layer with a dopant density of $N_D \approx 10^{12}$ cm^{-3} irradiated with $\Phi=10^{13}$ n/cm^2 were obtained.

The distribution of dopants density as well as the depth of junctions of layered structures can be evaluated by employing the BELIV technique for a cross-sectional scan of the boundary of the structure with a needle-tip probe.

Thus, the designed BELIV technique of barrier capacitance changes under linearly increasing voltage pulses and instrumentation, implemented by applying either cw or pulsed bias illumination of different intensity as well as of spectral range, can be employed for spectroscopy and for profiling of impurities and radiation defects in Si junction structures.

VII. Modification of the switching characteristics of power *pin* rectifiers

The switching characteristics of *pin* rectifiers can be effectively modified by employing protons implantation at various depths and consequently creating various profiles of enhanced recombination region within the diode base. In this chapter results of investigations of the modifications of switching characteristics in *pin* diodes are presented.

7.1. Irradiation regimes

Commonly gold diffusion procedure is included within technological route of production of these diodes for the modification of reverse recovery time (RRT) parameters. However, gold diffusion procedure was omitted from the technological route of production of these samples. These samples were irradiated by protons at Helsinki University Accelerator Laboratory (HUAL) in order to achieve fast (~140 ns) switching rates and a soft reverse recovery characteristic. The irradiation regimes were simulated by employing the SRIM – Stopping and Range of Ions in Matter software [69]. The penetration depth of protons into a sample is dependent on protons energy, as shown in Fig. 7.1 (a) for Si and Al targets. The irradiation regimes were simulated to create the δ-shape (when protons energy is kept constant) and triangle shape enhanced recombination regions (when protons energy is varied) within n-base of the diode. The profiles of the δ- and triangle shape enhanced recombination regions within diode base are sketched in Fig. 7.2. The simulated depth distribution of defects in *pin* diode structure, when protons energy is E_p=2.0 MeV, is presented in Fig. 7.1 (b).

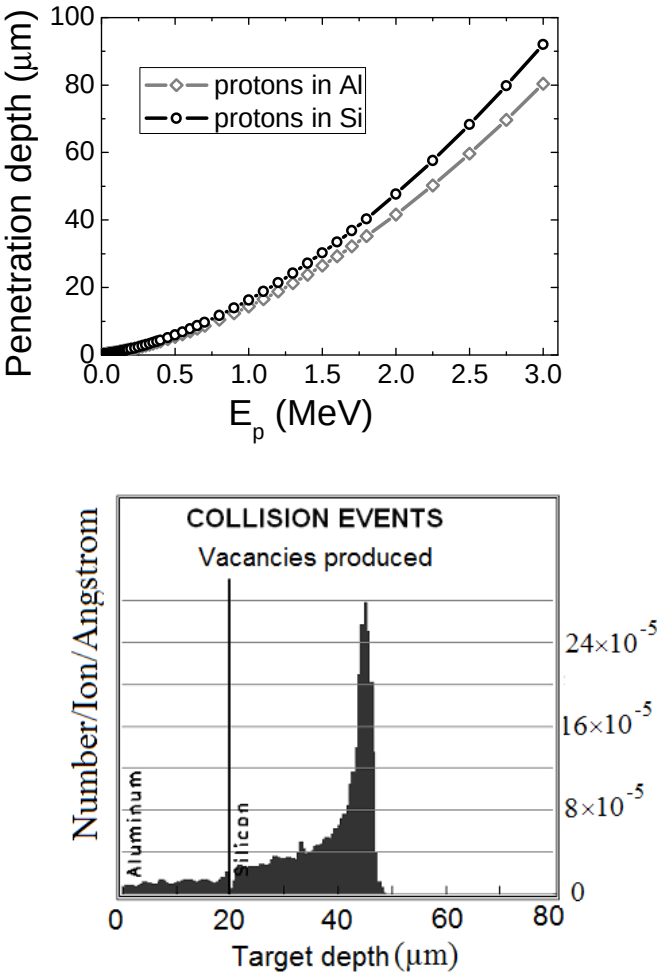

Fig. 7.1. a- Simulated penetration depth in Al and Si dependence on protons energy. b- Simulated depth distribution of defects in *pin* diode structure when protons energy E_p=2.0 MeV.

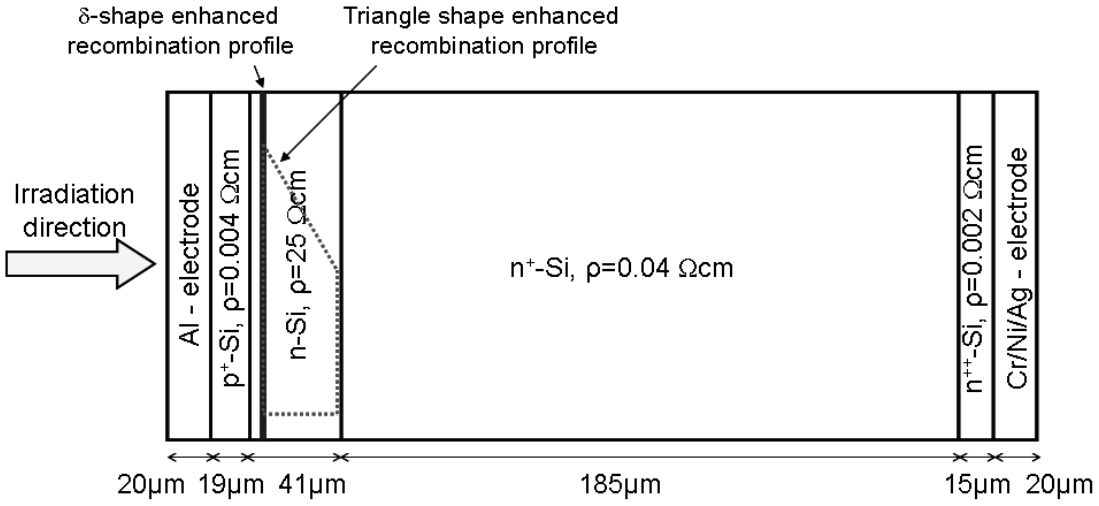

Fig. 7.2. Structure of diode with indicated δ- and triangle shape enhanced recombination regions.

The triangle shape enhanced recombination region is created by varying protons energy and fluence, as shown in Fig. 7.3. The irradiation is started with the highest energy (2.7 MeV) to create damage at the furthermost region of the base. Then, value of protons energy is decreased while the fluence is intentionally increased at the same time. Finally, the energy is decreased to 2.0 MeV which ensures damage nearby the p^+n junction.

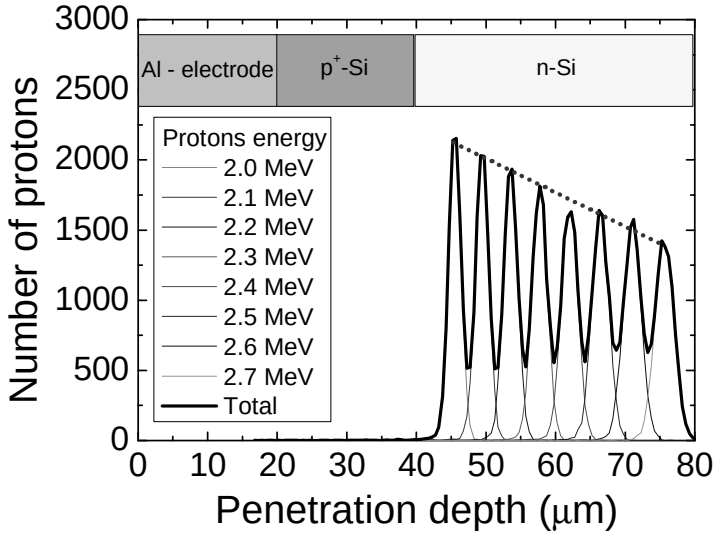

Fig. 7.3. Illustration of formation of triangle profile of enhanced recombination region within diodes base by varying protons energy in the range of 2.0–2.7 MeV.

The irradiation fluence strongly governs the carrier lifetime changes. The technically needed carrier lifetime value $\tau \approx 140$ ns determines the required irradiation fluence. Then, the necessary density of radiation defects is evaluated as:

$$N_{def} = \beta \cdot \Phi. \tag{7.1}$$

Here Φ is irradiation fluence, β - defects introduction rate which is commonly evaluated by analysis of recombination lifetime, leakage current, etc. parameters in samples after irradiation. In Si, the introduction rate is evaluated to be in the range of $\beta_p = 10^{-2} \div 1$ cm^{-1}. Carrier lifetime relation with defects density is expressed [44] as

$$\tau = \frac{1}{v_T \cdot \sigma_n \cdot N_{def}}. \quad (7.2)$$

Here, v_T is carrier thermal velocity, σ_n – carrier capture cross section. Using Eq. (7.2) the concentration of defects in Si is expressed as

$$N_{def} = \frac{1}{v_T \cdot \sigma_n \cdot \tau}. \quad (7.3)$$

Typical τ values, needed to modify the samples under design, are τ=140 ns, while other parameters are assumed to be v_T=10^7 cm/s, $\sigma_n \leq 10^{-14}$ cm^2. Then, density of the radiation induced defects should be

$$N_{def} = \frac{1}{v_T \cdot \sigma_n \cdot \tau} = 7.14 \cdot 10^{13} \text{ cm}^{-3}. \quad (7.4)$$

Assuming the defects introduction rate β_p =10^{-1} cm^{-1}, the irradiation fluence is evaluated to be:

$$\Phi = \frac{N_{def}}{\beta_p} = 7.14 \cdot 10^{14} \text{ cm}^{-2}. \quad (7.5)$$

Since defects introduction rate is not well defined in various conductivity materials when various species of defects are created, the samples were irradiated at various fluences to empirically choose the optimal irradiation regime. All irradiation regimes are listed in table 7.1 (for δ-shape enhanced recombination region) and in table 7.2 (for triangle-shape enhanced recombination region).

Table 7.1. Irradiation regimes when δ-shape enhanced recombination layer within diode base is formed.

Sample No.	**E_p, MeV**	**Φ, p/cm^{-2}**
1.	2.0	$7 \cdot 10^{12}$
2.	2.0	$7 \cdot 10^{13}$
3.	2.0	$7 \cdot 10^{14}$
4.	2.3	$7 \cdot 10^{13}$

Table 7.2. Irradiation regimes when triangle-shape enhanced recombination layer within diode base is formed.

	Sample 1	**Sample 2**	**Sample 3**	**Sample 4**
E_p, MeV	**$\Phi\times10^{11}$, p/cm^2**	**$\Phi\times10^{12}$, p/cm^2**	**$\Phi\times10^{13}$, p/cm^2**	**$\Phi\times10^{13}$, p/cm^2**
2.7	5	1	1	2
2.6	5	1	1	2
2.5	8	1.5	1.5	3
2.4	10	2	2	4
2.3	10	2.1	2.1	4.2
2.2	12	2.4	2.4	4.8
2.1	13	2.6	2.6	5.2
2.0	15	3	3	6
Total	**80**	**15.6**	**15.6**	**31.2**

7.2. Modelling of static and dynamic parameters of the irradiated diodes

The reverse recovery process is determined by the removal of the minority carriers from diode drift region during switching from the forward conduction to reverse blocking mode. The typical and linearly approximated reverse recovery current transients and carrier distribution at different time instants during recovery process are presented in Figs. 7.4 (a) and (b), respectively.

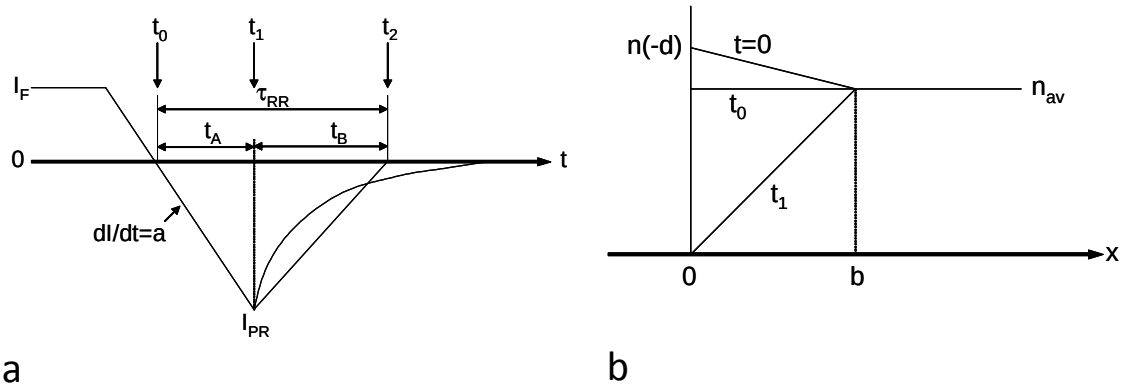

a b

Fig. 7.4. Typical linearly approximated reverse recovery current waveforms (a) and change of carrier distribution during reverse recovery (b).

To reach the soft reverse recovery current transient, which is described by the ratio of durations of (t_B) and (t_A) within reverse recovery transient, the recombination level position within drift region and carrier lifetime should be optimized. The softness parameter *S* is expressed as [7]:

$$S = \frac{t_B}{t_A} = \left(\frac{4d}{b} - 1 \right) = \frac{\tau_{rr} - \frac{b}{2} \frac{\tau_{HL}}{d} \frac{I_F}{I_{PR}}}{\frac{b}{2} \frac{\tau_{HL}}{d} \frac{I_F}{I_{PR}}}. \quad (7.6)$$

Here used quantities are expressed as:

$$b = \frac{2qD_n \lfloor n_j - n_{av} \rfloor}{I_F}; \quad (7.7)$$

$$I_{PR} = 2qD_n \frac{n_{av}}{b}; \quad (7.8)$$

$$I_{PR} = \frac{\tau_{HL} D_n}{bd} I_F; \quad (7.9)$$

$$\tau_{RR} = 2\tau_{HL} \frac{I_F}{I_{PR}} = \frac{2bd}{D_n}. \quad (7.10)$$

Here, additional symbols are as follows: $2d$ is geometrical width of drift region, b is the range where the injected minority carrier density reaches the average value n_{av} (presented in Fig. 7.4 (b)), D_n is the diffusion coefficient of the majority carriers, τ_{HL} – carrier lifetime at high injection level, μ_n and μ_p – electron and hole mobilities, respectively. The above expressions enable to relate the reverse recovery duration τ_{RR}, reverse current peak I_{PR} value at certain forward current I_F determined by external current generator.

It can be seen that the peak reverse recovery current can be reduced by decreasing the τ_{HL} lifetime in the middle of the drift region. The shorter reverse recovery time can be achieved by reducing the τ_{HL} lifetime and by increasing the peak reverse current. Assuming that parameter b can be varied by lifetime local killing techniques when b coincides with the enhanced recombination layer, the optimization of parameters can be reached by a trade–off. If the enhanced recombination layer is positioned nearby the metallurgic junction, then S and I_{RP} acquire the largest values, while τ_{RR} leads to the shortest RRT process. If the layer of enhanced recombination is shifted away from the junction, then S and I_{RP} decreases and τ_{RR} increases. Homogeneous or triangle shape (with shortest recombination lifetime nearby the p^+n junction and largest at the end of base region) of induced enhanced recombination layer would

result in fastest switching rates and lowest I_{RR}. However, it is necessary to evaluate the forward voltage drop U_F dependent on recombination lifetime profile and its position within the diode base region.

Forward voltage drop U_F within diode base region is evaluated by integrating the electric field [7] determined by drift and diffusion current components as

$$E_B(x) = \frac{I_F}{q_e(\mu_n + \mu_p)\Delta p(x)} - \frac{k_B T}{2q_e \Delta p(x)} \frac{d\Delta p(x)}{dx}. \qquad (7.11)$$

Here $\Delta p(x)=\Delta p_n \exp(-\tau_{tr}/\tau_R(x))\times\exp(-x/L_p)$ is the excess carrier $\Delta p_n = p_{0n}\exp(q_e U_{pn}/k_B T)$ distribution within n-base region, U_{pn} – voltage drop on p^+n junction due to carrier injection. Then, the forward voltage drop on junction and on base region $U_F=U_B+U_{pn}$ for a diode with homogeneous defect distribution profile is expressed as

$$U_{F,\mathrm{hom}} = \frac{I_F}{q_e\left(\mu_n + \mu_p\right)\Delta p_n \exp\left(\frac{\tau_{tr}}{\tau_R}\right)} L_p\left(\exp\left(\frac{d}{L_p}\right) - 1\right) + \frac{k_B T}{2q_e}\left(\frac{d}{L_p} + \frac{\tau_{tr}}{\tau_R}\right) + U_{pn}. \qquad (7.12)$$

Forward voltage drop in diode with δ-profile of enhanced recombination layer is expressed by separate analysis of current components for the diode base separate regions with appropriate τ_R and L_p parameters as shown in Fig. 7.5 (a).

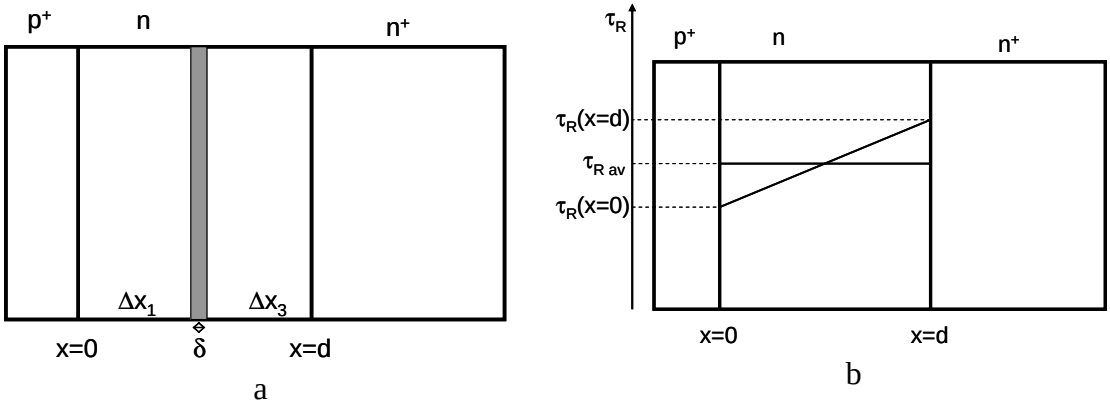

Fig. 7.5. Sketch of diode structure with position of δ-damage layer (a) and variation of recombination lifetime diode with triangle enhanced recombination profile (b).

Taking the boundary conditions for excess carrier distribution as

$$\Delta p\,|_{x=0} = \Delta p_n$$

$$\Delta p\,|_{x=\Delta x1} = \Delta p_n\,|_{x=0}\,\exp\left(\frac{-\Delta x_1}{L_{p1}}\right)\exp\left(\frac{-\tau_{tr}}{\tau_{R1}}\right)$$

$$\Delta p\,|_{x=\Delta x1+\delta} = \Delta p_n\,|_{x=\Delta x1}\,\exp\left(\frac{-\delta}{L_{p2}}\right)\exp\left(\frac{-\tau_{tr}}{\tau_{R2}}\right), \qquad (7.13)$$

$$\Delta p\,|_{x=d} = \Delta p_n\,|_{x=\Delta x1+\delta}\,\exp\left(\frac{-\Delta x_3}{L_{p3}}\right)\exp\left(\frac{-\tau_{tr}}{\tau_{R3}}\right)$$

the forward voltage drop for a diode with δ-shape defects distribution profile is expressed:

$$U_{F,\delta} = \frac{I_F}{q_e(\mu_n+\mu_p)}\left[\frac{L_{p1}\left(\exp\left(\frac{\Delta x_1}{L_{p1}}\right)-1\right)}{\Delta p_n\,|_{x=0}\,\exp\left(\frac{-\tau_{tr}}{\tau_{R1}}\right)} + \frac{L_{p2}\left(\exp\left(\frac{\Delta x_1+\delta}{L_{p2}}\right)-\exp\left(\frac{\Delta x_1}{L_{p2}}\right)\right)}{\Delta p_n\,|_{x=\Delta x1}\,\exp\left(\frac{-\tau_{tr}}{\tau_{R2}}\right)} + \frac{L_{p3}\left(\exp\left(\frac{d}{L_{p3}}\right)-\exp\left(\frac{\Delta x_1+\delta}{L_{p3}}\right)\right)}{\Delta p_n\,|_{x=\Delta x1+\delta}\,\exp\left(\frac{-\tau_{tr}}{\tau_{R3}}\right)}\right] +$$

$$\frac{k_B T}{2q_e}\left[\frac{\Delta x_1}{L_{p1}} + \frac{\delta}{L_{p2}} + \frac{\Delta x_3}{L_{p3}} + \tau_{tr}\left(\frac{1}{\tau_{R1}}+\frac{1}{\tau_{R2}}+\frac{1}{\tau_{R3}}\right)\right] + U_{pn} \qquad (7.14)$$

For a diode containing a triangle defects distribution profile, $U_{F,\wedge}$ can be evaluated using (7.12) expression after inserting the average recombination lifetime value $\tau_{R\,av} = \tau_R(x=0)/\tau_R(x=d)$ instead of τ_R, as sketched in Fig. (7.5 (b)). The simulated variations of U_F and its components as a function of τ_R are presented in Fig. 7.6 (a) for homogeneous distribution of recombination lifetime within 40 μm base region at forward current density of 100 A/cm^2 and at correspondent injection conditions. Variations of U_F are compared for a homogeneous, triangle and δ-shape enhanced recombination profiles within base region in Fig. 7.6 (b).

Simulations were performed assuming that recombination lifetime nearby the p^+n junction $\tau_R(x=0)$ is the shortest and its value increases linearly going to the end of the base region and reaches the largest value equal $\tau_R(x=d)=1.5\,\tau_R$ for a triangle recombination profile. For a δ-shape recombination profile it was assumed that it is positioned in the middle of the base region with recombination lifetime τ_R and width of 3 μm and with lifetime

of $7\tau_R$ within pedestal between the p^+n junction and the δ- layer. It can be seen that the lowest U_F values are achieved when δ-shape recombination profile is produced while the largest values are within homogeneously damaged base region.

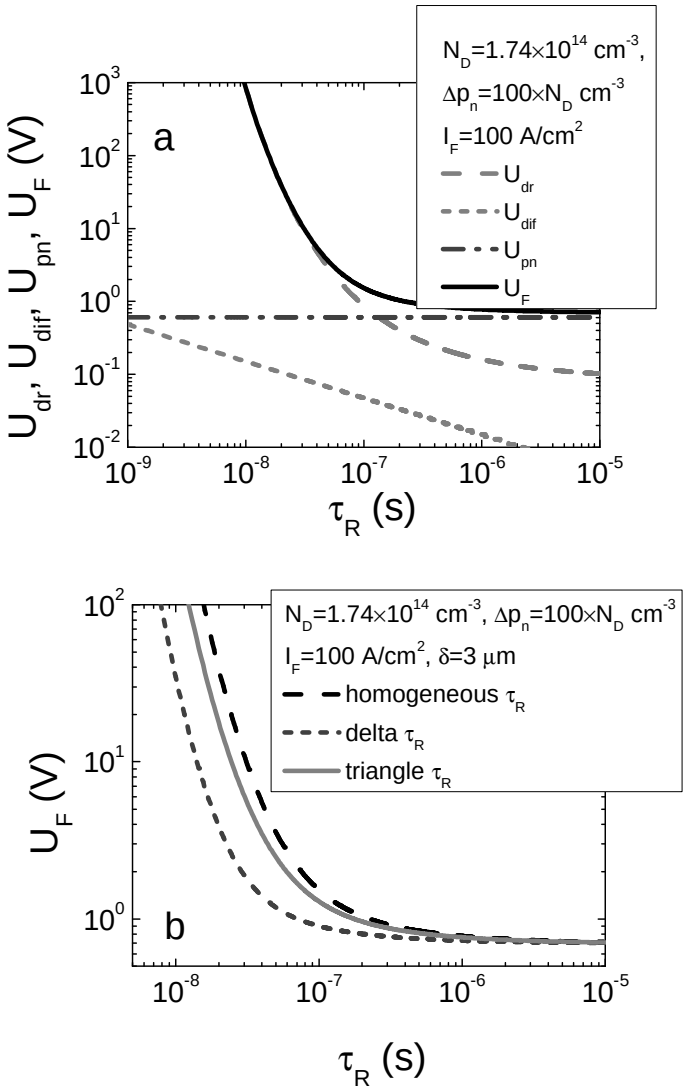

Fig. 7.6. Forward voltage drop, composed of diffusion, drift and p^+n junction voltage drop components (a) and comparison U_F with homogeneous, triangle and δ-shape defects distribution profiles (b) as a function or recombination lifetime.

Variations of U_F with positioning of δ-shape defects layer of width of 3 μm within base region are presented in Fig. 7.7 for various τ_R values. It can be noticed, that U_F increases with reduction of τ_R and with shifting the δ-shape layer away from the metallurgic p^+n junction due to the increase of width of

region with the lower recombination lifetime pedestal (relatively to that of the non-irradiated region behind the δ- layer).

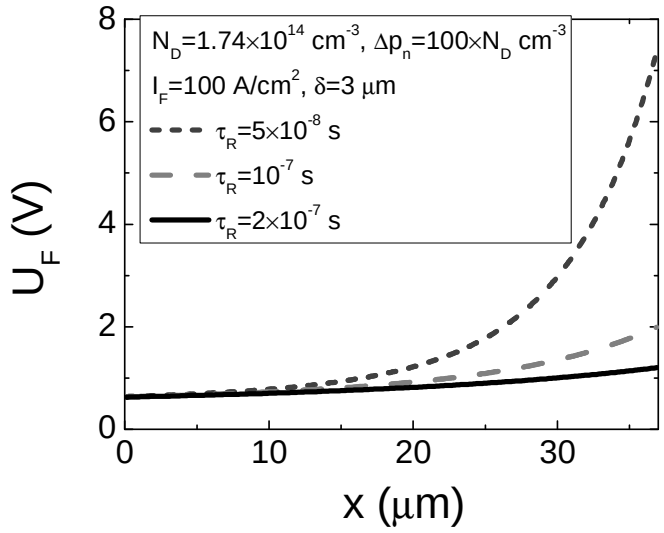

Fig. 7.7. Simulated forward voltage drop variations with positioning of δ-shape recombination layer for τ_R values of 50, 100 and 200 ns.

Therefore local lifetime modification should be engineered by varying the position, profile or creating multiple layers within structure to reach trade-off between the static (U_F) and dynamic (τ_{RR}) parameters of a device.

7.3. Experimental diode parameters after irradiation

7.3.1. Variations of carrier lifetime parameters after irradiation

Carrier recombination lifetime variations with fluence measured by microwave probed photoconductivity technique (MW-PCT) in 2.0 MeV protons irradiated Si wafer samples are presented in Fig. 7.8. The latter lifetimes are compared with those obtained in FZ n-Si samples of the same thickness diodes irradiated with penetrative protons of 50 MeV – 24 GeV energies. It can be noticed that lifetime values in FZ n-Si wafers irradiated with 2.0 MeV protons are significantly reduced relatively to that before irradiation ($\tau_{R,\ non\text{-}irrad}$=60 μs) and decreases almost linearly from tenths of nanoseconds to 1 ns by varying of protons fluence in the range of 7×10^{12}-4×10^{14} p/cm^2. Moreover, recombination lifetime values in 2.0 MeV protons irradiated FZ n-Si wafers are considerably shorter than those obtained in samples irradiated

with penetrative protons and neutrons [70] of the same fluence. This result proves that radiation damage is more efficient within a stopping range of protons than that achieved under irradiation with penetrative hadrons.

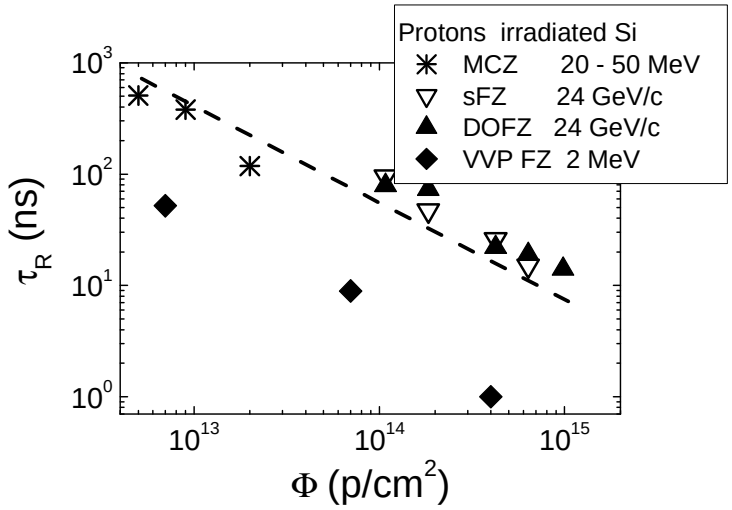

Fig. 7.8. Carrier recombination lifetime as a function of fluence measured in 2.0 MeV protons irradiated Si wafer samples and compared with those obtained in samples of various thickness irradiated by penetrative protons of various energies.

Fluence dependent variations of deep level spectra (normalized to the most intensive peak amplitude) obtained in protons irradiated *pin* diode structures with δ- and triangle-shape of enhanced recombination profiles are presented in Fig. 7.9 (a) and (b), respectively.

In order to separate the overlapping of carrier emission peaks within DLTS spectra, as well as to avoid seeming their shift due to emerging additional traps under increased radiation damage with fluence or defect transforms due to heat treatments, within intricate spectrum, it should be simulated by Gauss function. Such a peak separation procedure is illustrated in Fig. 7.10 for the diode irradiated with 2.0 MeV protons at fluence of 10^{13} cm^{-2}.

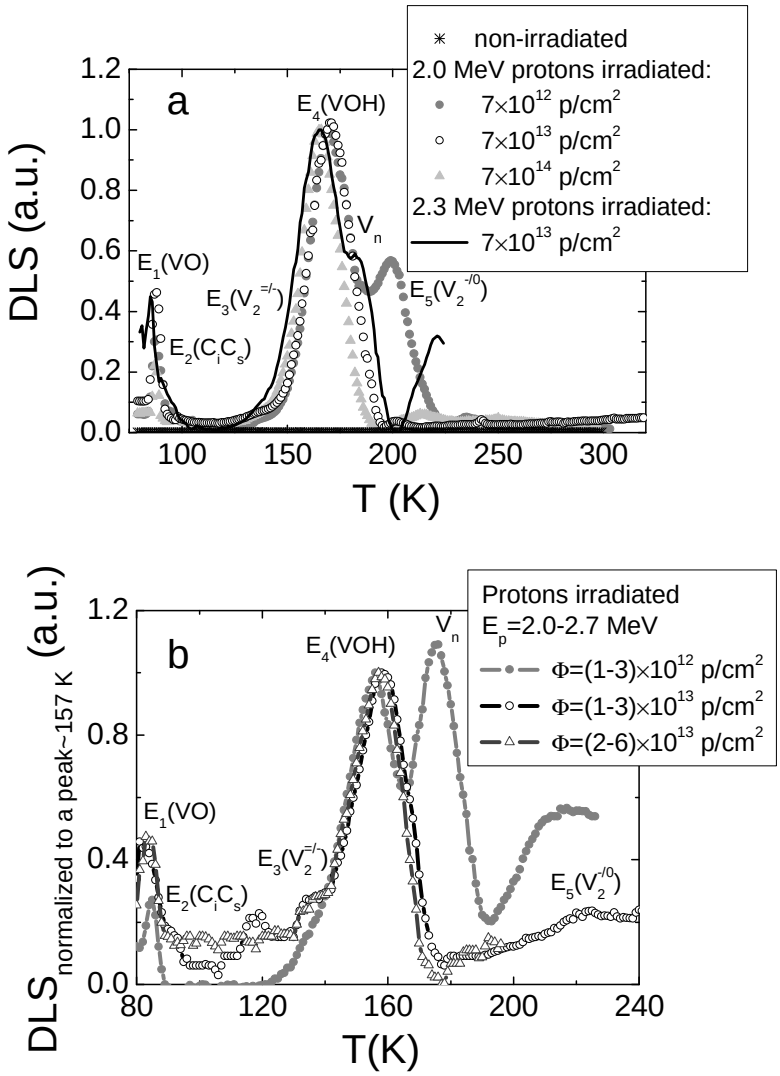

Fig. 7.9. Fluence dependent variations of normalized deep level spectra measured in diode samples containing δ(a) and triangle (b) shape enhanced recombination layers.

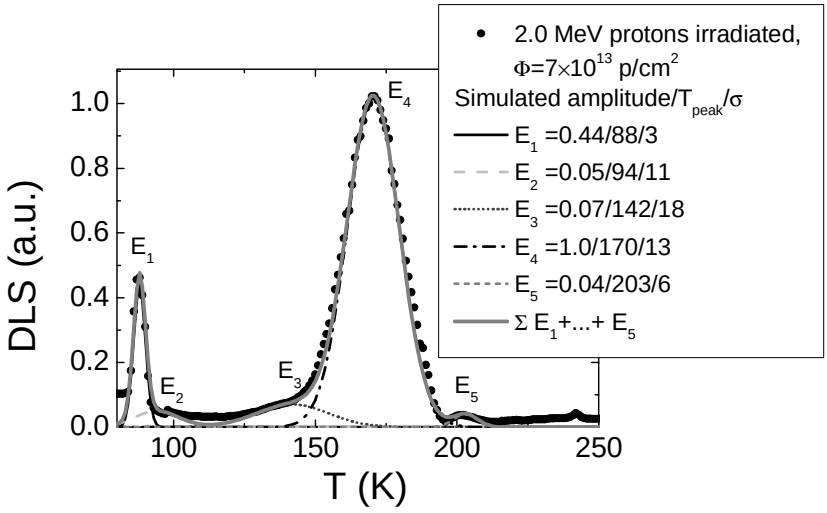

Fig. 7.10. Simulated DLTS spectrum peaks by using a Gauss function for a diode irradiated by 2.0 MeV protons of fluence of Φ=7×10^{13} cm^{-2}.

Five main DLTS peaks within temperature ranges of 88-90 K, 90-110 K, 130-150 K, 150-170 K, and 200-220 K, have been obtained at the same lock-in filtering and for carrier injection parameters in the as irradiated samples containing the δ- and triangle-shaped enhanced recombination profiles. The dominant DLTS peaks are commonly ascribed to a vacancy-oxygen (VO) complex (E_1 peak), to a carbon interstitial-substitutional atoms complex (E_2 peak), to a di-vacancy of different charged states (E_3 and E_5 peaks for $V_2^{=/-}$ and $V_2^{-/0}$, respectively), and to a vacancy-oxygen-hydrogen (VOH) complex (E_4 peak). Non-penetrating protons create efficiently the defects within stopping range due to the large interaction cross-section. High density of implanted hydrogen H^+ is a reason for intense generation of the VOH complexes within stopping range [17, 18]. Therefore, the latter E_4 peak observed at 170 K prevails with enhancement of fluence in 2.0 MeV protons irradiated diodes containing the enhanced recombination layer nearby the p^+n junction. For 2.3 MeV protons irradiated diode, containing an enhanced recombination layer at a half-width of the base region, a reduction of a peak E_4 is observed relatively to the di-vacancy ascribed peaks E_3 and E_5. This result implies that a depth integrated DLTS signal exposes an enhanced role of the irradiated pedestal of defects, relatively to a narrow δ-shape layer. The pedestal prevails in the DLTS spectrum measured for the as-irradiated diode by 2.0 MeV protons. Furthermore, a peak in the temperature range of 160-200 K is observed to be overlapped with additional component within the higher temperature wing which is debated [71, 72] as a trap associated with vacancy clusters (V_n). In diodes containing a triangle defects distribution profile, the overlapping multi-δ-shape layers are formed by gradual step-like change of protons energy and fluence. In diode irradiated with lowest protons fluence two DLTS peaks (ascribed to VOH complexes and vacancy clusters V_n) observed in the temperature range of 150-180 K compete, as can be seen in Fig. 7.9 (b). For the higher fluences irradiated diode, a peak E_4 starts to be dominating relatively to a peak associated with V_n clusters. This might be explained by a more

intensive production of VOH complexes (due to a higher density of hydrogen H^+) instead of V_n clusters.

7.3.2. Variations of static and dynamic characteristics

Reverse recovery time variations dependent on forward current in diodes, containing a δ-shape radiation induced layer and a triangle-shape profile of enhanced recombination region in diode base, are compared in Fig. 7.11 (a).

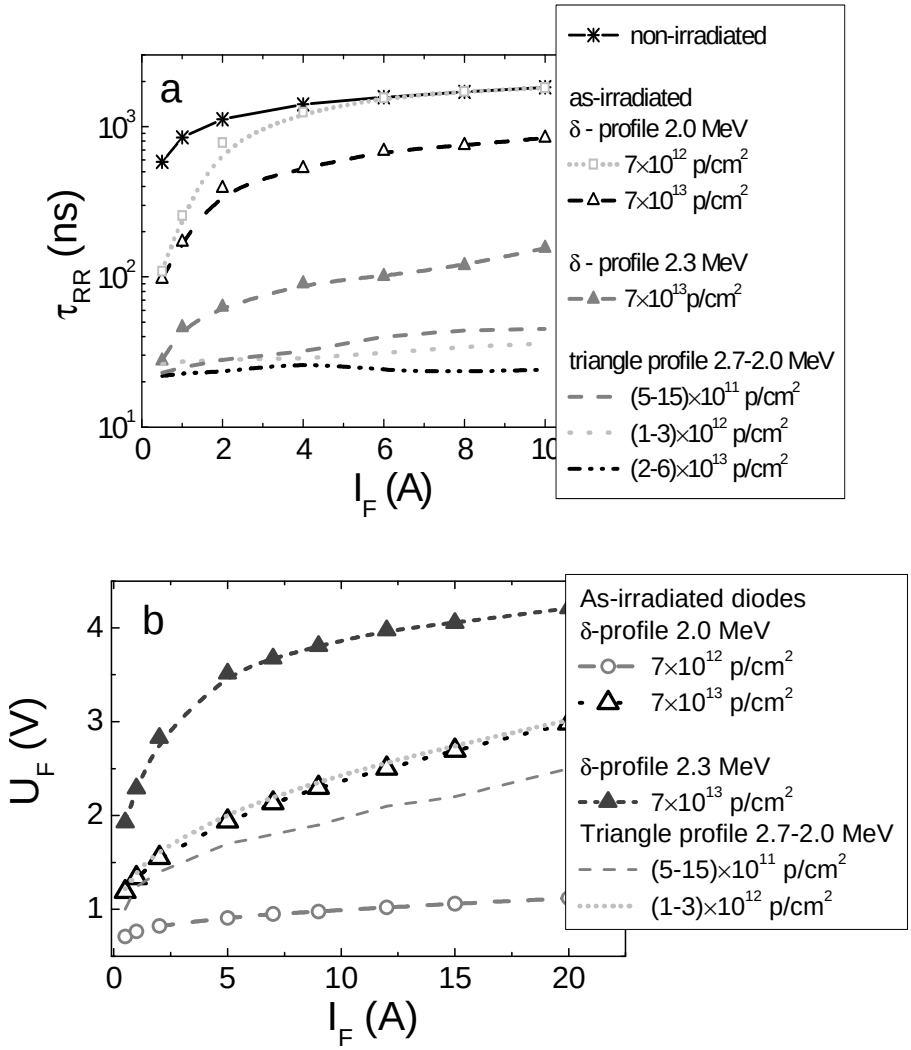

Fig 7.11. Reverse recovery time (a) and forward voltage drop (b) as a function of the forward current in diodes with δ–shape and triangle profiles of radiation defects distribution.

Value of the forward current I_F in diode represents the density of excess carriers $\Delta p_n = I_F/(q_e(\mu_e+\mu_p)E)$ (here μ_e and μ_p – electron and hole mobilities,

respectively and E – the electric field within drift region during forward conduction mode) which should be extracted during switchover process, in this case.

Reverse recovery time τ_{RR} strongly depends on the layer profile and on location of the layer containing deep recombination centres. Values of τ_{RR} are decreased after using all the employed irradiation regimes relatively to the non-irradiated diodes, as shown in Fig. 7.11 (a). In the diodes containing a δ-shape 2.0 MeV proton radiation-induced layer, the dominant recombination centres determine an increase of recombination lifetime with excitation level ($\sim I_F$). These deep centres do not govern the short high level carrier recombination lifetime τ_{HL} or their density is too low. Enhancement of irradiation fluence (of 2.0 MeV protons) reduces τ_{HL} and consequently, the τ_{RR} at large I_Fs. A shift of the δ-shape layer (induced by the same protons fluence) towards the half-width of the diode base by the increased 2.3 MeV energy of protons accelerates the rate of diode recovery by reducing the absolute value of τ_{RR}, as can be deduced from the comparison of respective τ_{RR}–I_F dependences in Fig. 7.11 (a). This might be caused by an enhancement of the density of VO complexes (which reduce τ_{HL}) in diode containing a δ-shape defects distribution profile in the middle of the base region, relatively to that localized nearby the junction. Moreover, the excess carriers recombine immediately after switching the diode from on-state to the blocking regime when the δ-shape defects layer is positioned in the middle of the base region, with no need do diffuse (which increases τ_{RR}) towards the recombination layer (before recombining) when it is localized nearby the junction. Formation of a triangle profile of radiation-induced recombination centres significantly reduces the τ_{RR} values that are obtained to be the shortest ones, relatively to those obtained in diodes containing a δ-shape defects distribution profile, and are nearly invariable with I_F. Physical reasons of the discussed variations of τ_{RR} can be the competition of the point-like and the cluster-type radiation defects [A8] and caused by their

distribution within entire base region, that ensure a rapid recombination after the diode is switched into the blocking regime.

However, due to radiation induced defects, the forward voltage drop U_F increases with irradiation fluence for all the formed defect profiles and their locations (Fig. 7.11 (b)). The largest values of U_F are obtained for heavily irradiated δ-shape layer located at the half-width of diode base. This can be explained by the increased integral resistivity of the base material over its length and by the serial redistribution of forward voltage drops on junction and on elevated resistivity base, when the efficiency of carrier injection is significantly reduced. Location of a vertex of triangle profile of induced layer nearby the metallurgical junction concentrates the applied field at junction, but the enhancement of defects density over the whole width of diode base increases the integral resistivity of the base material, and, consequently, the value of U_F appears to be elevated.

The effect of protons induced defects to leakage current can be easily resolved by measuring the I-V characteristics, as illustrated in Fig. 7.12 for diodes irradiated by various protons fluences and energies. An almost linear increase of a leakage current is clearly observed with enhancement of fluence measured in 2.0 MeV protons irradiated diodes (Fig. 7.12 (a)), that is explained by an increase of radiation induced generation centres.

A steep increase of a leakage current has been found at elevated reverse voltages, those values exceed a threshold of >50 V in diodes irradiated by protons of fluence $>7\times10^{13}$ p/cm^2 (Fig. 7.12 (a), grey dotted curve). A threshold value of the reverse voltage for detection of this component of the steep leakage current increase is reduced with an enhancement of irradiation fluence (Fig. 7.12 (a), light grey dash-dotted curve). This peculiarity might be cursorily explained as a manifestation of the Poole–Frenkel effect due to emission of carriers from the deep levels at a sufficient electric field due to reduction of a potential barrier at a local trap. Due to an increase of resistivity of the locally radiation damaged material area, a local enhancement of the strength of the electric field is very probable when a depth distribution of a

voltage drop exists within very narrow (few microns) diode base region. Then the threshold reverse voltage value (for the steep leakage current increase) is reduced if the increment of resistivity is proportional to the irradiation fluence. Alternatively, the steep leakage current increase can be understood by involving the current percolation effects for a damaged range of a diode base. It is well known that large values of an interaction cross-section in Si for 2–3 MeV protons is a reason for rather short penetration depth of these particles and for creation of a high density of cluster defects within a stopping range of 2–3 MeV protons. The existence of sharply inhomogeneous distribution of density of these cluster defects, with a rather flat pedestal within the proton penetration path and a δ-shape peak density at proton stopping length, acts as extended defects with the local-field-governed space charge regions surrounding the cluster cores. Then, the applied voltage drop distributes among the space-charge areas of clusters, while the conductivity current can be ascribed to areas free of clusters, those contain only point defects. It is the latter component that determines the magnitude of a percolative current flowing along the random paths of the non-damaged material. A cross-sectional area of these channels of a relatively non-damaged material depends on density of clusters and on applied external voltage which modifies the extent of space-charge regions surrounding the clusters. The parallel and serial linkage of components of inhomogeneously damaged areas determines the total leakage current. Thus, an increase of cluster density within a pedestal component of the damage depth distribution can be a reason for reduction of a threshold voltage to observe the steep leakage current increase if applied voltage enhances an integral diameter of percolation channels.

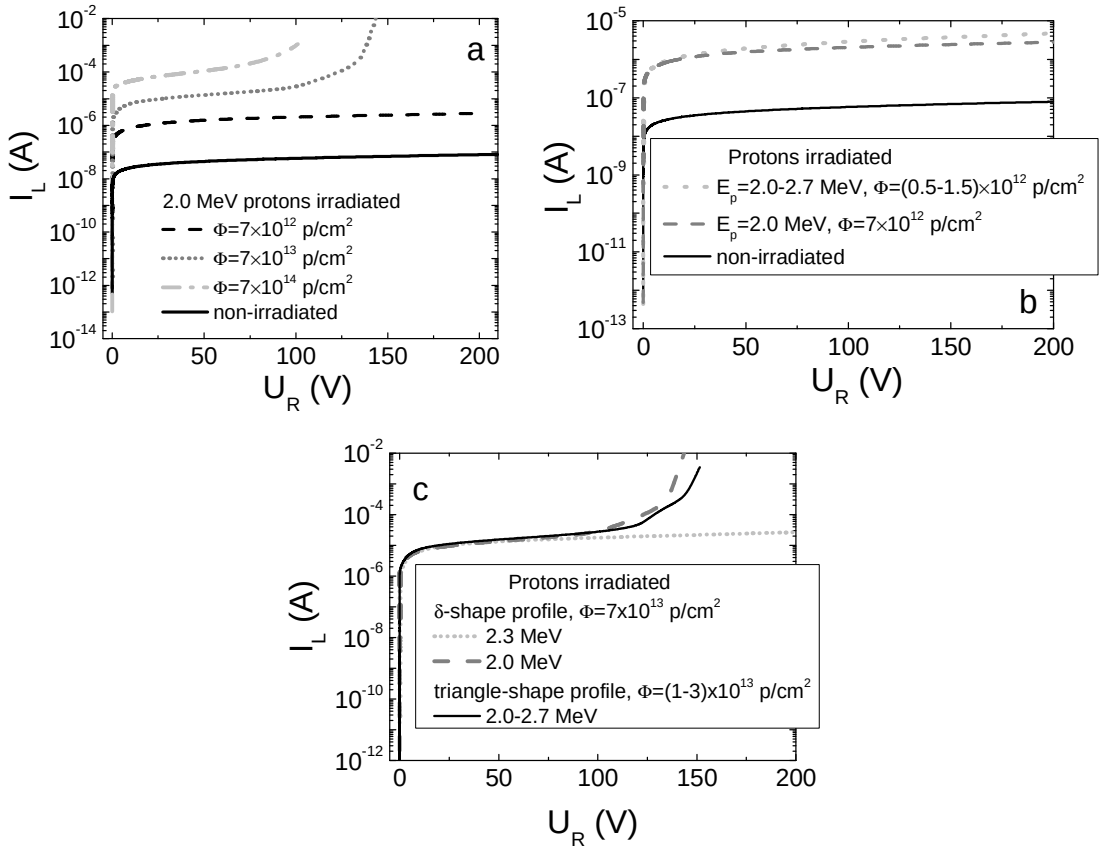

Fig. 7.12. (a) I-V characteristics in diodes irradiated by 2.0 MeV protons of different fluences, (b) comparison of I-V characteristics measured in non-irradiated diode and in diodes containing radiation induced δ (nearby the metallurgic junction) and triangle shape defects profiles irradiated by close fluences of protons. (c) comparison of I-V characteristics measured in diodes containing radiation induced δ (nearby the metallurgic junction and in the middle of the base region) and triangle shape defects profiles irradiated by close fluences of protons.

The I-V characteristics measured on diodes containing different defect distribution profiles formed by proton beam either of fixed (2.0 MeV) energy or of multi-step gradually varied energy in the range of 2.7–2.0 MeV are compared in Fig. 7.12 (b) for reverse biasing branches of the I–V dependences. Here, I–V characteristics obtained for the smallest irradiation fluences employed in this work are presented. Also, these fluences are of nearly the same peak value for δ- and triangle-shape defects distribution profiles. The increase for leakage current is obtained in the irradiated diodes when comparing with that for a non-irradiated material diode. A rather smooth variation of the I–V curves in the typical I–V saturation regions indicates the prevailing of the point defects. The impact of the same deep levels can be

implied, when their action as generation/trapping centres is inherent. These generation centres increase the leakage current.

However, the discussed segment of the steep increase of a leakage current inevitably appears for the elevated reverse voltages in diodes irradiated by higher proton fluences. The threshold reverse voltage value, for which the steep increase of a leakage current is detectable, depends on irradiation fluence, on defect distribution profile, and on location of a damaged layer relatively to a metallurgical junction, as illustrated in Fig. 7.12 (c). The segment of the steep increase of a leakage current starts at a threshold reverse voltage value which is the smaller the larger irradiation fluence (Fig. 7.12 (a)) or a closer location of the damaged layer relatively to junction (Fig. 7.12 (c)) is. A reduction of the threshold reverse voltage with a closer location of a peak of the damaged layer to metallurgical junction implies that the impact of the extended radiation defects, containing space-charge surroundings, exceeds that of the generation centres in the increase of leakage current dependently on the local strength of electric field. The latter is weaker in the middle of a diode base relatively to that at junction. Therefore, for the same radiation induced defects profiles formed by 2.0 and 2.3 MeV protons, the observed threshold reverse voltages differ significantly, when comparing the respective I–V's in Fig. 7.12 (c) for a layer, located at junction, and for a layer within the half-width of a diode base. With enhancing the cluster density when the latter is proportional to irradiation fluence, the cluster-surrounding space-charge spheres tend to overlap. Consequently, an external applied field governs the percolation current or the local field. Direction of local fields is dependent on the polarity of space charge and is caused by the cluster core structure in the space-charge it surrounds. Then, a leakage current increase is typical either to that of a forward biased junction or to avalanche processes evolved within a local strong field.

Thus, the improvement of dynamic (τ_{RR}) and static (U_F, I_L) parameters of the *pin* switchers can be reached only as a trade-off among technological procedures. Therefore, isochronous 24 h annealing in the temperature range of

80–400 ^{o}C have been performed in order to reduce the forward voltage drop and the leakage current.

7.4. Diode parameters after isochronal anneals

To reduce an increased leakage current and forward voltage drop, which is obtained after irradiations, the isochronal 24 h anneal procedures were carried out for Si wafer and diode samples. Carrier recombination/generation and static as well as dynamic parameters of diodes were examined after each annealing step.

7.4.1. Anneal induced variations of carrier lifetimes

Carrier recombination lifetime variations measured by MW-PCT technique after isochronal 24 h anneal steps at various temperatures are presented in Fig. 7.13. The higher increase of recombination lifetime with anneal temperature is observed in samples irradiated with higher fluences while in the lowest fluence irradiated samples carrier lifetime is obtained to be almost invariable.

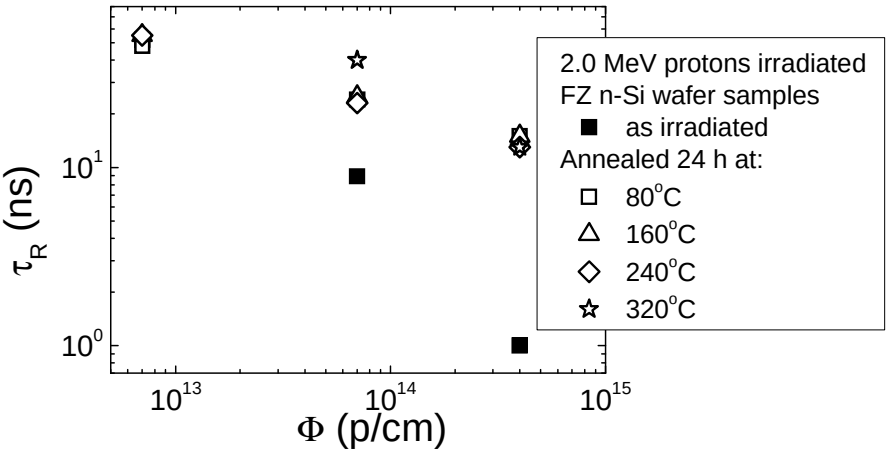

Fig. 7.13. Comparison of fluence dependent recombination lifetime variations after various steps of isochronal anneal procedures, obtained in FZ n-Si wafer samples.

Variations of the DLTS spectra, of peak amplitude values and of relative capture cross-section values as a function of 24 hour isochronal anneal temperature are presented in Fig. 7.14 and Fig. 7.15 for diodes containing δ-profile of radiation induced defects nearby the junction and in the middle of the

base region, respectively, and in Fig. 7.16 for a diode containing triangle profile of radiation induced defects. A seeming shift of peaks appears after each heating step in both irradiation profiles containing diodes. Actually, these shifts are determined by variation of different overlapping peaks.

In diode with a δ-shape recombination layer localized nearby the junction, the most significant changes are observed at the E_4 peak, associated with VOH complexes (Fig. 7.14).

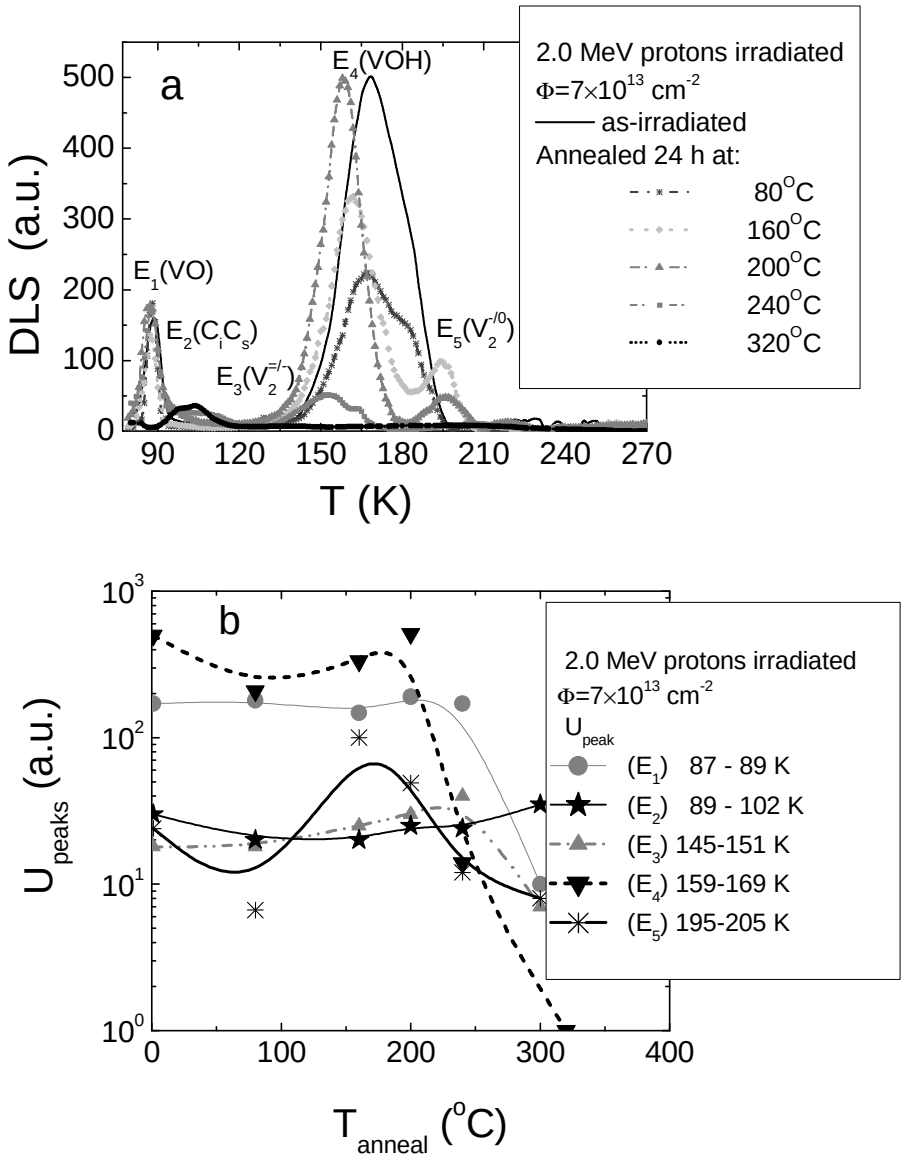

Fig. 7.14. Variation of the DLTS spectra (a) and of peak amplitude (b) values measured on diode containing radiation induced δ-shape profile of defects distribution nearby the junction after various steps of 24 h isochronal anneal.

Density of the VOH complexes, detected as variations of E_4 peak amplitude, behaves non-monotonically. The E_4 peak amplitude decreases after annealing step at 80^{o}C and overlaps with additional peak located at higher scanning temperature wing which might be associated with V_n clusters. Transform of the VOH centre to a component VO may be responsible for the changes of E_1. At the same time the peak E_5, ascribed to $V_2^{-/0}$, decreases as well. Further enhancement of temperature ($T \geq 160^oC$) leads to a complete disappearance of V_n clusters, which is a product for VOH and $V_2^{-/0}$ defects. At the highest anneal temperatures (>240^{o}C), the VO, VOH and divacancy related traps ($V_2^{=/-}$ and $V_2^{-/0}$) anneal out, as deduced from the reduction of the peak amplitudes within DLTS spectrum. Meanwhile, complexes of carbon interstitial and substitutional atoms C_iC_s are formed, as observed from an increase of E_2 peak amplitude.

In diode with a (-shape layer localized in the middle of the base region, the E4 peak and consequently the density of VOH complexes decreases with enhancement of anneal temperature and these peaks completely vanishes at temperatures $T \geq 160\ ^oC$ (Fig. 7.15).

The VOH decay is accompanied by formation of divacancies via Vn. After anneal at the highest temperatures, the CiCs complexes dominate.

Qualitatively similar picture of the heat treatment-induced transforms of the DLTS spectra has been also observed for diodes containing a triangle profile of defect distribution. Here, a slight difference relatively to the diodes, containing the (-shape layer, can be revealed within a wing of the elevated scan temperatures in DLTS spectra (Fig. 7.16).

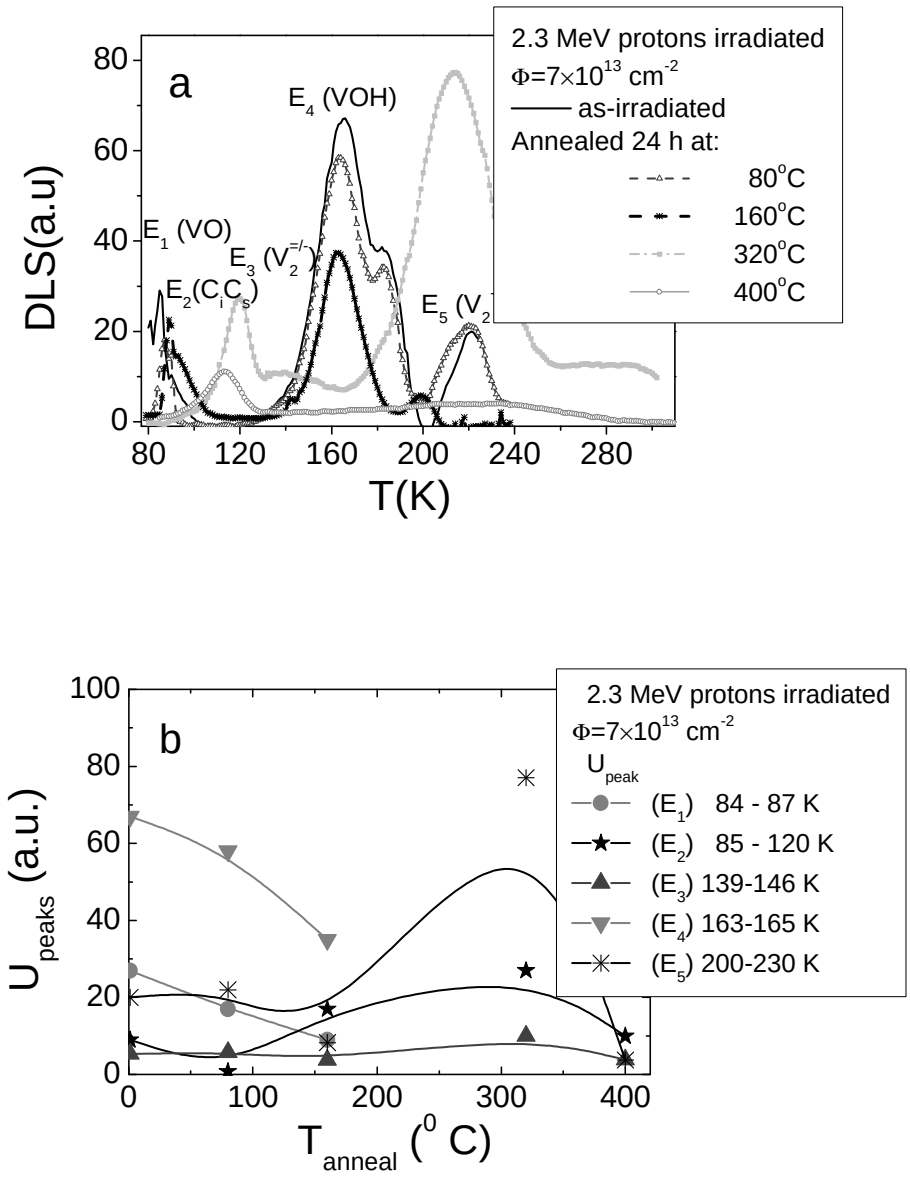

Fig. 7.15. Variation of the DLTS spectra (a) and of peak amplitude (b) values measured on diode containing radiation induced δ–shape profile of defects distribution in the middle of the base region after various steps of 24 h isochronal anneal.

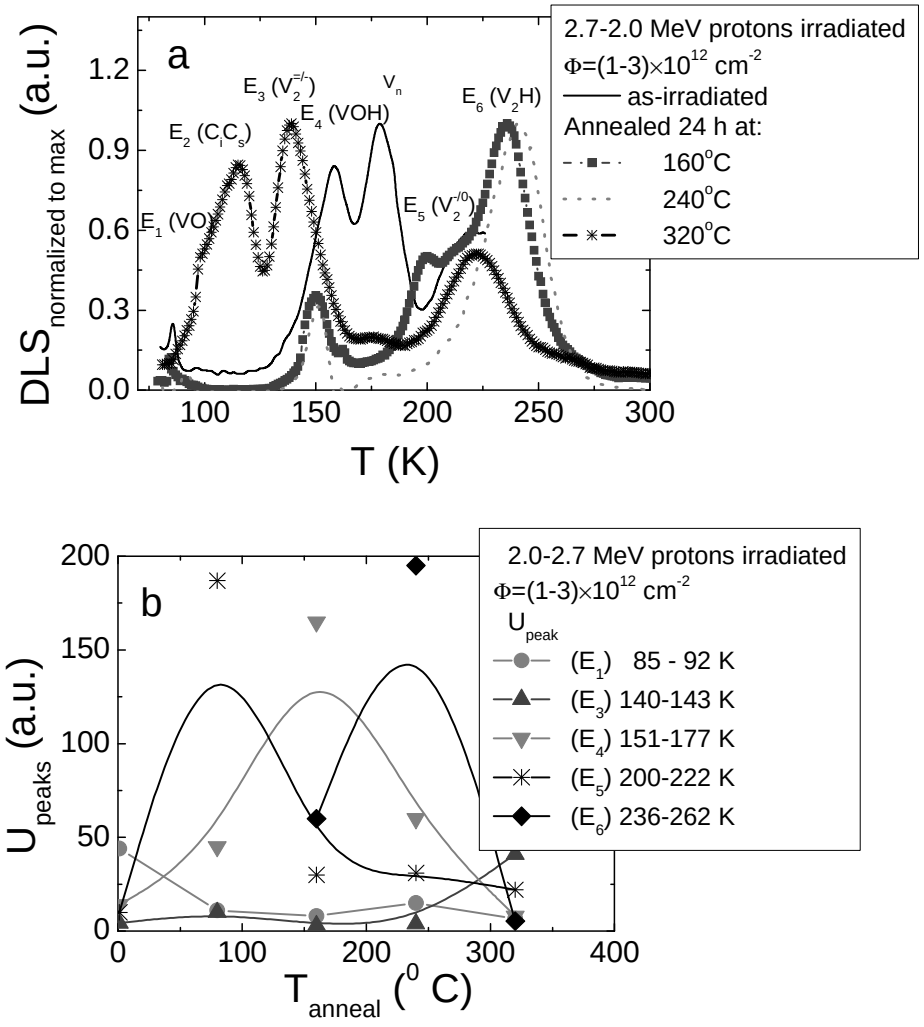

Fig. 7.16. Variation of the DLTS spectra (a) and of peak amplitude (b) values measured on diode containing radiation induced triangle profile of defects distribution within base region after various steps of 24 h isochronal anneal.

An additional hydrogen related complex (E_6) can be resolved via annealing dependent variations of an amplitude of DLTS signal within a range of the E_5 peak. An origin of this E_6 peak is debated as being associated with divacancy-hydrogen (V_2H) complex [71, 73, 74]. Appearance of the latter E_6 peak in diodes with the triangle defect distribution profile can be explained by a decay scenario of a dense area of VOH complexes within the base region, when creation of V_2H complexes is preferable relatively to pure divacancies due to weaker escape of hydrogen. At highest anneal temperatures a peak at 120 K prevails, which might be ascribed to C_iC_s complexes.

7.4.2. Anneal dependent variations of operational characteristics

For *pin* diodes, both with a δ-shape layer (2 MeV protons) and containing a triangle profile (gradually varied energy 2.7–2.0 MeV of protons) created with average fluence of 7×10^{13} p/cm^2, the reverse recovery time τ_{RR} increases after each step of 24 h heat treatment, as illustrated in Fig. 7.17 (a). After final (in this investigation) 400 ^{o}C annealing step, the value of τ_{RR} at elevated injection levels (~I_F) in diodes containing a δ-shape layer is almost completely restored to that measured in the non-irradiated diode, Fig. 7.17 (a). In diodes containing a triangle profile of defect distribution along the base (Fig. 7.17 (b)), irradiated by the smallest fluence, τ_{RR} is also restored to that measured in the non-irradiated diode. However, for diodes irradiated by larger fluences, the restoration of τ_{RR} values is incomplete, and restoration level depends on irradiation fluence. In addition, τ_{RR} in heat treated diodes becomes to be dependent on injection level, as shown in τ_{RR}–I_F plots for as-irradiated and heat treated diodes, Fig. 7.17 (b). The observed variations of τ_{RR}–I_F characteristic can be explained by different impact of point-like complexes and of extended clusters. The revealed decay of the point-like VOH complexes (in DLTS spectra) determines the high injection level carrier recombination lifetime τ_{HL}, due to the change of type of the dominant deep centres. The re-arrangement of a space-charge sphere (surrounding cluster) during heat treatments causes a redistribution of carriers and a limited filling of deep centres. The forward voltage drop U_F decreases after each temperature step of employed heat treatments, as illustrated in Fig. 7.17 (c). However, values of U_F in the annealed diodes do not reach that value in the non-irradiated ones. Although, the observed U_F reduction shows a beneficial impact of annealing in the correction of static parameters of the irradiated *pin* diodes. The revealed behaviour can be explained by radiation and heat treatment-induced variations of resistivity of the base region material. Annealing determines a reduction of this resistivity, and, subsequently of U_F values.

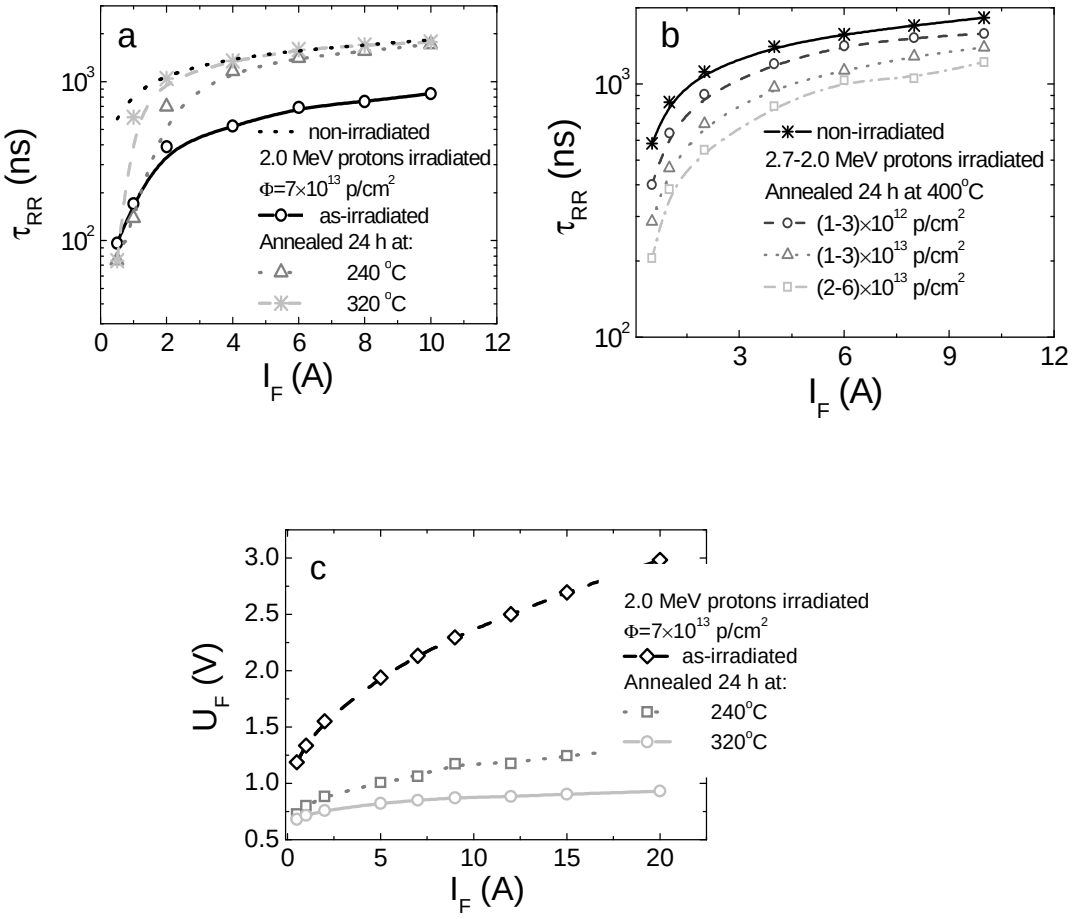

Fig. 7.17. Reverse recovery time (a, b) and forward voltage drop (c) as a function of forward current. These characteristics are compared for *pin* diodes containing either the δ-shape (a,c) or triangle profile (b) of irradiation defects distribution. Variations of these characteristics obtained by varying heat treatment temperature are shown relatively to those measured in non-irradiated and as-irradiated the same *pin* diodes.

Evolution of I–V characteristics for diodes irradiated by 2.0 MeV protons of fluence 7×10^{13} p/cm^2 after several temperature steps within isochronous 24 h heat treatment is illustrated in Fig. 7.18. The leakage current is reduced in all the applied reverse voltage range relatively to the current values obtained in the as-irradiated diode. The steep current increase due to percolation and to avalanche current effects disappears in the whole range of applied bias voltages. However, an enhancement of the heat treatment temperature above 160 °C leads to an increase of leakage current at elevated reverse voltages. This implies a shift of the steep current increase segment towards the range of higher voltages, exceeding those employed in this

investigation. The course of leakage current variation with U_R in the diode heated at 320 ^{o}C remains similar to that obtained after annealing at 240 ^{o}C. Therefore, a beneficial annealing of radiation defects can be implemented in the temperature range of 20–200 ^{o}C.

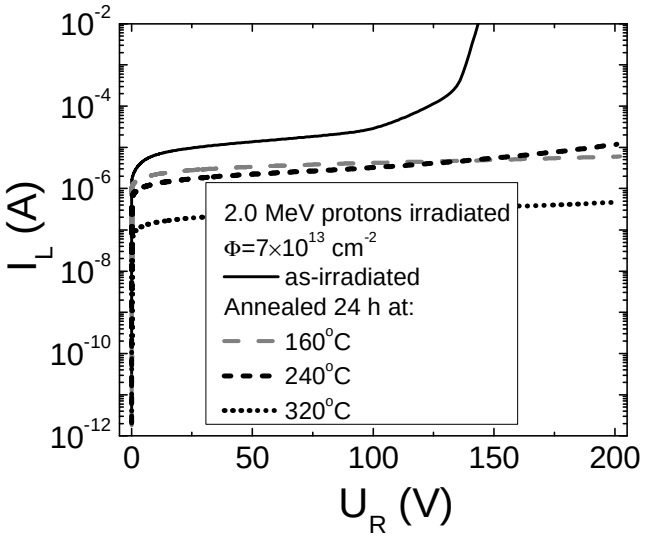

Fig. 7.18. Variations of the I-V characteristics in 2.0 MeV protons irradiated diodes after various temperature steps of the isochronal 24 h heat treatment.

Summary of the main results described in the chapter

[A2-A9, A20]

It has been obtained that recombination lifetime decreases almost linearly from tenths of nanoseconds to 1 ns by varying the protons fluence in the range of 7×10^{12}-4×10^{14} p/cm^2 and lifetime values are obtained to be shorter relatively to values obtained in Si samples irradiated by penetrative protons. After isochronal 24 h anneal a higher increase of recombination lifetime with anneal temperature is observed in samples irradiated with higher fluences while in the lowest fluence irradiated samples carrier lifetime is almost invariable.

The VOH complexes are dominant within the stopping range of protons in the as-irradiated diodes. Isochronous 24 h heat treatments of the irradiated diodes indicate an efficient annealing of the VOH complexes by transforms to other divacancy associated deep centres via vacancy clusters V_n. An additional hydrogen related complex associated with divacancy-hydrogen (V_2H) complex

is observed in diodes containing triangle defects distribution profile. These anneal induced transforms of defects are explained by a decay scenario of dense area of VOH complexes within the base region, when creation of V_2H complexes is preferable relatively to generation of pure divacancies due to weaker escape of hydrogen. At the highest anneal temperatures >320 ^oC divacancy associated defects anneal out, and the carbon C_iC_s complexes become prevailing.

Reverse recovery time τ_{RR} decreases with irradiation fluence and strongly depends on the layer profile and on location of this layer containing deep recombination centres. The fastest switching rate is achieved in diodes containing the triangle defects distribution profile. The forward voltage drop U_F increases with irradiation fluence and U_F*'s* value is the largest for a diode containing the δ-shape defects profile located at the half-width of the base region, due to increased integral resistivity within damaged region. An increase of τ_{RR} and a decrease of U_F values were observed in diodes after heat treatments.

Concerted analysis of changes of the I–V characteristics in *pin* diodes with radiation damaged layers of various profiles unveiled a different impact of point and of cluster type radiation defects on transforms of diode electrical characteristics. Point-like radiation induced and vacancy-ascribed complexes are responsible for the increase of leakage current in the range of small reverse voltages. Extended clusters, owing to a space-charge sphere surrounding a cluster with inherent charging of cluster core, modify the I–V characteristics when radiation damaged layers are located nearby the metallurgic junction. A steep leakage current increase in I–V characteristic appears to be caused by forward biased space-charge regions around clusters or generation of micro-plasma in local strong fields. The local field effects, caused by the extended radiation defects, depend on cluster density gradients, and these effects are more pronounced in diodes containing a narrow δ-shape radiation damaged layer within the diode base. Annealing of point defects within a material that surrounds the cluster space charge spheres is mostly probable and observable

after heat treatments in the temperature range of 20–320 ^{o}C, when the density of clusters is rather small.

Therefore, improvement of dynamic (τ_{RR}) and of static (U_F, I_L) parameters of the *pin* switchers can be reached only as a trade-off among irradiation and heat treatment technological procedures.

In summary, the combined modelling and measurements of the reverse recovery time, of recovery softness and of forward voltage drop characteristics in Si power diodes show that these parameters strongly depend on values of carrier lifetime at high injection and on their depth-distribution within diode base region, while the desired trends in variations of these parameters dependent on carrier lifetime appear at discrepant tendencies. Therefore optimization of dynamic diode operation characteristics can be only achieved by trade-off, using formation of strongly localized and predictably distributed recombination centres by proton beams when stabilized extended radiation defects are created. To reach a trade-off between the dynamic and static diode parameters, the radiation induced traps with short low-level carrier lifetime (τ_{LL}) should be annealed, however creation of different species and densities of protons beam induced defects makes a program for annealing procedures to be complicated.

Summary of dissertation results and conclusions

Measurement technology results

1. Surface passivation by iodine ethanol solution increases recombination lifetime from 1.2 µs to 58 µs for the investigated float zone (FZ) n-Si samples.
2. Barrier evaluation by linearly increasing voltage (BELIV) pulsed technique approved to be a useful extension of transient techniques for the separation of barrier charging and carrier capture/emission current components and for the fast estimation of the impact of traps.
3. The models for under-depleted diode with induced charge and of current transients at low and high densities of the photo-excited excess carrier domain within diode base region have been proposed. In material with small density of traps the displacement Ramo's current prevails. In heavily irradiated diodes carrier capture and emission components become dominant.
4. The BELIV technique has been approved for the spectroscopy of deep levels and for profiling of dopants concentration and depth of junctions within layered structures. The instrument for spectroscopy and profiling has been designed and approved.

Spectroscopy results

5. Spectra measured by the BELIV-IR pulsed technique have been compared with those registered by C-DLTS on the same Si thyristor structures in the case that the dopant density is close to that of the trap concentration showing good agreement between both techniques. The activation energy of the trap within bandgap was evaluated to be 0.3 eV and ascribed to sulphur impurity.
6. The photo-ionization peaks with activation energy values of E_1=0.3±0.02 eV, E_2=0.41±0.01 eV and E_3=0.51±0.01 eV (ascribed to divacancies of different charge state $V^{=/-}$, $V^{-/0}$ and defect clusters, respectively) in an n-Si

layer with a dopant density of $N_D \approx 10^{12}$ cm^{-3} irradiated with $\Phi = 10^{13}$ n/cm^2 were obtained by BELIV-IR pulsed measurements.

7. The distribution of dopants density as well as the depth of junctions have been evaluated by employing the BELIV technique for a cross-sectional scan of the boundary of the structure with a needle-tip probe within *pnp*, *pnpn*$^+$ and pin structures. Also the distribution of S, C, Cu within *pnp* and *pnpn*$^+$ structures and of V_2 traps within *pin* structure has been determined by employing the C-V and C-DLTS techniques.

Results of investigation of radiation induced defects

8. Combined analysis of C-V, I-V and barrier capacitance charging currents revealed that barrier capacitance decreases with neutron irradiation fluence and reaches its geometrical value C_{geom}=9 pF at the highest fluences ($\Phi \geq 10^{16}$ cm^{-2}) in 300 μm thick n-type Si diodes doped with 10^{12} cm^{-3} donors due to radiation induced carrier traps that reduce free carriers concentration.
9. Values of the effective recombination lifetime measured in situ during 8 MeV protons irradiation by the MW-PCT-E technique on diodes with applied electric field start to saturate. This saturation is explained by manifestation of multi-trapping effect, when several centres of different species act together. Saturation of the effective recombination lifetime correlates well with enhancement of leakage current relatively to the irradiation exposure time scale.
10. A small impact of irradiation on the carrier scattering parameters was unveiled during 8 MeV protons irradiation when carrier capture processes prevail. Electrons mobility was evaluated to be μ_e=1300 cm^2/Vs.
11. *In situ* experiments of barrier capacitance charging current measurements during protons implantation revealed that carrier recombination processes determine the increase of dielectric relaxation time within electrically neutral region (ENR) of a diode base. This leads to the elongated time scale of stabilization of depletion width. Carrier capture/emission

processes within space charge (SC) and transition layer (between ENR and SC) regions lead to the increase of generation/recombination currents in the irradiated diode.

Results of optimization of device parameters by radiation techniques

12. The combined modelling and measurements of the reverse recovery time, of the recovery softness and of the forward voltage drop characteristics in Si power diodes show that these parameters strongly depend on values of carrier lifetime at high injection level and on their depth-distribution within diode base region, while the desired trends in variations of these parameters dependent on carrier lifetime appear at discrepant tendencies. Reverse recovery time decreases with reduction of the high injection level carrier lifetime τ_{HL}. Reduction of τ_{HL} causes an increase of the forward voltage drop.
13. The VOH complexes are dominant within the stopping range of protons in the as-irradiated diodes. Isochronous 24 h heat treatments of the irradiated diodes indicate an efficient annealing of the VOH complexes by transforms to other divacancy associated deep centres mediated by the vacancy cluster V_n transforms. An additional hydrogen related complex associated with divacancy-hydrogen (V_2H) complex is observed in diodes containing a triangle defects distribution profile. These anneal induced transforms of defects are explained by a decay scenario of dense area of VOH complexes within the base region, when creation of V_2H complexes is preferable relatively to generation of pure divacancies due to a weaker escape of hydrogen. At the highest anneal temperatures >320 ^{o}C, the divacancy associated defects anneal out, and the carbon C_iC_s complexes become prevailing.
14. Optimization of dynamic diode operation characteristics can be only achieved by trade-off, using formation of strongly localized and predictably distributed recombination centres by proton beams when stabilized extended radiation defects are created. To reach a trade-off

between the dynamic and static diode parameters, the radiation induced traps with short low-level carrier lifetime (τ_{LL}) should be annealed.

References

[1] C. Claeys, and E. Simoen, *Radiation effects in advanced semiconductor materials and devices* (Springer-Verlag Berlin Heidelberg, 2002).

[2] J.R. Srour, Review of Displacement Damage Effects in Silicon Devices. IEEE Transactions on Nucl. Sc., **50** (2003) 553-670.

[3] F.B. McLean, and T.R. OldHam, Basic mechanisms of radiation effects in electronic materials and devices. US Army Lab command, HDL-TR-2129, US Army command, Harry Diamond Laboratories, MD, USA (1987).

[4] V. Privitera, S. Coffa, F. Priolo, and E. Rimini, Migration and interaction of point defects at room temperature in crystalline silicon. Rivista del Nuovo Cimento **21** (1998) 1-52.

[5] M. Huhtinen, Simulation of non-ionising energy loss and defect formation in silicon. Nucl. Instrum. Methods A **491** (2002) 194–215.

[6] M. Moll, E. Fretwurst, and G. Lindstrom, Investigation on the improved radiation hardness of silicon detectors with high oxygen concentration. Nucl. Instrum. Methods A **439** (2000) 282-292.

[7] J.B. Baliga, *Power Semiconductor devices* (PWS Publishing company, Boston, 1996).

[8] B.C. MacEvoy, and G. Hall, Defect kinetics in novel detector materials. Material Sc. Semiconductor Processing **3** (2000) 243-249.

[9] W. Shockley, and W.T. Read, Statistics of the recombination of holes and electrons. Phys. Rev. **85** (1952) 835-842.

[10] J.S. Blakemore, *Semiconductor statistics* (Pergamon Press, 1962).

[11] P. Hazdra, K. Brand, and J. Vobecky, Defect distribution in MeV proton irradiated silicon measured by high-voltage current transient spectroscopy. Nucl. Instrum. Methods B **192** (2002) 291–300.

[12] P. Hazdra, J. Rubeš, an J. Vobecky, Divacancy profiles in MeV helium irradiated silicon from reverse I-V measurement. Nucl. Instrum. Methods B **159** (1999) 207-217.

[13] P. Hazdra, and J. Vobecky, Nondestructive defect characterization and engineering in contemporary silicon power devices. Solid State Phenom. **69–70** (1999) 545–550.

[14] P. Hazdra, J. Vobecky, H. Dorschner, and K. Brand, Axial lifetime control in silicon power diodes by irradiation with protons, alphas, low- and high-energy electrons. Microelectron. J. **35** (2004) 249–257.

[15] P. Hazdra, and H. Dorschner, Radiation defect distribution in silicon irradiated with 600 keV electrons, Nucl. Instrum. Methods B **201** (2003) 513–519.

[16] A. Hallen, N. Keskitalo, F. Masszi, and V. Nagl, Lifetime in proton irradiated silicon. J. Appl. Phys. **79** (1996) 3906–3914.

[17] P. Leveque, P. Pellegrino, A. Hallen, B.G. Svensson, and V. Privitera, Hydrogen-related defect centers in float-zone and epitaxial n-type proton implanted silicon. Nucl. Instrum. Methods B **174** (2001) 297–303.

[18] M. Mikelsen, E.V. Monakhov, G. Alfieri, B.S. Avset, J. Harkonen, and B.G. Svensson, Annealing of defects in irradiated silicon detector materials with high oxygen content. J. Phys. Condens. Matter **17** (2005) 2247–2253.

[19] Hazdra, and V. Komarnitskyy, Lifetime control in silicon power P-i-N diode by ion irradiation: Suppression of undesired leakage. Microelectron. J. **37** (2006) 197–203.

[20] S. Godey, E. Ntsoenzok, D.C. Schmidt, and J.F. Barbot, Effect of shallow donors induced by hydrogen on P^+N junctions. Mater. Sci. Eng. B 58 (1999) 108.

[21] P. Hazdra, J. Vobecky, and K. Brand, Optimum lifetime structuring in silicon power diodes by means of various irradiation techniques. Nucl. Instrum. Methods B **186** (2002) 414–418.

[22] P. Hazdra, and V. Komarnitskyy, Thermal donor formation in silicon enhanced by high-energy helium irradiation. Nucl. Instrum. Methods B **253** (2006) 187–191.

[23] P. Hazdra, and V. Komarnitskyy, Influence of radiation defects on formation of thermal donors in silicon irradiated with high-energy helium ions. Materials Sc. Eng. B **159–160** (2009) 346–349.

[24] P. Hazdra, K. Brand, J. Rubeš, and J. Vobecky, Local lifetime control by light ion irradiation: impact on blocking capability of power P-i-N diode. Microelectron. J. **32** (2001) 449–456.

[25] P. Hazdra, and J. Vobecky, Platinum in-diffusion controlled by radiation defects for advanced lifetime control in high power silicon devices. Mat. Sc. Eng. B **124–125** (2005) 275–279.

[26] J. Vobecky, and P. Hazdra, The application of platinum–silicide anode layer to decrease the static and turn-off losses in high-power P-i-N diode. Thin Solid Films **433** (2003) 305–308.

[27] J. Vobecky, and P. Hazdra, Dynamic avalanche in diodes with local lifetime control by means of palladium. Microelectron. J. **39** (2008) 878–883.

[28] J. Vobecky, and P. Hazdra, Low-temperature radiation controlled diffusion of palladium and platinum in silicon for advanced lifetime control. Nucl. Instrum. Methods B **253** (2006) 162–166.

[29] P. Hazdra, V. Komarnitskyy, and V. Bursikova, Hydrogenation of platinum introduced in silicon by radiation enhanced diffusion. Mat. Sc. Eng. B **159–160** (2009) 342–345.

[30] S. Ramo, Currents Induced by Electron Motion. Proceedings of I.R.E. (1939) 584-585.

[31] I.V. Kotov, Currents induced by charges moving in semiconductor. Nucl. Instrum. Methods A **539** (2005) 267-268.

[32] L-A. Hamel, and M. Julien, Generalized demonstration of Ramos's theorem with space charge and polarization effects. Methods Phys. Res. A **597** (2008) 207-211.

[33] G.Cavalleri, E. Gatti, G. Fabri, and V. Svelto, Extension of Ramo's theorem as applied to induced charge in semiconductor detectors. Nucl. Instrum. Meth. **92** (1971) 137-140.

[34] P. De Visschere, The validity of Ramo's theorem. Solid St. Electron. **33** (1990) 455-459.

[35] G. Lutz, *Semiconductor radiation detectors* (Springer, Heidelberg-Berlin-New York, 2007).

[36] H. Spieler, *Semiconductor detector systems* (Oxford University Press, New York, 2005).

[37] G. Lindstrom, M. Moll, and E. Fretwurst, Radiation hardness of silicon detectors - a challenge from high-energy physics. Nucl. Instrum. Methods A **426** (1999) 1-15.

[38] D. Campbell, A. Chilingarov, and T. Sloan, Frequency and temperature dependence of the depletion voltage from CV measurements for irradiated Si detectors. Nucl. Instrum. Methods A **492** (2002) 402–410.

[39] V. Eremin, N. Strokan, E. Verbitskaya, and Z. Li, Development of transient current and charge techniques for the measurement of effective net concentration of ionized charges (N_{eff}) in the space charge region of p-n junction detectors. Nucl. Instrum. Methods A **372** (1996) 388-398.

[40] J. Harkonen, V. Eremin, E. Verbitskaya, S. Czellar, P. Pusa, Z. Li, and T.O. Niinikoski, The Cryogenic Transient Current Technique (C-TCT) measurement setup of CERN RD39 Collaboration, Nucl. Instrum. Methods A **581** (2007) 347-350.

[41] V. Eremin, and Z. Li, Carrier drift mobility study in neutron irradiated high purity silicon, Nucl. Instrum. Methods A **362** (1995) 338-343.

[42] C. Leroy, P. Roy, G. Casse, M. Glaser, E. Grigoriev, and F. Lemeilleur, Study of charge transport in non-irradiated and irradiated silicon detectors, Nucl. Instrum. Methods A **426** (1999) 99-108.

[43] T.J. Brodbeck, A. Chilingarov, T. Sloan, E. Fretwurst, M. Kuhnke, and G. Lindstroem, Carrier mobilities in irradiated silicon, Nucl. Instrum. Methods A **477** (2002) 287-282.

[44] P. Blood, J.W. Orton, *The Electrical Characterization of Semiconductors: Majority Carriers and Electron States* (Academic Press Inc., San Diego, 1992).

[45] D.K. Schroder, *Semiconductor Material and Device Characterization* (John Wiley & Sons, New Jersey, 2006).

[46] I. Pintilie, C. Tivarus, L. Pintilie, M. Moll, E. Fretwurst, and G. Lindstroem, Thermally stimulated current method applied to highly irradiated silicon diodes. Nucl. Instrum. Methods A **476** (2002) 652-657.

[47] I. Pintilie, G. Lindstroem, A. Junkes, and E. Fretwurst, Radiation-induced point-and cluster-related defects with strong impact on damage properties of silicon detectors. Nucl. Instrum. Methods A **611** (2009) 52–68.

[48] Z. Li, W. Chen, V. Eremin, R. Gul, Y.H. Guo, J. Harkonen, P. Luukka, E. Tuovinen, and E. Verbitskaya, Equal-double junctions in 24GeV/c proton-irradiated MCZ n-and p-type Si detectors: A systematic transient current technique investigation. Nucl. Instrum. Methods A **612** (2010) 539–548.

[49] E. Verbitskaya, V. Eremin, I. Ilyashenko, Z. Li, J. Harkonen, E. Tuovinen, and P. Luukka, Operation of heavily irradiated silicon detectors in non-depletion mode. Nucl. Instrum. Methods A **557** (2006) 528–536.

[50] V. Eremin, E. Verbitskaya, and Z. Li, The origin of double peak electric field distribution in heavily irradiated silicon detectors, Nucl. Instrum. Methods A **476** (2002) 556–564.

[51] V. Eremin, E Verbitskaya, and Z. Li, Effect of radiation induced deep level traps on Si detector performance. Nucl. Instrum. Methods A **476** (2002) 537–549.

[52] E. Verbitskaya, V. Eremin, Z. Li, J. Harkonen, and M. Bruzzi, Concept of double peak electric field distribution in the development of radiation hard silicon detectors. Nucl. Instrum. Methods A **583** (2007) 77–86.

[53] D. Campbell, A. Chilingarov, and T. Sloan, Evaluation of possible equivalent circuits for the description of the CV characteristics of heavily irradiated Si diodes. Nucl. Instrum. Methods A **552** (2005) 152–157.

[54] E. Gaubas, Transient absorption techniques for investigation of recombination properties in semiconductor materials. Lith. J. Phys. **43** (2003) 145-165.

[55] S.M. Sze, *Physics of Semiconductor Devices* (John Wiley & Sons, Inc., Hoboken, New Jersey 2007).

[56] L.T. Pillage, R.A. Rohrer, and C. Visweswariah, *Electronic circuit and system simulation methods* (McGraw-Hill, NY, 1995).

[57] P.M. Morse and H. Feshbach, *Methods of theoretical physics, Part I,* (McGraw-Hill Book Company, New York, 1953).

[58] D.G. Duffy, *Green's functions with applications* (Chapman&Hall/CRC, New York, 2001).

[59] R. Smith, *Semiconductors, 2nd ed.* (Cambridge Univ. Press, London – New York, 1982).

[60] S. Vayrynen, P. Tikkanen, J. Raisanen, I. Kassamakov, and E. Tuominen, Effects of activation by proton irradiation on silicon particle detector electric characteristics. J. Appl. Phys. **106** (2009) 024908.

[61] H. Amekura, N. Kishimoto, and K. Kono, Particle-induced conductivity and photoconductivity of silicon under 17 MeV proton irradiation. Journ. Appl. Phys. **84** (1998) 4834.

[62] N. Shashank, V. Singh, S.K. Gupta, K.V. Madhu, J. Akhtar, and R. Damle, DLTS and in situ C–V analysis of trap parameters in swift 50 MeV Li^{3+} ion-irradiated Ni/SiO_2/Si MOS capacitors. Rad. Effects and Defects in Solids **166** (2011) 313.

[63] Z. Li and C.J. Li, Development of current-based microscopic defect analysis method using optical filling techniques for the defect study on heavily irradiated high-resistivity Si sensors/detectors. Mater. Sci. Semicond. Processing **9** (2006) 283.

[64] S.T. Pantelides, The electronic structure of impurities and other point defects in semiconductors. Rev. Mod. Phys. **50** (1978) 797.

[65] G. Lucovsky, On the photoionization of deep impurity centers in semiconductors. Solid State Commun. **3** (1965) 299.

[66] H.G. Grimmeiss, Deep level impurities in semiconductors. Annu. Rev. Mat. Sci. **7** (1977) 341.

[67] J.W. Chen and A.G. Milnes, Energy levels in silicon. Annu. Rev. Mat. Sci. **10** (1980) 157.

[68] M. Karimov and A. Karakhodzhaev, Influence of the post-diffusion hardening rate and thermal treatment on the thermal stability of the charge-carrier lifetime in overcompensated n-Si(B,S). Russ. Phys. J. **44** (2001) 734.

[69] http://www.srim.org/

[70] E. Gaubas, A. Kadys, A. Uleckas, and J. Vaitkus, Investigation of carrier recombination in Si heavily irradiated by neutrons. Acta Phys. Pol. A **113** (2008) 837-840.

[71] P. Johannesen, B. Bech Nielsen, and J.R. Byberg, Identification of the oxygen-vacancy defect containing a single hydrogen atom in crystalline silicon. Phys. Rev. B **61** (2000) 4659–4666.

[72] K. Gill, G. Hall, and B. MacEvoy, Bulk damage effects in irradiated silicon detectors due to clustered divacancies. J. Appl. Phys. **82** (1997) 126–136.

[73] P. Johannesen, R. Jakobsen, P. Stallinga, B. Bech Nielsen, and J.R. Byberg, Silicon vacancy containing two hydrogen atoms studied with electron paramagnetic resonance and infrared absorption spectroscopy. Phys. Rev. B **66** (2002) 235201.

[74] P. Leveque, A. Hallen, P. Pellegrino, B.G. Svensson, and V. Privitera, Dose-rate influence on the defect production in MeV proton-implanted float-zone and epitaxial n-type silicon. Nucl. Instrum. Methods B **186** (2002) 375–379.